Doctoral theses at NTNU, 2024:241

Florian Beiser

Local Drift Forecasting with Simplified Ocean Models and Multi-Level Data Assimilation

Doctoral thesis

NTNU
Norwegian University of Science and Technology
Thesis for the Degree of
Philosophiae Doctor
Faculty of Information Technology and Electrical
Engineering
Department of Mathematical Sciences

NTNU
Norwegian University of
Science and Technology

Florian Beiser

Local Drift Forecasting with Simplified Ocean Models and Multi-Level Data Assimilation

Thesis for the Degree of Philosophiae Doctor

Trondheim, June 2024

Norwegian University of Science and Technology
Faculty of Information Technology and Electrical Engineering
Department of Mathematical Sciences

NTNU
Norwegian University of
Science and Technology

NTNU
Norwegian University of Science and Technology

Thesis for the Degree of Philosophiae Doctor

Faculty of Information Technology and Electrical Engineering
Department of Mathematical Sciences

ISBN 978-82-326-8074-0 (printed ver.)
ISBN 978-82-326-8073-3 (electronic ver.)
ISSN 1503-8181 (printed ver.)
ISSN 2703-8084 (online ver.)

Doctoral theses at NTNU, 2024:241

Printed by NTNU Grafisk senter

Abstract

Search-and-rescue operations at sea are supported by fast predictions of drift trajectories that are classically based on operational ocean models. This thesis promotes a complementary approach for drift forecasting based on computationally efficient methodologies utilising simplified models and ensemble-based data assimilation.

Simplified ocean models aim to capture only the most relevant dynamics for short time horizons and they are hence more computationally efficient than complex operational models. Herein, the rotational shallow-water equations and a massively parallel simulation framework are exploited for the simplified modelling. Given the inherent inaccessibility of the true dynamics of the ocean, both presently and in the future, large ensembles of simplified models can be run to account for this spatio-temporal uncertainty in local forecasts. Such ensemble-based representations enable the incorporation of observations of ocean currents by data assimilation techniques as new measurements are available. Consequently, the uncertainty in the prediction is typically reduced. In this work, methodologies behind such an on-demand system for local short-term drift trajectory prediction are considered. The investigations include different modelling and assimilation techniques suitable for search-and-rescue scenarios.

The first part of this thesis synthesises the background and the description of the general concepts, whereas the second part consists of the scientific papers. The contributions in this thesis reach from the discussion of numerical solvers for shallow-water simulations, over mathematical modelling for simplified ocean dynamics, to tailored data assimilation methods for sparse in-situ observations and settle with the advancement of computational efficient data assimilation, building on the foundations of multilevel Monte Carlo methods and simulations on different resolutions.

Contents

Preface i

Acknowledgments i

Papers included in thesis iii

Part I: Background

1 Introduction 1

2 Simplified Ocean Models 7
- 2.1 Shallow-Water Equations 8
- 2.2 Barotropic and Baroclinic Modelling 15
- 2.3 Trajectory Modelling 17

3 Ensemble Forecasts 19
- 3.1 Sources of Uncertainty 19
- 3.2 Uncertainty Quantification 21

4 Data Assimilation 27
- 4.1 The Data Assimilation Problem 28
- 4.2 Ensemble-Based Data Assimilation 29
- 4.3 Assessment of Ensemble Forecasts 35

5 Multi-Level Data Assimilation 39
- 5.1 Multi-Level Monte Carlo Estimators 41
- 5.2 Practicalities for Multi-Level Ensembles 44
- 5.3 Multi-Level Ensemble Kalman Filter 48
- 5.4 Assessment of Multi-Level Ensemble Forecasts 50

6 Paper Contributions **53**
Paper I 55
Paper II 57
Paper III 59
Paper IV 61

7 Concluding Remarks and Outlook **65**
7.1 Concluding Remarks 66
7.2 Outlook 68

Bibliography **73**

Part II: Scientific Papers

Paper I **87**
Reducing Numerical Artifacts by Sacrificing Well-Balance for Rotating Shallow-Water Flow

Paper II **97**
Combining Barotropic and Baroclinic Simplified Models for Drift Trajectory Predictions

Paper III **125**
Comparison of Ensemble-Based Data Assimilation Methods for Sparse Oceanographic Data

Paper IV **161**
Multi-Level Data Assimilation for Simplified Ocean Models

Preface

This thesis is submitted in partial fulfillment of the requirements for the degree of philosophiae doctor (PhD) at the Norwegian University of Science and Technology (NTNU), Trondheim, Norway.

The work has been performed at the Department of Mathematics and Cybernetics, SINTEF Digital, Oslo, and the Department of Mathematical Sciences, NTNU, Trondheim. It was financed by the Norwegian Research Council through the Havvarsel project, grant number 310515.

Acknowledgments

Først og fremst vil jeg framheve Håvards veiledning som førte til denne avhandlingen. Jeg er veldig takknemlig for at han sprer så mye motivasjon, lagånd og gode råd. Jeg setter stor pris på det tette samarbeidet preget av spontane diskusjoner med lav terskel og de mange tipsene relatert til vitenskapelig arbeid, programmering og for å holde blikk på de store målene i prosjektet. Dessuten takker jeg Jo for å ha ønsket meg velkommen på NTNU i Trondheim i det første semesteret og for å ha holdt kontakten gjennom hele doktorgradstudiet. Det var nyttig med innspill fra den statistiske siden fra Jo og vurderingen fra den operative siden fra Martin i MET. I tillegg var det artig å jobbe sammen med Kjetil og å diskutere med ham matematikken som ligger bak. Ved siden av det faglige har Knut-Andreas bistod med å skape de riktige rammebetingelsene, slik at jeg har kunnet lære mange ting i løpet av de siste tre og et halvt årene.

For øvrig har kollegene i Applied Computational Science-gruppen i SINTEF Digital støttet alltid med et trivelig og svært profesjonelt miljø, og ikke minst med mange ideer for nye eventyr i den norske naturen. Likeså var det gøy å tilbringe tid med gode kollegaer på IMF hos NTNU. Takk til alle sammen!

Florian Beiser
Oslo, February 2024

List of Papers

Papers included in thesis

I: **Reducing Numerical Artifacts by Sacrificing Well-Balance for Rotating Shallow-Water Flow**
Håvard Heitlo Holm, Florian Beiser
Finite Volumes for Complex Applications X—Volume 2, Hyperbolic and Related Problems

DOI: 10.1007/978-3-031-40860-1_19

II: **Combining Barotropic and Baroclinic Simplified Models for Drift Trajectory Predictions**
Florian Beiser, Håvard Heitlo Holm, Martin Lilleeng Sætra, Nils Melsom Kristensen, Kai Håkon Christensen
In review

III: **Comparison of Ensemble-Based Data Assimilation Methods for Sparse Oceanographic Data**
Florian Beiser, Håvard Heitlo Holm, Jo Eidsvik
Quarterly Journal of the Royal Meteorological Society

DOI: 10.1002/qj.4637

IV: **Multi-Level Data Assimilation for Simplified Ocean Models**
Florian Beiser, Håvard Heitlo Holm, Kjetil Olsen Lye, Jo Eidsvik
In review

Part I

Background

Chapter 1

Introduction

Daily weather forecasts are a familiar service and they extensively influence people's everyday lives on multiple aspects. For everyone at sea or in coastal areas, ocean forecasts are equally important as atmospheric weather forecasts. While numerical weather prediction and ocean forecasting share structural similarities, the preconditions for ocean forecasts are more challenging: the dynamics are more complex due to feature systems of smaller scales and the amount of observation data is significantly less.

Data plays a crucial role to improve the description of the current conditions of the ocean, but observations alone are insufficient to recover the complete ocean state and fall short to predict future ones. Therefore, observations are combined with numerical simulations. Mathematical models resemble the dominating physical processes in the ocean and generate forecasts for future dynamics, while available measurements are sequentially assimilated into model forecasts. After an update reflecting the latest observations, new forecasts can be produced. As more data is assimilated closer to the target time, the precision of statistical predictions is thereby improved.

At sea, search-and-rescue (SAR) operations rely on fast and trustworthy forecasts of drift trajectory to define search areas [27, 99]. Such drift predictions are commonly produced by trajectory models using the operational forecasts. In that, operational ocean forecast architectures are built on complex models that aim for as precise as possible simulations and assimilation of all available data. Therefore, operational forecasts require large computational resources and deliver predictions on a fixed resolution.

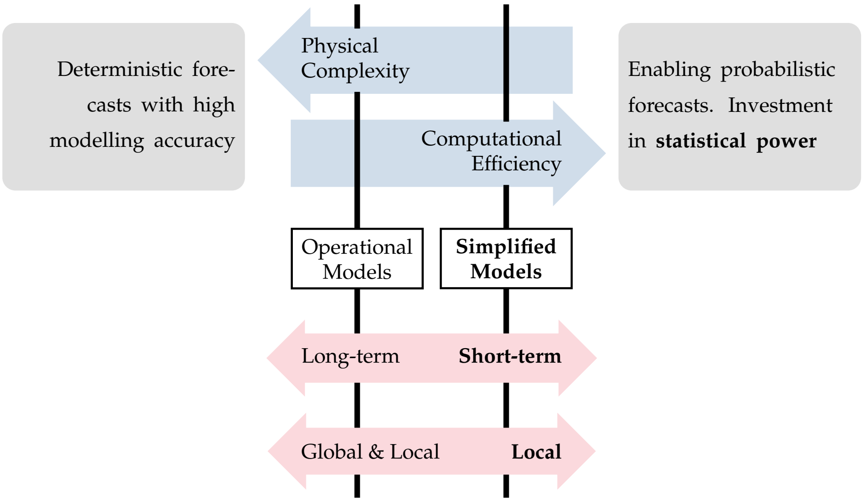

Figure 1.1: Simplified models treat some of the physical complexity in favour for computational efficiency which is useful for conducting uncertainty quantification.

In Norway, 80% of the population lives within 10 km of the coast. Additionally, the Norwegian coast line is the second longest in the world with narrow fjords and archipelagos. For these reasons, high-resolution forecasts that capture local features in the ocean currents and that can be used for rapid drift predictions are required.

In this thesis, we follow a complementary approach for local drift trajectory forecasting that utilises ensembles of simplified models together with multi-level data assimilation. Thereby, we facilitate lightweight decision-support tools that exploit fast and flexible models and assimilate sparse in-situ observations.

In general, ocean circulation models are capable of representing a wide range of oceanographic processes and provide high-fidelity predictions. These cutting-edge ocean models afford an accurate description of the three-dimensional physics, and assimilation of data from different sources for precise estimates of the true ocean state. However, they often produce only a single simulation due to extensive computational demands and restricted resources. Drift forecasts can then be generated by an offline trajectory model using results of operational simulations.

In contrast, simplified ocean models offer a lightweight supplement with reduced computational burden, enabling rapid and replicated simulations. Simplified models capture the dominant physical processes and

Figure 1.2: Photos of experimental drifters used for drift trajectory monitoring during a cruise in Inner Oslofjord on the 27.04.2023. Drifters can be used to gather current observations in a specific area of interest.

can flexibly increase resolutions, making them suitable for local short-term forecasting. They provide a valuable approximation of the real ocean state over short time spans, allowing for efficient and timely predictions in applications like drift trajectory forecasting for SAR or emergency response decision-support. This is a different use case than climate modelling where the goals are involving long time horizons and global coverage [5]. Furthermore, by running numerous simulations, an ensemble of simplified models can feature enhanced statistical properties, efficiently explore the uncertainty space, and yield improved probabilistic forecasts, a capability not easily achievable with deterministic circulation models. Figure 1.1 exhibits these contrasts.

Observational data obtained from, e.g. drifters (see Figure 1.2), can be used to improve the accuracy of ensemble forecasts by data assimilation techniques. Hereby, relevant in-situ observations are sparse, since related measurements are collected only at few locations in the ocean. Data assimilation helps to calibrate models and to correct biases, and it adjusts the model state to better match observations, yielding more reliable forecasts which often have reduced uncertainty. With deterministic models on one end of the scale, machine learning models represent another extreme approach where all physical behaviour is supposed to be learned from data [65]. While the machine learning approach often suffers from insufficient training data in the case of SAR missions, data assimilation is a data-driven approach that combines the physical model and observational data in a statistically principled framework.

The computational benefits of simplified ocean models facilitate producing ensemble forecasts in local domains with high spatial resolution and assimilating latest in-situ observations that have not been respected in the operational machinery. Consequently, we promote the application of the simplified approach in time-sensitive SAR scenarios.

In this work, we advance the complementary approach that combines simplified ocean models and data assimilation for the prediction of drift trajectories in local areas. Therefore, we present contributions to the following research objectives:

I Adaption of the numerical simulations for simplified ocean models to produce more realistic results.

II Extension of the modelling framework for simplified ocean models to capture a variety of simplified dynamics.

III Dwelling on the data assimilation aspect with techniques that are tailored for sparse observations.

IV Design of multi-level data assimilation for simplified ocean models where simulations on multiple resolutions are exploited.

The *havvarsel* Project The *havvarsel* project is a collaboration among the Norwegian Institute of Marine Research (HI), the Norwegian Meteorological Institute (MET Norway) and SINTEF Digital, and aims to prepare next-generation ocean forecast systems that provide personalised ocean forecasts in coastal zones. This PhD project was carried out within the frame of the *havvarsel* project and builds academically on the work of Holm [72], which was carried out during the previous *GPU Ocean* project. In the preceding project, a GPU-accelerated simplified ocean model that runs for real conditions of the Norwegian coast was implemented and state-of-the-art data assimilation methods for drift trajectories were explored. As technical results of the *havvarsel* project, a two-way data flow system has been established which handles up- and download of individual ocean observations and the topic of ocean forecasting is presented to the public on the web page `https://havvarsel.no`. Complementary, this PhD project focuses on the research and the fundamental development of simplified models and associated data assimilation techniques that are necessary to incorporate such data to improve local forecasts in the future. To demonstrate how decision-support can be advanced, SAR scenarios are considered in this thesis.

Outline The remainder of this thesis is structured as follows. First, Chapter 2 presents the simplified ocean models used throughout this thesis, expounding the shallow-water equations, numerical methods for solving them, and drift trajectory modelling. The Monte Carlo approach to quantify inherent uncertainty by ensembles is explained in Chapter 3 and Chapter 4 introduces ensemble-based data assimilation methods. Here, the data assimilation problem is stated, followed by a discussion of particle filters and ensemble Kalman filters that strive to modify uncertainty realistically in the forecasts. Chapter 5 explains multi-level Monte Carlo estimation along with the multi-level version of the ensemble Kalman filter. Chapter 6 summarises the contributions made in the attached papers and Chapter 7 concludes with a general summary and an outlook.

Chapter 2

Simplified Ocean Models

In the context of geophysical fluid dynamics, mathematical modelling aims at describing the flow processes and relies on the principles of conservation laws, i.e. conservation of mass, momentum, internal energy, and tracer quantities. While the Reynolds-averaged Navier-Stokes equations serve as a starting point when studying ocean dynamics [63], additional approximations are commonly introduced. The hydrostatic approximation assumes that the horizontal scale is large compared to the vertical scale[1], while the Boussinesq approximation assumes the incompressibility of ocean water. These approximations lead to the formulation of the primitive equations for the ocean dynamics. For most operational forecasts, the primitive equations are solved in one way or another by fully three-dimensional circulation models such as ROMS [123], NEMO [97], or HYCOM [11].

These models find also application in the operational forecasting systems of MET Norway. For instance, the TOPAZ system encompasses the North Atlantic region with a resolution of 12–16 km [119], while the NorKyst model is nested into the TOPAZ domain to cover specifically the Norwegian coast, offering a higher resolution of 800 m [2]. NorKyst is the main operational forecast tool for the Norwegian coastal area and is set up with boundary and forcing information from several sources and with 35 vertical layers. In addition, NorFjord forecasts, that are nested into NorKyst, can provide a 160 m resolution, but are not available operationally [1]. Moreover, specialised products can integrate additional services like a sea ice model for Arctic waters [115]. Given the complexity of these models and their computational requirements, supercomputer in-

---

[1] In the perspective of the hydrostatic approximation, the ocean is shallow while a glass of water is deep.

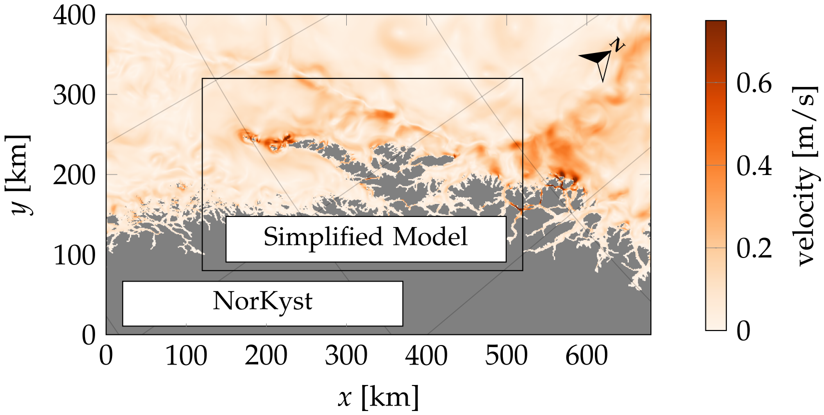

Figure 2.1: NorKyst is the ROMS-based model for the coast of Norway. Simplified models can be nested into its domain locally. Here, we show a cut-out for the Lofoten area in Northern Norway.

frastructure has to be employed, and model runs are typically scheduled only once or twice a day.

These operational forecasts are the backbone of the ocean forecast services [132]. However, when it comes to capturing information of high spatial resolution on-demand, one has to compete for additional computational resources beyond the allocated slots for the scheduled runs. This can take time and these efforts are often limited to a single high-detail deterministic forecast.

Simplified models provide a complementary approach: While they do not attempt to produce the most detailed dynamics, these models are only valid for short-term physics and can be run efficiently. The resolution can be increased for improved representation of local conditions and the models can run on-demand as no large clusters are needed. Simplified models for the Norwegian coast can be nested locally into NorKyst, see Figure 2.1. Then, the simplified model inherits features from NorKyst through the initialisation or from the boundary. Simplified models are less complex and potentially only two-dimensional, such that they can run on conventional computers, for example on board of a vessel.

2.1 Shallow-Water Equations

The primitive equations of ocean dynamics can be further simplified by assuming constant density and by integrating the variables over the full

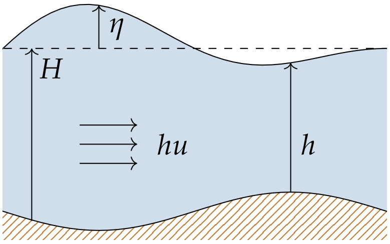

Figure 2.2: Cross section explaining the variables of the shallow-water equations. The momentum hu is the current u integrated over the entire water column $h = H + \eta$, where H is an equilibrium depth and η is the deviation from this equilibrium.

water column, see e.g. [114]. This results in the formulation of the *shallow-water equations (SWE)* within a rotating frame of reference, which constitutes our simplified ocean model in all our further studies. The rotational SWE takes into account the Coriolis force that arises due to the Earth's rotation.

We consider the equilibrium water depth H and the deviation from this equilibrium η, such that the total water column height becomes $h = H + \eta$. The velocities in x- and y-direction are denoted as u and v, respectively (see Figure 2.2). Then the SWE can be expressed as

$$\begin{bmatrix} \eta \\ hu \\ hv \end{bmatrix}_t + \begin{bmatrix} hu \\ hu^2 + \frac{1}{2}gh^2 \\ huv \end{bmatrix}_x + \begin{bmatrix} hv \\ huv \\ hv^2 + \frac{1}{2}gh^2 \end{bmatrix}_y = \begin{bmatrix} 0 \\ fhv \\ -fhu \end{bmatrix} + \begin{bmatrix} 0 \\ ghH_x \\ ghH_y \end{bmatrix}, \quad (2.1)$$

where g is the gravitational force and f the Coriolis parameter. These equations encapsulate the two-dimensional dynamics governed by the evolution of the sea surface elevation and the momenta (hu and hv), where the source terms on the right-hand side account for the effects of the Coriolis force and the variations in the bottom topography. In practice, further source terms can be added, accounting for atmospheric pressure forcing, bed friction, wind stress, and so on.

A lake-at-rest with flat surface and no flow constitutes a trivial example of a steady-state solution to the SWE. However, in the presence of Coriolis forces, an important class of equilibria is described by *geostrophic balance*, where the Coriolis force balances the pressure gradient. This concept yields non-trivial rotating steady state solutions. As the SWE capture the Coriolis force as a source term and the pressure forces from the slope of the free surface, they have the conceptual capability to sustain solutions of the type

$$fhv = gh\frac{\partial \eta}{\partial x} \quad \text{and} \quad fhu = -gh\frac{\partial \eta}{\partial y} \tag{2.2}$$

over time. Geostrophic balance plays a significant role in physical oceanography [134] and will arise in several of the examples throughout the thesis.

High-Resolution Finite-Volume Methods

The SWE are a non-linear hyperbolic conservation law. With the vector of conserved variables $\mathbf{q} = [\eta, hu, hv]^\top$, the SWE can be expressed in vectorised form as

$$\mathbf{q}_t + \mathcal{F}(\mathbf{q})_x + \mathcal{G}(\mathbf{q})_y = S(\mathbf{q}). \tag{2.3}$$

Here, $\mathcal{F}(\mathbf{q})$ and $\mathcal{G}(\mathbf{q})$ represent the flux functions in the x- and y- direction, respectively, and $S(\mathbf{q})$ denotes the source terms. To numerically solve this system, we employ *finite-volume methods* (FVM), which are designed to preserve physical properties of the original equations, i.e. FVMs can be composed to be conservative, see e.g. [133, 92, 102]. In our setting, we discretise the computational domain into a regular Cartesian grid of size $n_x \times n_y$, with each grid cell representing a control volume of dimensions $\Delta x \times \Delta y$. Then, we define $\mathbf{Q}_{j,k}$ as the average of the conserved variables $\mathbf{q}$ over the cell $\Gamma_{j,k}$ with the indices (j, k) in the grid. We omit additional time notation as long as it is not strictly necessary.

With Gauss's theorem, eq. (2.3) can be rephrased into its integral form

$$\frac{\partial \mathbf{Q}_{j,k}}{\partial t} = -\int_{\partial \Gamma_{j,k}} \mathcal{F}(\mathbf{q}) \cdot \mathbf{n}_x \, \mathrm{d}s - \int_{\partial \Gamma_{j,k}} \mathcal{G}(\mathbf{q}) \cdot \mathbf{n}_y \, \mathrm{d}s + S(\mathbf{Q}_{j,k}), \tag{2.4}$$

where the integrals are evaluated over the boundary of the cell and $\mathbf{n}_x$ and $\mathbf{n}_y$ are x- and y-contribution of the outer normal vector of the cell, respectively.

FVMs utilise the integral form of eq. (2.3) and approximate the spatial derivatives by the differences of the fluxes over opposite cell interfaces. With numerical fluxes $\mathbf{F}$ and $\mathbf{G}$, which approximate the flux terms over the cell interfaces in x- and y-direction, respectively, the semi-discrete approximation to eq. (2.3) becomes

$$\frac{\partial \mathbf{Q}_{j,k}}{\partial t} = -\frac{\mathbf{F}_{j+1/2,k} - \mathbf{F}_{j-1/2,k}}{\Delta x} - \frac{\mathbf{G}_{j,k+1/2} - \mathbf{G}_{j,k-1/2}}{\Delta y} + S(\mathbf{Q}_{j,k}). \tag{2.5}$$

This is a set of ordinary differential equations that describes the evolution of the cell averages in time and is a fundamental building block for many modern FVMs.

One approach to proceed from eq. (2.5) is to utilise the so-called REA-algorithm, which involves three key steps: reconstruction, evolution and averaging. First, a polynomial is reconstructed per cell which enables a better representation of the underlying functions. This provides also point values on the interfaces for the evaluation of the numerical fluxes. Next, the equations are evolved in time using appropriate time integration schemes. Lastly, the FVM representation is again obtained by averaging the results over the grid cells.

As geostrophic balance is a central concept in oceanography, special effort is exerted in the design of the FVMs to guarantee that also the numerical solutions preserve these steady states. Such FVMs are then called *well-balanced*. Well-balanced schemes are a wider class of FVMs, but we are particularly interested in those that are well-balanced with respect to an instance of geostrophic balance.

In this thesis, we touch on two well-balanced FVMs for the SWE. These are high-resolution schemes of second order that are derived from the REA-algorithm. The first method by Kurganov and Petrova (KP, [87]) is constructed to be well-balanced for the lake-at-rest case, even in the presence of discontinuous bottom topography. KP employs linear reconstruction on the conserved variables and finds slopes using the generalised minmod limiter [95]. The numerical fluxes are then evaluated by the central-upwind scheme [88].

The second scheme by Chertock et al. (CDKLM, [25]) is similar to KP, but it extends the well-balanced property to a larger subset of rotating equilibria. It is proposed for a special case of non-trivial geostrophic jets along the coordinate axes, including the trivial lake-at-rest case. In contrast to KP, the reconstruction is based on potential energies with respect to the geostrophic imbalance and further, to obtain the well-balance for the jets, the components of **F** and **G** that embrace the *huv*-term are evaluated with a standard upwind scheme.

For the evolution in time, both methods employ the explicit second-order total-variation-diminishing Runge-Kutta scheme for the time evolution [60], whose time step size Δt is restricted by the Courant-Friedrich-Levy (CFL)-condition, given by

$$\Delta t \leq \frac{C}{4} \min_{j,k} \left\{ \frac{\Delta x}{\max \left| u_{j,k} \pm \sqrt{g h_{j,k}} \right|}, \frac{\Delta y}{\max \left| v_{j,k} \pm \sqrt{g h_{j,k}} \right|} \right\}, \tag{2.6}$$

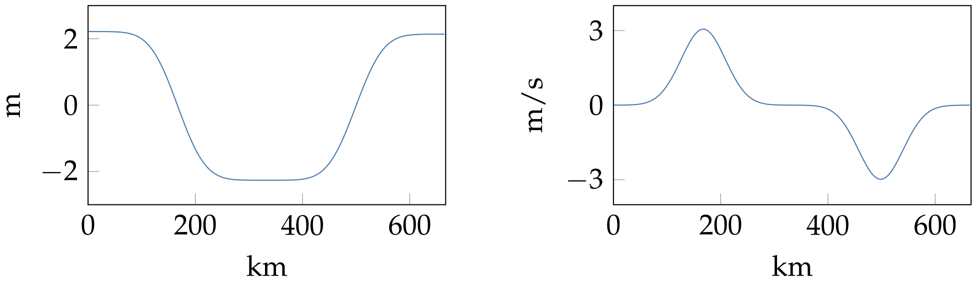

(a) η **(b)** u

Figure 2.3: Cross section along the y-axis through exemplary initial conditions of the synthetic SWE experiment. Note that $v = 0$.

where $C < 1$ is the Courant number and grid values come from $[\eta_{j,k}, hu_{j,k}, hv_{j,k}]^\top = \mathbf{Q}_{j,k}$.

Finally, to solve eq. (2.1), it is necessary to combine the SWE with appropriate initial and boundary condition. In the context of simplified ocean simulations, the initial conditions are imposed from operational models without spin-up phase at the starting time of the simulation. Analogously, the boundary conditions are set over the time span of the simulation from the operational forecast data, where a flow relaxation scheme accounts for the origin from a mismatching model [33].

Synthetic SWE Experiment Throughout the contributions of this thesis, we consider the so-called double jet case to test numerical schemes and data assimilation methods. Galewsky et al. [51] suggested a test case for numerical solvers for the SWE on a rotating frame of reference. The case starts from an initial steady state in form of a jet, but the system is unstable in the sense that a small perturbation leads to turbulent behaviour. The set-up was extended by Holm et al. [76] by a second jet in the opposite direction and periodic boundary conditions. With that, the case gets more demanding and creates near-realistic currents. The state is described by a westward jet in the north and an eastward jet in the south, both along the coordinate axes. The initial conditions, see Figure 2.3 for an example, are designed to be in geostrophic balance and the example is therefore within the subset for which the CDKLM scheme is well-balanced. Due to its chaotic response to perturbations, the synthetic double jet case serves also as a challenging test case for data assimilation scenarios in the remainder of this thesis.

GPU OCEAN Code Base

While central processing units (CPUs) serve as the primary general-purpose units of a computer system responsible for executing instructions and performing calculations, graphics processing unit (GPUs) can be used to accelerate computations through massive parallelisation. The GPU was originally developed to accelerate and enhance the rendering and displaying of visual content and are therefore designed to handle typical computations on a grid of pixels in a highly parallel manner. As GPUs became programmable, the potential of parallelism could be harvested for general-purpose scientific computing tasks beyond graphics processing [14]. Whereas CPUs typically consist of dozens of computational cores, modern GPUs consist of several thousands of simpler cores operating in the 'single-instruction, multiple-data' paradigm of parallel computing. This means that GPUs excel at problems that can be solved through embarrassingly parallel algorithms, where the same instruction set can be applied to a large set of input data to produce output that is independent from other output values [16].

Due to the explicit time-stepping used to solve eq. (2.1), the FVMs for simulating the SWE are perfect examples of parallel algorithms that are well-suited for GPU accelerations [66, 127, 74]. Over the recent years, the Applied Computational Sciences group (formerly Computational Geosciences group) at SINTEF Digital, together with the Ocean and Ice research unit at MET Norway, have developed the GPU OCEAN code base as tool for simplified ocean forecasts. Therefore, the simulation framework includes among others GPU-accelerated implementations of the KP and CDKLM schemes for the efficient simulation of the SWE and supports realistic scenarios by allowing initialisation from operational ocean forecasts, such as NorKyst or similar models, and handling domains with land masks. Furthermore, the capabilities include fetching boundary conditions and deriving forcing terms for wind and atmospheric pressure from operational models. Furthermore, the framework offers the flexibility to adjust the resolution independent of the initial data resolution, accommodates for ensemble simulations and enables the integration of data assimilation.

Computational Efficiency

The SWE, as simplified two-dimensional ocean model, are designed for specific ocean processes and treat some of the physical complexity in favour of computational efficiency. Still, the SWE can inherit dynamics from the complex models through initial and boundary conditions and preserve

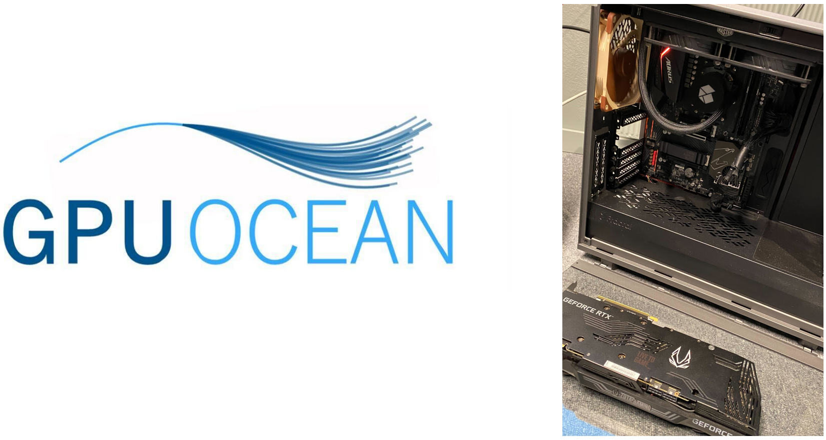

Figure 2.4: GPU Ocean logo and picture of the GeForce RTX3090 GPU, which was used for most of the experiments in this thesis, taken on 11.09.2023 after it burnt through.

structural patterns to some extent. Moreover, the efficient implementation on GPUs makes the SWE a complementary special-purpose tool for shorter time spans.

In this work, the GPU Ocean framework has extensively been used for the simulation of simplified forecasts such that a operating GPU set-up was vital, see Figure 2.4. While a NorKyst simulations takes about 1 h 7 min (v2, 512 cores) or 3 h 30 min (v3, 128 cores) on the 'Stratus' cluster at the National Supercomputer Centre, Linköping University, the GPU Ocean simulation of the same domain and time span takes 1 min 13 s on a GeForce RTX3090, which is an advanced GPU series, or 10 min 48 s on a Quadro T2000, which is a more standard laptop GPU.

Reduced computational time due to accelerated models yields furthermore a cut of financial costs. Considering that financial expenses for the computations are effectuated by number of hours of node usage, more efficient methods reduce the associated price, whereas parallelisation only reduces the wall time but not the total node occupancy. Beyond the financial impact, decreased computational requirements sparse the need for extra hardware resources. This dual effect underscores advantages of efficient computational methods seen from an alternative perspective.

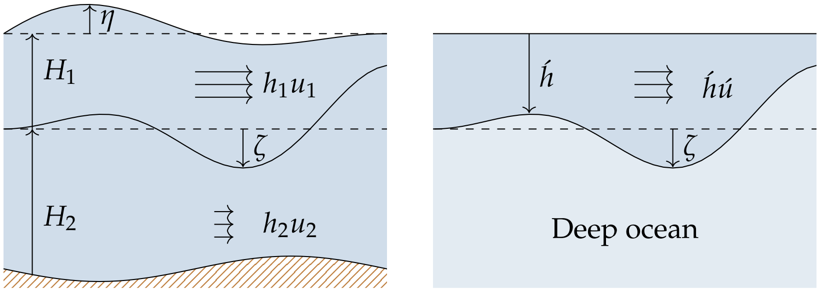

(a) Two-layer shallow-water model **(b)** Baroclinic shallow-water model

Figure 2.5: Schematic cross sections for the two-layer shallow-water and the baroclinic shallow-water model with schematic explanation of the variables.

2.2 Barotropic and Baroclinic Modelling

The integration of the primitive equations over a constant-density water column leads to a pressure depending solely on the depth. As a result, the SWE presented in eq. (2.1) serve as a textbook model for *barotropic* ocean dynamics [113]. This captures, for example, tidal signals or Rossby waves and finds practical applications in scenarios like storm surge forecasting [85]. However, this model ignores *baroclinic* dynamics, which is driven by pressure gradients that are not aligned with the density gradient. Seawater density typically increases with depth and it depends on temperature as well as salinity. The latter quantities vary across space in the ocean leading to varying density profiles for different locations. In particular, protected fjords exhibit a distinct stratification, meaning that a shallow upper layer of lower density ρ_1 and a deep lower layer of higher density ρ_2 are separated by a sharp transition [31].

Determining a mixed-layer depth (MLD), that separates the low density layer on top from the high density region below, a two-layer shallow-water ocean model can be formulated as

$$\begin{aligned}\begin{bmatrix} h_1 \\ h_1u_1 \\ h_1v_1 \end{bmatrix}_t + \begin{bmatrix} h_1u_1 \\ h_1u_1^2 + \frac{1}{2}gh_1^2 \\ h_1u_1v_1 \end{bmatrix}_x + \begin{bmatrix} h_1v_1 \\ h_1u_1v_1 \\ h_1v_1^2 + \frac{1}{2}gh_1^2 \end{bmatrix}_y \\ = \begin{bmatrix} 0 \\ fh_1v_1 \\ -fh_1u_1 \end{bmatrix} + \begin{bmatrix} 0 \\ gh_1H_x \\ gh_1H_y \end{bmatrix} + \begin{bmatrix} 0 \\ -gh_1(h_2)_x \\ -gh_1(h_2)_y \end{bmatrix} \qquad \text{(2.7a)}\end{aligned}$$

$$\begin{bmatrix} h_2 \\ h_2u_2 \\ h_2v_2 \end{bmatrix}_t + \begin{bmatrix} h_2u_2 \\ h_2u_2^2 + \frac{1}{2}gh_2^2 \\ h_2u_2v_2 \end{bmatrix}_x + \begin{bmatrix} h_2v_2 \\ h_2u_2v_2 \\ h_2v_2^2 + \frac{1}{2}gh_2^2 \end{bmatrix}_y$$
$$= \begin{bmatrix} 0 \\ fh_2v_2 \\ -fh_2u_2 \end{bmatrix} + \begin{bmatrix} 0 \\ gh_2H_x \\ gh_2H_y \end{bmatrix} + \begin{bmatrix} 0 \\ -rgh_2(h_1)_x \\ -rgh_2(h_1)_y \end{bmatrix}. \tag{2.7b}$$

This is a coupled system of shallow-water equations for both layers where $r = \rho_2/\rho_1$, see Figure 2.5a, where $H = H_1 + H_2$ and h_1, h_2 are the depth of the upper and lower layer, respectively. However, such a system is no longer unconditionally hyperbolic [21] and the FVM schemes implemented in GPU OCEAN are not sufficient to solve eq. (2.7) on GPUs [35]. Even though the system in eq. (2.7) has the abilities of barotropic as well as baroclinic responses, we follow Røed [114] and continue to isolate the baroclinic response by employing the rigid-lid assumption, meaning that we set $\eta = 0$. By adding the mass conservation equations from eqs. (2.7a) and (2.7b), this requires

$$h_1u_1 = -h_2u_2 \quad \text{and} \quad h_1v_1 = -h_2v_2, \tag{2.8}$$

and the mass conservation reduces to

$$\zeta_t + (h_1u_1)_x + (h_1v_1)_y = 0. \tag{2.9}$$

Lastly, we assume an infinitely deep lower level which implies that we neglect currents in the lower layer, i.e. $u_2, v_2 = 0$ using eq. (2.8). This yields that the equations for the upper layer become decoupled and the momentum equations of the lower layer reduce to

$$\left(\frac{1}{2}gh_2^2\right)_x = gh_2H_x - rgh_2(h_1)_x \quad \text{and} \quad \left(\frac{1}{2}gh_2^2\right)_y = gh_2H_y - rgh_2(h_1)_y. \tag{2.10}$$

With the chain rule, the terms $(h_2)_x$ and $(h_2)_y$ can be extracted and plugged into the force terms of the upper layer.

The resulting so-called 1.5-layer shallow-water model boils down to the same type of mathematics as the barotropic shallow-water model in eq. (2.1). With the baroclinic variables as in Figure 2.5b, the model reads

$$\begin{bmatrix} \zeta \\ \acute{h}\acute{u} \\ \acute{h}\acute{v} \end{bmatrix}_t + \begin{bmatrix} \acute{h}\acute{u} \\ \acute{h}\acute{u}^2 + \frac{1}{2}\acute{g}\acute{h}^2 \\ \acute{h}\acute{u}\acute{v} \end{bmatrix}_x + \begin{bmatrix} \acute{h}\acute{v} \\ \acute{h}\acute{u}\acute{v} \\ \acute{h}\acute{v}^2 + \frac{1}{2}\acute{g}\acute{h}^2 \end{bmatrix}_y = \begin{bmatrix} 0 \\ f\acute{h}\acute{v} \\ -f\acute{h}\acute{u} \end{bmatrix}, \tag{2.11}$$

where the gravity is reduced according to

$$\acute{g} = \frac{\rho_2 - \rho_1}{\rho_2} g \tag{2.12}$$

and the forcing from the bathymetry cancel out. Due to eq. (2.12), the system is also called 'reduced-gravity model' and we use it as a simplified model for the baroclinic dynamic in the ocean. Note that we initialise the reduced-gravity model with the baroclinic currents in the mixed layer $\acute{u} = u_1 - u$ and $\acute{v} = v_1 - v$ for consistency, but this is different to the model of Røed [114]. Moreover, the reduced depth of the water column and reduced gravity leads to significantly reduced phase speeds $(\acute{g}\acute{h})^{1/2}$ in the CFL-condition in eq. (2.6), such that larger time steps are achievable and the system can be solved very efficiently in GPU Ocean.

2.3 Trajectory Modelling

Drift trajectory predictions are, for example, important in SAR missions, but also for collision forecasts of icebergs with offshore facilities or oil spill clean-up. Hereby, the drift properties heavily depend on the shape of the object, how deep the object is submerged into the ocean, and how it orients relative towards the wind. For such incidents in Norwegian waters, trajectories are computed with the OpenDrift software package [30]. Therewith, the forecast outputs from operational models, which commonly have a 1 h time resolution, are read in and trajectories are separately but rapidly simulated using a suitable module in the OpenDrift framework. Such workflows use the ocean models offline, meaning that the currents are not on-the-fly updated according to the latest observations. Drift trajectory prediction based on simplified models enables us to also update the ocean states whenever additional data becomes available.

In GPU Ocean, the drift modelling is integrated into the SWE simulation, meaning that the drifter locations are updated during the simulation. Drifters are passively advected using the currents u and v interpolated from the relevant grid cells. Additionally, a drift contribution from wind fields can be considered.

Let $\boldsymbol{\psi}^t \in \mathbb{R}^2$ represent the location of a floating object within the computational domain at time t. Further, we denote the bi-linearly interpolated velocities by $u(t, \boldsymbol{\psi}^t)$ and $v(t, \boldsymbol{\psi}^t)$ where the interpolation is defined over the grid cell that contains $\boldsymbol{\psi}^t$ and three of its neighbours. Then, the drifter locations are advanced for the time step Δt_{drift}, commonly chosen to be the same as the simulator time step Δt, according to

$$\boldsymbol{\psi}_0^{t+\Delta t_{\text{drift}}} = \boldsymbol{\psi}_0^t + \Delta t_{\text{drift}} \left(u(t, \boldsymbol{\psi}^t) + \text{wind}_u(t, \boldsymbol{\psi}^t)\right) \tag{2.13a}$$

$$\boldsymbol{\psi}_1^{t+\Delta t_{\text{drift}}} = \boldsymbol{\psi}_1^t + \Delta t_{\text{drift}} \left(u(t, \boldsymbol{\psi}^t) + \text{wind}_v(t, \boldsymbol{\psi}^t)\right), \tag{2.13b}$$

where $\text{wind}_u, \text{wind}_v$ are contributions from the wind relative to the water velocity. This is not the wind field directly but a function of the wind field.

Chapter 3

Ensemble Forecasts

Numerical simulations are a powerful pillar in the generation of ocean forecasts, but even complex models are only an approximation of reality such that the generated predictions contain inherent uncertainty. To quantify the uncertainty, we consider statistical interpretation from a Bayesian perspective and ensemble prediction systems (EPS) [91, 130, 34]. An ensemble is a set of ocean simulations with slight perturbations and, for example, the Barents-2.5 model of MET Norway is composed of 24 ensemble members [81].

In general, larger ensembles are preferable for more realistic statistical representation, but the ensemble size is limited by available computational resources. Since the SWE are computationally highly efficient, they allow to run ensembles with a bigger number of simulations. This means that we invest the computational gain through the simplification into enhanced statistical power and this is useful for reliable uncertainty quantification.

3.1 Sources of Uncertainty

In the process of mathematical modelling and numerical simulation in Chapter 2, we imposed a series of simplifications and incorporated parameters that are not perfectly known in real-world applications. Likewise, initial conditions and additional forcing terms may be only poorly known. This requires appropriate statistical representation in the forecast system.

To describe the state of a simplified ocean model, we use the *state vector* $\boldsymbol{x} \in \mathbb{R}^{N_X}$. For the SWE model, the state vector collects all the variables over all spatial grid cells at a certain time t, i.e.

$$\boldsymbol{x}(t) = \big(\mathbf{Q}_{j,k}(t)\big)_{j,k=1}^{nx,ny} \tag{3.1}$$

such that $N_X = 3 \cdot nx \cdot ny$. Therewith, the state vector is naturally high-dimensional. The Bayesian paradigm accounts for the inherent uncertainty by prescribing distributions, such that the state vector is interpreted as stochastic process.

Here, the uncertainty begins with the initial conditions $\boldsymbol{x}(t^0) = \boldsymbol{x}^0$. The actual state of the ocean at time t^0 is commonly inaccessible or only partially known. Data from operational systems can provide information to set $\boldsymbol{x}^0$ for the SWE, where the operational forecast already includes uncertainty.

For the evolution of the states in time, we embrace the numerical SWE model into the operator $\mathcal{M}^{t^0 \to T}$, which forwards the ocean state from time t^0 to time T. To account for the uncertainty in this temporal evolution, two conceptually distinct statistical modelling approaches can be considered.

First, the simplified models represent only an idealised version of the oceanographic reality and the numerical solution is again only an approximation of the continuous model. To account for unresolved physics, we add an additive error term $\boldsymbol{\epsilon}$ to get

$$\boldsymbol{x}(T) = \mathcal{M}^{t^0 \to T}(\boldsymbol{x}^0) + \boldsymbol{\epsilon}(\omega), \tag{3.2}$$

where ω denotes an element of a sample space. Here, one can include features into the model error that are not captured by the model equations.

Second, the uncertainty in the model involves the parametrisation of every single forcing term in the problem formulation. Hence, we consider these values as random variables and can sample them from appropriate distributions. This then means that we consider a set of random model parametrisations by

$$\boldsymbol{x}(T) = \mathcal{M}^{t^0 \to T}(\boldsymbol{x}^0, \omega) \tag{3.3}$$

such that the randomness gets directly incorporated into the model operator.

Note that model error is a design choice and should respect realistic conditions, while still being efficient to sample. In particular, we use structures for $\boldsymbol{\epsilon}$ that add random small-scale eddies onto the SWE states, where the eddies are chosen in such a way such that extensive gravity waves are avoided.

The conceptual difference between the model error ansatzes is illustrated in Figure 3.1. The distribution of states with the implicit model error is propagated and transformed through the model equations as visualised in the left display. In the right display, the additive model error determines the distribution of states around the deterministic simulation at time T and

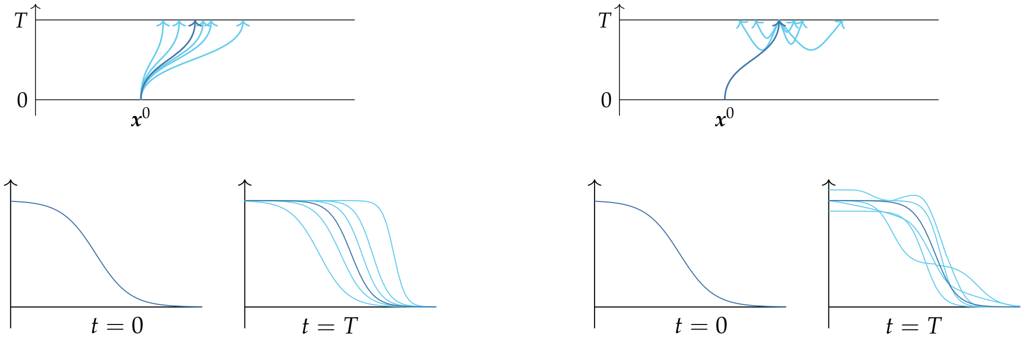

(a) Implicit model error

(b) Additive model error

Figure 3.1: The stochastic model error can be incorporated into the model forecasts implicitly or additively. The dark curve represents a deterministic simulation. The upper row depicts the timing when the model error shows effect. The lower row shows an idealised illustration of a travelling wave. The implicit model error perturbs parameters in the model evolution such that all realisations still come from the modelled physics. Conversely, the additive model error allows the inclusion of unresolved features at time T.

its characteristics has to be known a priori. In the lower panels, we also consider a travelling wave to illustrate effects that come with the disparity of the two model error formulations with respect to the introduced features. However, we remark also that the additive model error can be applied with shorter time steps during the simulation from 0 to T. In that case, model error features can develop distinct dynamics over time and the distribution of states at time T is no longer a priori determined. Note that it is also possible to combine both approaches.

3.2 Uncertainty Quantification

In forecast scenarios, it is of interest to quantify the influence of uncertainty represented in the inputs and the model itself onto the final ocean states. While a single deterministic forecast does not provide a comprehensive uncertainty description, a fully probabilistic forecast for the states $\boldsymbol{x}$ with a continuous probability density function (PDF, p) is inaccessible for complex models. If p was available and the following high-dimension integral was solvable, the expected value defined by

$$\mathbb{E}\left[\boldsymbol{x}\right] = \int \boldsymbol{x} \cdot p(\boldsymbol{x}) \, \mathrm{d}\boldsymbol{x} \tag{3.4a}$$

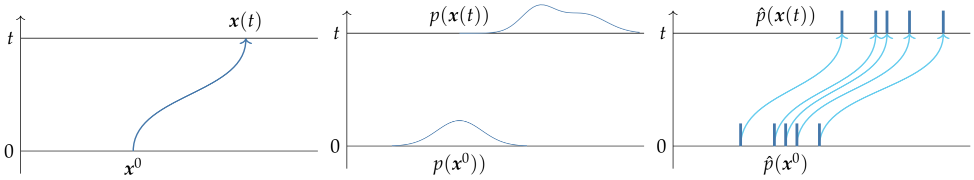

(a) Deterministic forecast **(b)** Probabilistic forecast **(c)** Ensemble forecast

Figure 3.2: Schematic depiction of different forecast types

or the covariance of the state with some random vector $\boldsymbol{y} \in \mathbb{R}^{N_Y}$ defined by

$$\mathrm{Cov}\left[\boldsymbol{x},\boldsymbol{y}\right] = \mathbb{E}\left[(\boldsymbol{x} - \mathbb{E}\left[\boldsymbol{x}\right])(\boldsymbol{y} - \mathbb{E}\left[\boldsymbol{y}\right])^\top\right], \tag{3.4b}$$

where also the associated PDF of $\boldsymbol{y}$ is assumed to be known, would be two examples of extracting information from a fully probabilistic forecast.

In contrast to both deterministic and fully probabilistic forecasts, *Monte Carlo* methods rely on repeated sampling of an experiment and are one practical approach to provide forecasts together with the associated statistical uncertainty. In this setting, an *ensemble* is a set of N_e state vectors $(\boldsymbol{x}_e)_{e=1}^{N_e}$, where all ensemble members $\boldsymbol{x}_e$ are independent samples of the same model.

In the Monte Carlo setting, an underlying PDF p is approximated by the ensemble representation with discrete PDF $\hat{p}$. The ensemble approximation of the marginal distribution of $\boldsymbol{x}$ becomes

$$\hat{p}(\boldsymbol{x}) = \sum_{e=1}^{N_e} w_e \delta(\boldsymbol{x} - \boldsymbol{x}_e), \tag{3.5}$$

where $(w_e)_{e=1}^{N_e}$ are weights that sum up to 1 and δ is the Dirac delta function. Starting from uncertain initial conditions x^0 with a given distribution, an ensemble forecast is generated by evolving all ensemble members independently in time. The concept of ensemble-based forecasts in contrast to deterministic and probabilistic forecasts is illustrated in Figure 3.2.

Further, the ensemble members can be used to estimate statistical quantities like the first and second moments at certain times. With equal weights $w_e = 1/N_e$ for all members $e = 1, \ldots, N_e$, the expected value in eq. (3.4a) can be estimated by the sample average

$$\mathrm{E}\left[\boldsymbol{x}\right] = \frac{1}{N_e} \sum_{e=1}^{N_e} \boldsymbol{x}_e, \tag{3.6}$$

which is a vector in $\mathbb{R}^{N_X}$, and using a corresponding ensemble $(\boldsymbol{y}_e)_{e=1}^{N_e}$ with equal weights, the covariance $\mathbb{C}\mathrm{ov}$ in eq. (3.4b) is approximated by

$$\mathrm{Cov}\left[\boldsymbol{x}, \boldsymbol{y}\right] = \frac{1}{N_e - 1} \sum_{e=1}^{N_e} \left(\boldsymbol{x}_e - \mathrm{E}\left[\boldsymbol{x}\right]\right) \left(\boldsymbol{y}_e - \mathrm{E}\left[\boldsymbol{y}\right]\right)^\top, \tag{3.7}$$

which is a matrix in $\mathbb{R}^{N_X \times N_Y}$. The variance $\mathbb{V}\mathrm{ar}\left[\boldsymbol{x}\right]$ is approximated by the diagonal of $\mathrm{Cov}\left[\boldsymbol{x}, \boldsymbol{x}\right]$, which is denoted as $\mathrm{Var}\left[\boldsymbol{x}\right] \in \mathbb{R}^{N_X}$. In the case of arbitrary weights, the mean is estimated by

$$\mathrm{E}\left[\boldsymbol{x}\right] = \sum_{e=1}^{N_e} w_e \boldsymbol{x}_e, \tag{3.8}$$

and the covariance of $\boldsymbol{x}$ with itself is estimated by

$$\mathrm{Cov}\left[\boldsymbol{x}, \boldsymbol{x}\right] = \frac{1}{1 - \sum_{e=1}^{N_e} w_e^2} \sum_{e=1}^{N_e} w_e \left(\boldsymbol{x}_e - \mathrm{E}\left[\boldsymbol{x}\right]\right) \left(\boldsymbol{x}_e - \mathrm{E}\left[\boldsymbol{x}\right]\right)^\top. \tag{3.9}$$

From these estimators for the full state vector, statistics for variables of interest can be derived by selecting the corresponding dimensions. For example for the ocean currents in the SWE model, the statistics can be estimated through its mean $\mathrm{E}\left[u\right], \mathrm{E}\left[v\right]$ and variance $\mathrm{Var}\left[u\right], \mathrm{Var}\left[v\right]$, which are vectors of the same dimension as the computational grid and can be directly visualised.

Monte Carlo estimators are approximations to the true, but inaccessible, expected value and covariance, respectively, and the statistical accuracy of the estimates generally improves for a larger effective number of samples. Hence, larger ensembles with more members are preferable for the quantification of the uncertainty. In ocean forecasting, each Monte Carlo sample corresponds to the simulation of an instance of an ocean model. Since the ensemble size of complex models is limited by the available time budget and computational resources, operational systems provide commonly only a single forecast or a small ensemble. As seen in Section 2.1, the SWE model is computationally more efficient, such that we can afford an increased number of experiments and larger ensembles.

Exemplary, we consider an ensemble of with 500 SWE members for the double jet case from Section 2.1. Each member is initialised by the same initial conditions and evolved by the SWE model for 10 d, where the simulations are perturbed every 1 min with some small additive model error. Then, Figure 3.3 shows the mean velocity in the upper row, meaning $(\mathrm{E}\left[u\right]^2 + \mathrm{E}\left[v\right]^2)^{1/2}$, and velocity fields for two ensemble members in the

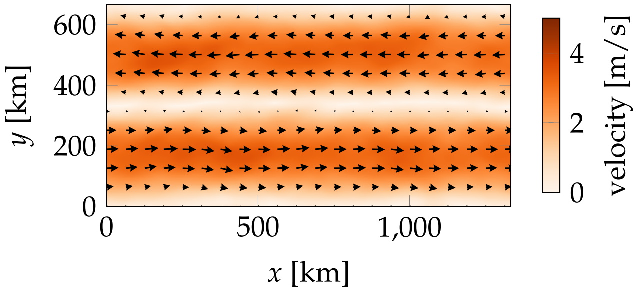

(a) Ensemble mean

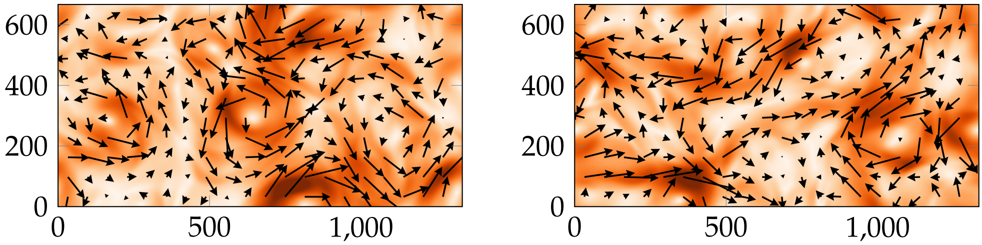

(b) Ensemble member $e = 1$

(c) Ensemble member $e = 2$

Figure 3.3: Velocities in a ensemble of double jet simulations. The mean is calculated over 500 ensemble members.

lower row. Clearly, the single ensemble members develop turbulent current structures while the mean has a regular pattern reflecting smeared initial conditions.

Ensemble Trajectory Modelling

In our application, the ensemble of ocean states supplies an ensemble of drift trajectories $(\boldsymbol{\psi}_d)_{d=1}^{N_d}$ for some drifter ensemble size N_d. We consider two distinct approaches for the modelling of ensemble trajectories, where both can be integrated into the simulation routine as generally described in Section 2.3. The first one intrudes into every single simulator of the ensemble, while the second one relies on ensemble statistics.

Trajectories by Ensemble Attachment

The most straightforward method for generating an ensemble of drift trajectories from an ensemble of simplified ocean models, is to simulate one realisation of drift trajectories connected to one ocean model. The drifter locations are updated every time step Δt of the simulator using eq. (2.13) and thee ensemble of drift trajectories is equally large as the ensemble of SWE models, meaning $N_d = N_e$. The advantage of this is that each individual drift trajectory is consistent with respect to the physics of the ocean model, it is computationally inexpensive, and the statistical distribution of the drift trajectories are in accordance with the distribution of the simulated currents.

Trajectories by Ensemble Statistics

In contrast to the previous approach, the members of the ocean model ensemble are not utilised individually in this alternative. Instead, estimates of the ocean currents are computed and these statistics are used to evolve the drifter ensemble. We sample drifter realisations from a Gaussian process that is centred at $(\mathrm{E}\left[u(t,\boldsymbol{\psi}^t)\right], \mathrm{E}\left[v(t,\boldsymbol{\psi}^t)\right])$ and is scaled by $(\mathrm{Var}\left[u(t,\boldsymbol{\psi}^t))\right], \mathrm{Var}\left[v(t,\boldsymbol{\psi}^t))\right])$. Note that the stochastic realisation spans over the entire simulation time for a sample of this process. In this case, the size of the drifter ensemble N_d can be chosen independent from the SWE ensemble size N_e. To ensure that the realisation of modelled path is consistent over time, we first sample a random component for the currents u and v for every drifter member as

$$\delta_{d,u}, \delta_{d,v} \sim \mathcal{N}(0,1) \quad \text{for } d = 1,\dots,N_d \tag{3.10}$$

and keep those fixed for the evolution of the drifter in time. The time steps of the drifter evolution Δt_{drift} is also independent of the simulator time steps, but at relevant time steps the means $\mathrm{E}\left[u(t)\right], \mathrm{E}\left[v(t)\right]$ and variances $\mathrm{Var}\left[u(t)\right], \mathrm{Var}\left[v(t)\right]$ are calculated. The drifter ensemble is then forwarded as

$$\boldsymbol{\psi}_{d,0}^{t+\Delta t_{\text{drift}}} = \boldsymbol{\psi}_{d,0}^{t} + \Delta t_{\text{drift}} \left(\mathrm{E}\left[u(t,\boldsymbol{\psi}_d^t)\right] + \delta_{d,u}\sqrt{\mathrm{Var}\left[u(t,\boldsymbol{\psi}_d^t)\right]} + \mathrm{wind}_u(t,\boldsymbol{\psi}^t) \right) \tag{3.11a}$$

$$\boldsymbol{\psi}_{d,1}^{t+\Delta t_{\text{drift}}} = \boldsymbol{\psi}_{d,1}^{t} + \Delta t_{\text{drift}} \left(\mathrm{E}\left[v(t,\boldsymbol{\psi}_d^t)\right] + \delta_{d,v}\sqrt{\mathrm{Var}\left[v(t,\boldsymbol{\psi}_d^t)\right]} + \mathrm{wind}_v(t,\boldsymbol{\psi}^t) \right) \tag{3.11b}$$

for $d = 1,\dots,N_d$. The currents in eq. (2.13) are replaced by statistical terms. As this approach does not require access to the individual simulations, it is versatile, but assumes intrinsically a Gaussian distribution.

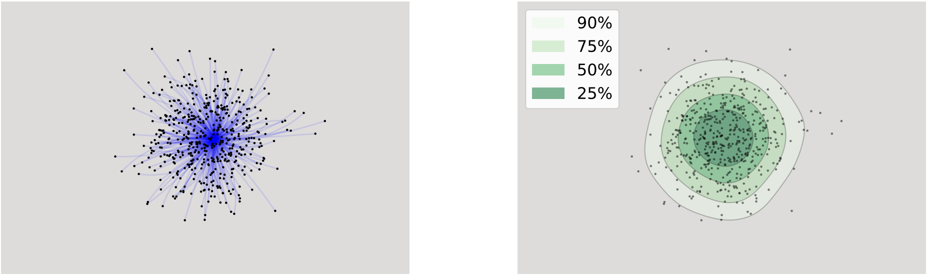

(a) Drifter paths

(b) KDE

Figure 3.4: Ensemble trajectories and visualisation by drifter paths and KDE

Statistical Modelling of Search Areas

In the Monte Carlo setting for drifters, a point cloud together with the trajectories informs about the paths of the drifter ensemble. However, the discrete representation does not necessarily result in comprehensive visualisations for search areas. As the sampled drifter positions represent an approximation to continuous PDFs, kernel density estimation (KDE) can additionally provide a smooth representation based on the discrete samples at a certain time. For example, for huge ensembles of drift trajectories, a kernel-density presentation is more appropriate than a point cloud. With the estimated covariance of the drifter locations $\boldsymbol{\Sigma}_{\boldsymbol{\psi},\boldsymbol{\psi}} = \operatorname{Cov}\left[\boldsymbol{\psi},\boldsymbol{\psi}\right]$ the KDE can be a sum over Gaussian kernels centred at the Monte Carlo samples

$$\hat{p}_{\mathrm{KDE}}(\boldsymbol{\psi}) \propto \sum_{d=1}^{N_d} \exp\left(-\frac{1}{2}(\boldsymbol{\psi}-\boldsymbol{\psi}_d)(\kappa\boldsymbol{\Sigma}_{\boldsymbol{\psi},\boldsymbol{\psi}})^{-1}(\boldsymbol{\psi}-\boldsymbol{\psi}_d)^{\top}\right), \tag{3.12}$$

where κ is the bandwidth and by Scott's rule set as $N_e^{-1/6}$ for a two-dimensional variable [122].

Figure 3.4 pictures the difference between a trajectory plot with drifter paths for every ensemble member from start to end time of the forecast and the KDE of the drifter locations at the final time. The visualised drift trajectory ensemble has 500 members with the same initial position and the black dots mark the drifter locations at the end time of the forecast.

Chapter 4

Data Assimilation

In the previous sections, we have described simplified ocean model and how these can be used to efficiently forecast drift trajectories. Alongside these models and simulations, observation data plays a crucial role in oceanographic forecasts [36]. In this section, we discuss the mathematical framework for how ensembles of numerical models can be updated using such observations through data assimilation.

In general, observations can be obtained from several sources such as satellite images [29], high-frequency radars [126], or buoys [111, 17] and exhibit diverse properties like various resolutions [68]. Similarly to the routines in classical numerical weather prediction, these measurements are utilised in the operational machinery to improve the accuracy of forecasts [98, 107]. However in comparison to the atmosphere, the ocean is only sparsely observed [67]. Operational ocean forecast systems incorporate a wide range of the available observations into the assimilation, but as the models are typically scheduled once or twice a day, the data has to be available before or at least during the run.

In certain time-critical scenarios like SAR missions, additional observations of the real currents can become available during the mission [32]. Such data was not considered in the operational forecasts, as it was likely not yet available during a scheduled run of the computationally intensive models. However, these latest observations can be incorporated into on-demand forecasts with simplified models instead. In this thesis, we consider data from in-situ buoys as these typically take measurements frequently. On the contrary, dozens of kilometres can lie between different buoys, such that the observations are spatially very sparse. Simplified models cannot be expected to resolve all characteristics from general circulation models as there is a natural simplification in the equations and variables in the SWE compared to the complex models, but an SWE ensemble can benefit from frequent updating according to measurements and can thereby be steered towards the true dynamics.

4.1 The Data Assimilation Problem

To get started, we consider a series of time steps t^n, $n = 0, \dots, N_T$ at which new data is assimilated. Without loss of generality those time steps are assumed to be equidistant. Moreover, we denote the state vector at time t^n as $\boldsymbol{x}^n \in \mathbb{R}^{N_X}$. Starting from an ensemble representation of the initial distribution $(\boldsymbol{x}_e^0)_{e=1}^{N_e}$ and assuming that the ensemble has reached time t^{n-1}, we evolve each member from the previous time step t^{n-1} to the current t^n by

$$\boldsymbol{x}_e^{n,f} = \mathcal{M}^{t^{n-1} \to t^n}(\boldsymbol{x}_e^{n-1}) + \boldsymbol{\epsilon}_e. \tag{4.1}$$

Here, $\mathcal{M}$ represents the numerical SWE model and $\boldsymbol{\epsilon}_e$ is a realisation of the model error as in eq. (3.2). Note that we employ the additive model error as we will actively use its properties later on. Equation (4.1) is called the 'forward step' in the data assimilation cycle and executes for each ensemble member independently. To pronounce that the resulting states are forecasts generated from the physical model, we mark them with the superscript f.

In most geophysical systems, such as in the ocean, states can only be partially observed. In our context, we assume that an *observation* of the (inaccessible) true state $\boldsymbol{x}_{\text{truth}}^n$ is extracted by an operator $\mathcal{H}$ and contains some observation noise. We express the extraction of an observation $\boldsymbol{y}^n \in \mathbb{R}^{N_Y}$ as

$$\boldsymbol{y}^n = \mathcal{H}(\boldsymbol{x}_{\text{truth}}^n) + \boldsymbol{\nu}^n, \tag{4.2}$$

where $\nu^n \sim \mathcal{N}(\boldsymbol{0}, \boldsymbol{R})$ is a Gaussian random variable with independent components. Due to the nature of in-situ observations, we restrict the following considerations to linear observation operators $\boldsymbol{H}$ that are matrices of dimensions $N_Y \times N_X$. In particular, if $\boldsymbol{H}$ has only a single 1 per row and 0 otherwise, then this means that $\boldsymbol{H}$ picks the measured state variables at the measurement location. The noise term accounts for various sources of uncertain errors in the data. The measurement tools have error tolerances themselves, and the observations might not directly represent the actual variables in the computational grid. For example, point measurements of currents using buoys do not directly represent the depth and cell averaged values in the discretised SWE model, but they still contain valuable information. As those inaccuracies are often not elsewhere specified, the Gaussian distribution is chosen as generic error law.

A key assumption in the data assimilation framework of this thesis is the sparsity of data in space. Mathematically speaking, we impose

$$N_Y \ll N_X, \tag{4.3}$$

which expresses the big contrast between the high-dimensional state space and the low-dimensional space of observations.

Model forecasts and available observation data are integrated in *data assimilation* workflows for updating predictions and reducing uncertainty. As this procedure is sequentially repeated whenever new data becomes available, we also speak of *sequential* data assimilation. Bayes' rule provides the formal foundation for data assimilation as

$$p(\boldsymbol{x}^n|\boldsymbol{y}^{1:n}) \propto p(\boldsymbol{y}^n|\boldsymbol{x}^n)p(\boldsymbol{x}^n|\boldsymbol{y}^{1:n-1}), \quad n = 1, \dots, N_T. \tag{4.4}$$

starting from the unconditioned prior PDF $p(\boldsymbol{x}^0)$ at t^0. The forecast $p(\boldsymbol{x}^n|\boldsymbol{y}^{1:n-1})$ that acts as prior is acquired from the forward model before incorporating the latest observation. The likelihood $p(\boldsymbol{y}^n|\boldsymbol{x}^n)$ is the PDF of observing the new data $\boldsymbol{y}^n$ given the model state. For the conditioning, we here use the assumptions of independent error terms in eq. (4.1) and conditionally independent measurements in eq. (4.2). Finally, we are interested in the resulting posterior $p(\boldsymbol{x}^n|\boldsymbol{y}^{1:n})$ or also called filtering PDF that conjuncts the information of prior and likelihood. Together, the prior and the likelihood are the main building blocks for Bayesian inference as Bayes' rule provides the optimal solution of the data assimilation problem, i.e. the posterior, see e.g. [139]. In practice, however, only ensemble approximations of the probability distributions are viable, as we have already acknowledged in Section 3.2. Therefore, Bayes' rule must be interpreted within a Monte Carlo setting.

In contrast to a Monte Carlo setting, ocean forecast systems with a single simulation can only employ variational data assimilation techniques. For this purpose, an optimisation problem is derived from Bayes' rule under the assumption of Gaussian model noise in addition to the Gaussian observation noise. A new state is identified that fits best both the forecast state and the data. In an ensemble version of variational methods, the structures of the covariances in the system are estimated from the samples and go into the optimisation problem, for a review, see [3].

4.2 Ensemble-Based Data Assimilation

In ensemble-based data assimilation, we strive to obtain an ensemble representation of the posterior distribution, and for this task, two major ap-

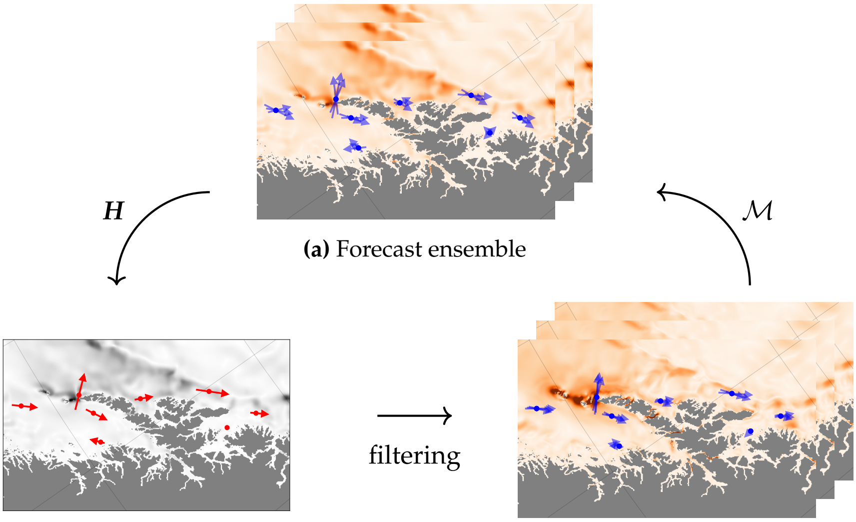

(a) Forecast ensemble

(b) Observations

(c) Analysis Ensemble

Figure 4.1: Conceptual illustration of the data assimilation cycle.

proaches exist, see e.g. [46, 139, 20]. Particle filters (PFs) aim to solve Bayes' rule directly [137], whereas ensemble Kalman filters (EnKFs) are derived from the analytical solution of Gaussian linear problems [44]. In the following, we will give a short description of each of the two approaches.

Both PFs and EnKFs share the same conceptual cycle that is illustrated in Figure 4.1 for ensemble-based data assimilation. Starting from an initial state, ensemble forecasts are evolved until observations become available. Through filtering methods, an updated ensemble is achieved in one way or another. This is also called the analysis step and we will use the superscript a for the resulting states. Finally, a new forecast step can start.

Particle Filters

PFs are data assimilation methods that are designed to approximate the solution of data assimilation problem through a weighted ensemble. The starting point is typically an ensemble of equiprobable states at time t^0, and throughout the data assimilation cycle, the PF updates the weights according to Bayes' rule. In the basic conception of PFs, the states themselves are not manipulated by the assimilation of observation, such that PFs can be considered to be as fully non-linear data assimilation methods and all states remain consistent with the physics in the forward step at all time.

Starting from a weighted ensemble as in eq. (3.5), representing an approximation to the PDF of the initial state denoted by $\hat{p}(\boldsymbol{x}^0)$ or an approximation to the PDF at the previous model time step denoted by $\hat{p}(\boldsymbol{x}^{n-1}|\boldsymbol{y}^{1:n-1})$, with weights $(w_e^{n-1})_{e=1}^{N_e}$, the forecast PDF approximation becomes

$$\hat{p}(\boldsymbol{x}^n|\boldsymbol{y}^{1:n-1}) \propto \sum_{e=1}^{N_e} w_e^{n-1} p(\boldsymbol{x}^n|\boldsymbol{x}_e^{n-1}, \boldsymbol{y}^{1:n-1}). \tag{4.5}$$

To return to a Monte Carlo representation of the forecast, the transition probabilities have to be evaluated in a first step of an algorithm. In the classical bootstrapping approach, this is done by evolving each ensemble member $\boldsymbol{x}_e^{n-1}$ by eq. (4.1) in order to obtain $(\boldsymbol{x}_e^n)_{e=1}^{N_e}$ [59]. In the succeeding update step, the weights are updated according

$$w_e^n \propto p(\boldsymbol{y}^n|\boldsymbol{x}_e^n) w_e^{n-1} \tag{4.6}$$

to approximate the posterior distribution. This assignment updates weights according to the similarity of the observation and the forecast of the ensemble member. Note that only the weights but not the states are manipulated in this purest form of the PF. Hence, we have dropped additional superscripts for the distinction of forecast and analysis states.

The main issue with classical PFs is that over repeated updates, some weights will vanish to almost zero influence, undermining the statistical quality of the ensemble. Hence, resampling approaches are commonly employed, where the goal is to completely disregard low-weight members with negligible statistical contribution, and rather use these computational resources by re-initialising new ensemble members similar to the states of high-weight members [26]. Especially in high-dimensional system like ocean models, it may happen that all states are far away from the observation and a single member carries almost all probability weight. This is called the 'curse of dimensionality' and leads to ensemble degeneration and non-useful results [125]. This is the main reason why PFs are uncommon in ocean data assimilation.

To counteract this behaviour, one could increase the number of ensemble members to postpone the degeneration, but this is rarely computational feasible [75]. Alternatively, one can sample from a proposal density q_e such that the new weights become

$$w_e^{n,*} = \frac{w_e^n}{q_e(\boldsymbol{x}_e^n|\boldsymbol{x}_{1:N_e}^{n-1}, \boldsymbol{y}^n)}. \tag{4.7}$$

The choice for q_e that minimises the variance in the weights is called the optimal proposal and is given by $q_e(\boldsymbol{x}_e^n|\boldsymbol{x}_{1:N_e}^{n-1}, \boldsymbol{y}^n) = p(\boldsymbol{x}^n|\boldsymbol{x}_e^{n-1}, \boldsymbol{y}^n)$, but this is generally hard to evaluate due to the conditioning on the future data [41]. However, in case of a normally distributed model error $\boldsymbol{\epsilon} \sim \mathcal{N}(\mathbf{0}, \boldsymbol{Q})$ the optimal proposal remains Gaussian $\mathcal{N}(\boldsymbol{x}_e^{n,*}, \boldsymbol{P})$ with

$$\begin{aligned}\boldsymbol{x}_e^{n,*} &= \mathcal{M}^{t^{n-1}\to t^n}(\boldsymbol{x}_e^{n-1}) \\ &\quad + \boldsymbol{Q}\boldsymbol{H}^\top \left(\boldsymbol{H}\boldsymbol{Q}\boldsymbol{H}^\top + \boldsymbol{R}\right)^{-1} \left(\boldsymbol{y}^n - \boldsymbol{H}\mathcal{M}^{t^{n-1}\to t^n}(\boldsymbol{x}_e^{n-1})\right) \qquad (4.8\text{a})\end{aligned}$$

$$\boldsymbol{P} = \boldsymbol{Q} - \boldsymbol{Q}\boldsymbol{H}^\top \left(\boldsymbol{H}\boldsymbol{Q}\boldsymbol{H}^\top + \boldsymbol{R}\right)^{-1} \boldsymbol{H}\boldsymbol{Q}, \qquad (4.8\text{b})$$

where we see that the model error covariance $\boldsymbol{Q}$ is actively used to steer the update ensemble [41].

Since proposal density particle filters may still degenerate in high-dimensional models [103], PF variants that retain equivalent weights have gained attention [135]. The implicit-equal weights particle filter (IEWPF, [145]) is one such example, which keeps all weights equal to a target weight and is unbiased in its two-stage formulation [124]. Interestingly, the IEWPF can be implemented efficiently on the GPU and has been applied to simplified ocean models [76].

Ensemble Kalman Filters

In contrast to PFs that seek to solve the non-linear data assimilation problem directly, EnKFs stem from the linearised data assimilation problem with Gaussian assumptions and the ensemble approximation of its analytical solution. The posterior representation is obtained by updating the states vectors while all weight are kept equal and constant by construction [44].

Following the forward step from eq. (4.1), the EnKF estimates the state covariance matrix from the ensemble and we use the short-hand notation $\boldsymbol{\Sigma}_{x,x}^{n,f} = \mathrm{Cov}\left[\boldsymbol{x}^{n,f}, \boldsymbol{x}^{n,f}\right]$. With this, the *Kalman gain* is constructed as

$$\boldsymbol{K} = \boldsymbol{\Sigma}_{x,x}^{n,f}\boldsymbol{H}^\top \left(\boldsymbol{H}\boldsymbol{\Sigma}_{x,x}^{n,f}\boldsymbol{H}^\top + \boldsymbol{R}\right)^{-1}. \qquad (4.9)$$

In accordance with the observation model for the true data in eq. (4.2), the forecasted observations from the ensemble are generated as

$$\boldsymbol{y}_e^n = \boldsymbol{H}\boldsymbol{x}_e^{n,f} + \boldsymbol{\nu}_e^n, \qquad (4.10)$$

where $(\boldsymbol{\nu}_e^n)_{e=1}^{N_e}$ are independent realisations of the model error. Finally, the ensemble is updated and the analysis ensemble is obtained by

$$\boldsymbol{x}_e^{n,a} = \boldsymbol{x}_e^{n,f} + \boldsymbol{K}\left(\boldsymbol{y}^n - \boldsymbol{y}_e^n\right), \qquad (4.11)$$

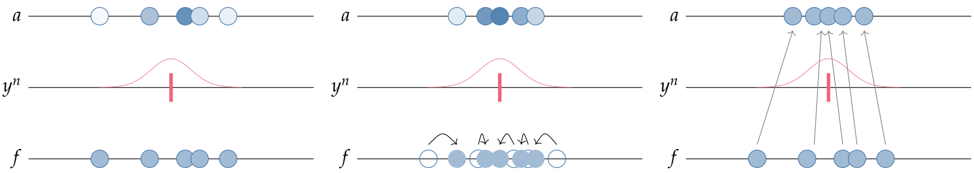

(a) PF **(b)** Optimal Proposal PF **(c)** EnKF

Figure 4.2: Schematic illustration of different ensemble-based data assimilation approaches in one dimension.

see e.g. [19, 77, 47, 136]. Here, the state vectors are manipulated in the update step according to a combination of the Kalman gain, that is the same for all ensemble members, and an individual contribution from the difference between true and forecasted observation. This usually results in a push of the ensemble states towards each other and towards the observation.

First, we note that the EnKF update is similar to the optimal proposal in eq. (4.8a), but the covariance is estimated from the ensemble. Second, for high-dimensional models $\boldsymbol{\Sigma}_{\boldsymbol{x},\boldsymbol{x}}^{n,f}$ is a large matrix of size $N_X \times N_X$, but its assembling is actually not required. Instead, we can more efficiently use

$$\boldsymbol{\Sigma}_{\boldsymbol{x},\boldsymbol{y}}^{n,f} = \boldsymbol{\Sigma}_{\boldsymbol{x},\boldsymbol{x}}^{n,f} \boldsymbol{H}^{\top} = \mathrm{Cov}\left[\boldsymbol{x}^{n,f}, \boldsymbol{H}\boldsymbol{x}^{n,f}\right], \tag{4.12}$$

which is a matrix in dimensions $N_X \times N_Y$ only. This simplifies the Kalman gain as

$$\boldsymbol{K} = \boldsymbol{\Sigma}_{\boldsymbol{x},\boldsymbol{y}}^{n,f} (\boldsymbol{H}\boldsymbol{\Sigma}_{\boldsymbol{x},\boldsymbol{y}}^{n,f} + \boldsymbol{R})^{-1}. \tag{4.13}$$

Even though eq. (4.13) enables more efficient computations [45], further developments as deterministic square-root filter are common, see e.g. [141, 139]. These methods exploit the assumption of a Gaussian posterior and avoid sampling errors due to perturbed model observations. The analysis distribution is defined as $\mathcal{N}(\overline{\boldsymbol{x}}^{n,a}, \boldsymbol{\Sigma}^{n,a})$, which is again derived from the linear Gaussian case. Then, the analysis samples are obtained by

$$\boldsymbol{x}_e^{n,a} = \overline{\boldsymbol{x}}^{n,a} + \tilde{\boldsymbol{x}}_e^{n,a} \tag{4.14}$$

where $\tilde{\boldsymbol{x}}_e^{n,a}$ comes from a matrix square root of $\boldsymbol{\Sigma}^{n,a}$. One such example is the ensemble transform Kalman filter (ETKF, [10]) which works in the ensemble subspace.

A schematic illustration for PFs and EnKF in a single dimension is provided in Figure 4.2. All data assimilation in this subsection methods include in one way or another a forward step yielding a prior ensemble. This is the equally-weighted dots lying on the lower line depicting the prior states. The displays illustrate how ensembles are re-weighted or moved in the assimilation step. The standard PF only updates the weights, represented by colour shades, while the optimal proposal PF also generates updated states before weighting. In only one dimension, the EnKF update becomes a weighted sum of the prior states and the observation rated by the relation $\frac{1}{1+\sigma/r}$ between the prior variance σ and the observation noise r. The states are moved closer to the observation similar to the update in the optimal proposal PF, but in the EnKF all weights are kept equal.

Localisation

A single observation is mostly valid for describing the conditions in its vicinity, but the limited ensemble size can lead to unintended effects that thwart the filtering update. Therefore, localisation is an essential strategy in practical high-dimensional data assimilation applications.

In the classical PF, we work with weights that are global parameters. So, it may happen that one ensemble member fits well to an observation in one area, but not to an observation in another area. Then, it is difficult to merge different members in such a way that they are a good fit to both observations. One approach lies in sequential processing of observations and smooth reconstruction of posterior ensemble members [110]. In the case of proposal density particle filters, we note that not only weights are changed but also the analysis members are sampled from a new distribution. In particular, this proposal distribution is redefined for each member and incorporates the latest observation data. Thereby, the new ensemble can be steered locally towards each observation.

For EnKFs, there are two common localisation schemes: *local analysis* and *covariance localisation* where in practice the decision for one or the other depends on reasons like computational efficiency [118]. Local analysis follows the paradigm that only data in a certain neighbourhood should influence the update of a grid cell [18]. For each single grid cell or group of grid cells, a subset of close observations is selected and then the update is performed in the local state dimensions only, for example using ETKF [108]. For scenarios with $N_Y \approx N_X$ this scheme is very powerful and can be efficiently parallelised or combined with tapering in the observation influence [80].

Note that the low-rank Monte Carlo estimation of the covariance matrix suffers from spurious correlations that would generate inadvertent long-range updates. In contrast to local analysis, the point of view is reverted

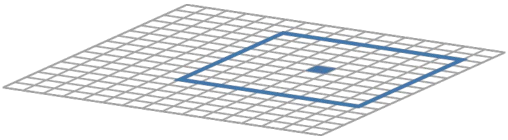

Figure 4.3: Schematic illustration of the interpretation of covariance localisation showing an observation (blue grid cell) together with its area of influence (blue frame). The mesh represents a computational grid for a FVM.

in covariance localisation and the idea is that an observation only affects grid cells that are physically nearby to the observation location, see Figure 4.3. This is done by multiplying the covariance matrix elementwise with a tapering function [78, 79]. As the covariance matrix is often not assembled, this approach can be transferred to the observation space or the Kalman gain [22]. Both localisation approaches can be formulated in such ways that the Kalman gain is not formed in the full state dimensions yielding improved computational efficiency in addition to the truncation of spurious correlations. Herein, we will use Kalman-gain localisation for $N_Y \ll N_X$.

4.3 Assessment of Ensemble Forecasts

Apart from the generation of ensemble forecasts and their refinement by data assimilation, the assessment of the forecast quality is crucial [128, 55]. Therefore, the role of new observational data is extended beyond its use in the assimilation to also serve as reference to assess of the predictive skills. This process where the ensemble forecast is assessed in relation to observations can also be called evaluation or verification [143, Chapter 7] and such considerations enable to evaluate the propriety of the included dynamical models and filtering methods.

Here, we start the discussion for a scalar observation y, meaning that $N_Y = 1$ in eq. (4.2), and we again omit superscripts indicating the time step. An ensemble forecast for the same time, usually after assimilating previously available data, generates synthetic observations y_e as in eq. (4.10). In the Bayesian framework, the observation is associated with some uncertainty and hence it is not favourable when all ensemble members match the observation, but the ensemble should provide a good fit and represent the uncertainty appropriately.

Error metrics like the bias [37] or the root-mean square error [77] are versatile applicable and give good indication of the forecast quality for single experiments. However, the ultimate ambition is that the synthetic ensemble observations have the same statistical distribution as the real observations [57].

To this end, we recall some statistical foundations for scalar observations and introduce the cumulative distribution function (CDF, F) of a real-valued random variable as

$$F(y) = \int_{-\infty}^{y} p(y^*)\,\mathrm{d}y^* \tag{4.15}$$

where p is the PDF. Then, the CDF takes values from 0 to 1 and is monotonously increasing. A fundamental result states, if a random variable Y is distributed according to F, then

$$F(Y) \sim \mathcal{U}[0,1], \tag{4.16}$$

meaning samples of $F(Y)$ are uniformly distributed.

Probability-integral transforms (PIT) are intended to exploit the relation in eq. (4.16) for the assessment of an ensemble forecast. In the Monte Carlo case, the CDF is approximated by the empirical cumulative distribution function (ECDF, $\hat{F}$) which is calculated by eq. (4.15) where the EPDF $\hat{p}$ substitutes the PDF p. The PIT value u is then defined as

$$u = \hat{F}(y), \tag{4.17}$$

meaning that it is the function value of the ECDF for the observation y. Now, one assumes that the observations y follow an unknown statistical distribution Y and if the ensemble represents the same distribution, then the PIT values will be approximative samples from a uniform distribution. For an ensemble with equal weights, the PIT value boils down to counting the rank of the true observation in the sorted ensemble values and normalising by the ensemble size. Therefore, the PIT value is also called 'rank'.

To evaluate whether the observations and the ensemble forecasts have the same distribution, the calculation of PIT values is repeated multiple times for a set of independent observations and ensemble forecasts. This can be done from historical time series or from repetitions of the full experiment. Then, the results are visualised by a histogram and this is a popular analysis tool [69]. Due to the result in eq. (4.16), the true distribution will result in flat histograms that are indistinguishable from a uniformly distributed random variable subject to some Monte Carlo noise [43]. Therefore, flat histograms are favourable. Convex shapes indicate an overdispersive ensemble, while a concave shape is an indicator for underdispersion

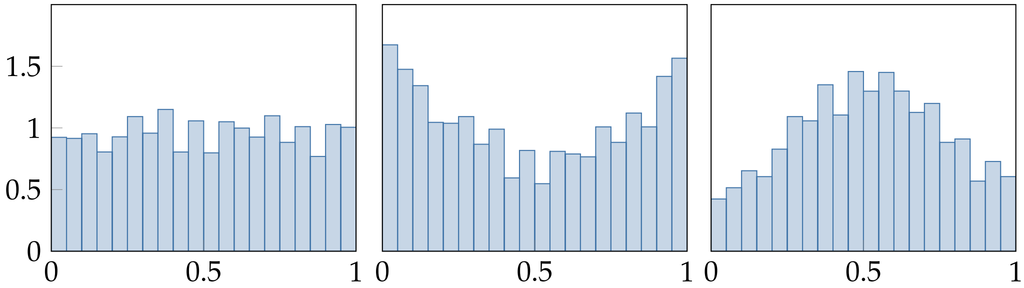

(a) Calibrated ensemble

(b) Underdispersive ensemble

(c) Overdispersive ensemble

Figure 4.4: Exemplary PIT histograms

and one-sided histograms hint a bias [142, 117]. For an illustrative example, see Figure 4.4.

Beyond histograms, scoring rules reward the conformity of the forecast with the distribution of the observation and can be used to assess the statistical fit of an ensemble [56]. For example, the continuous ranked probability score (CRPS) as proper scoring rule is defined as

$$\mathrm{CRPS}(F, y) = \int_{-\infty}^{\infty} \left(F(y^*) - \mathbb{1}_{[y,\infty)}(y^*)\right)^2 \, \mathrm{d}y^*, \tag{4.18}$$

where $\mathbb{1}_{[}y, \infty)$ is the indicator function for the set $[y, \infty)$. For the ensemble evaluation, the CDF F can be replaced by the ECDF $\hat{F}$ and the experiment can repeated similarly to the acquisition of PIT values obtaining an average CRPS. If the ensemble and the observation come from the same distribution, then the average CRPS is minimal.

In context of the SWE model, an in-situ observation of the current at a single location in the domain is actually two-dimensional, since currents in both coordinate directions are measured. To use the PIT histograms or CRPS directly, one has to be treated the dimensions individually such that histograms or CRPS are often presented for each variable independently. For the assessment of the joint two-dimensional vector of the current components, there are efforts to elevate the same assessment concepts. Ranks are re-defined to still produce one-dimensional histograms [131] and the CRPS is generalised to the energy score [58].

Chapter 5

Multi-Level Data Assimilation

In the previous chapters, we have laid the foundation for a complementary ocean forecasting system by introducing simplified ocean models and data assimilation techniques as necessary components. In this chapter, we continue the quest for computational efficiency and aim to save computational costs in the production of forecasts. Therefore, we investigate the computational benefits of using simulations on multiple resolutions and an alternative method to construct the Kalman gain in the data assimilation routine.

To set the stage, it is helpful to revisit a few properties of the simplified ocean model from Chapter 2: The SWE model offers flexibility in the spatial resolution, where it can also run simulations on a coarser or finer resolution than the operational data. The effect of varying resolution can be inspected, for example, by the vorticity ω_z, which is a measure for the rotation of the water. The rate relative to the earth rotation is defined by

$$\omega_z = \frac{\partial v}{\partial x} - \frac{\partial u}{\partial y}, \tag{5.1}$$

where the notation must not be mixed with the notation for a stochastic realisation. Vorticity can be used to visualise eddies and the level of details in a flow field, and Figure 5.1 shows the vorticity field of simulations with different resolutions in the Lofoten area. All simulations are initialised from the same state extracted from NorKyst and evolved for 3 h. NorKyst runs on the fixed resolution of 800 m, but the SWE in the local area can be run on flexible resolutions [15]. For the SWE simulations, we consider a coarse cell size of 1.600 m, the matching resolution of 800 m, and refined cells with edge length 200 m. In the results on coarse grids, the general patterns of the vorticity are reflected but details are lost. In contrast, the simplified simu-

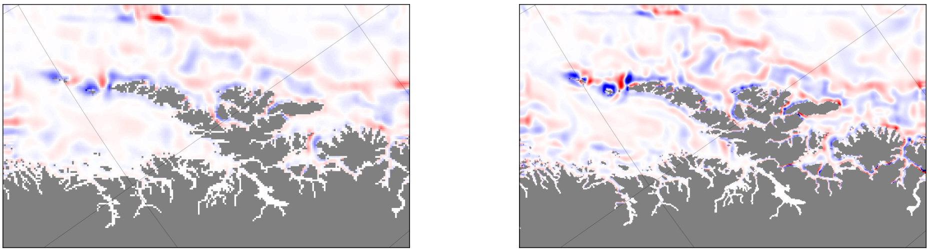

(a) SWE with $\Delta = 1.600\,\mathrm{m}$

(b) SWE with $\Delta = 800\,\mathrm{m}$

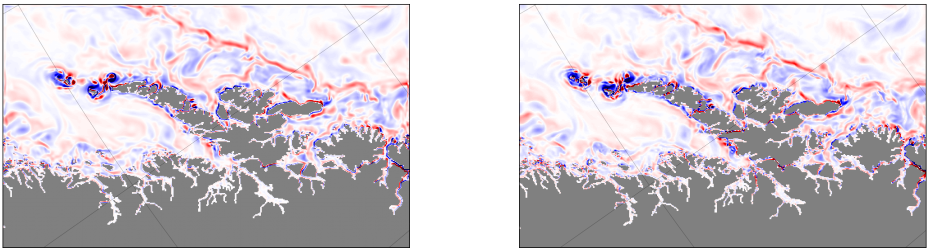

(c) SWE with $\Delta = 200\,\mathrm{m}$

(d) NorKyst with $\Delta = 800\,\mathrm{m}$

Figure 5.1: Vorticity after 3 h of simulation with the SWE on different resolutions and with NorKyst on the operational resolution.

lation with the SWE on the finest resolution is very similar to the NorKyst result and keeps the same amount of details as the complex model. The simplified description of the dynamics can be compensated by increased resolution. For this reason, the fine SWE model also stays valid for longer time as the coarse set-ups. Therefore, the ambition is to provide forecasts and conduct data assimilation on the grid with $\Delta = 200\,\mathrm{m}$.

In tandem with the level of detail, the computational run time of the SWE increases towards finer resolutions, whereas coarse grids enable faster simulations but might miss fine-scale details. Nonetheless, those coarse simulations can still resolve large-scale dynamics and can contribute this information inexpensively to statistical estimators. Then, the cost for generation of forecasts can benefit from ensembles of many cheap models on coarse grids for the larger patterns, while more expensive ensembles on fine resolutions fill in features stemming from small-scale dynamics. The flexible resolution of the SWE facilitates to use information from multiple resolutions at different computational cost per resolution.

In this chapter, we introduce multi-level methods in the data assimilation context. The idea of multi-level methods originates from numerical integration, where ensembles of different accuracy are combined by a telescoping sum [70]. Thereby, computational costs can be saved as fewer expensive samples of high accuracy have to be simulated.

This notion extends to statistical estimation such that under certain assumptions a speed-up for the estimation is achieved by preserved statistical quality [52]. In the context of numerical solutions to PDEs, decreasing grid resolutions yield decreasing accuracy by decreasing computational costs. So, the multi-level approach got applied in PDE applications [28, 40] and its potential to reduce computational costs got particularly analysed for hyperbolic conservation laws [100, 96] and the SWE [101]. For data assimilation problems, however, the multi-level concept is less established yet, but it got recently explored for particle filters [82, 61, 90] and ensemble Kalman filters [71, 24].

5.1 Multi-Level Monte Carlo Estimators

Up to this chapter, all members of an ensemble have shared the same computational grid. However, in this chapter, we introduce a hierarchy of grids that cover the same domain, and we use these grids to generate numerical SWE solutions of different accuracy. In abuse of notation, both the grid itself and the grid cell size of the original grid are simply referred to as Δ. We define the hierarchy such that the finest resolution corresponds to the original grid, meaning that we set $\Delta^L = \Delta$. Then, the hierarchy considers additionally a set of grids that are coarser than the original one. The grids in the hierarchy are denoted as Δ^l for $l = 0, \dots, L$ with $\Delta^0 > \cdots > \Delta^L$, such that Δ^0 is the coarsest and Δ^L is the finest grid. Note here that the original grid refers to the resolution of interest and should not be mixed with the resolution of the operational grid.

For most of the following considerations, we restrict ourselves to a hierarchy of nested grids, where the domain of a fine cell is covered by exactly one coarser grid cell only. Nested grids can, for example, be generated by iteratively merging neighbouring cells starting from the original grid: two cells in x-direction and two cells in y-direction such that four cells are merged into a coarser one [6]. Such a hierarchy is illustrated in Figure 5.2.

The resolutions in a hierarchy of grids are referred to as *levels*. To distinguish states on different levels, we use the superscript l for the reference to a certain grid level l, and denote states as $\boldsymbol{x}^l \in \mathbb{R}^{N_X^l}$. Hereby, the states on different levels have distinct dimensions N_X^l according to the varying number of grids cells on each level. Note that we still omit the usage of the time step superscript to prevent confusion.

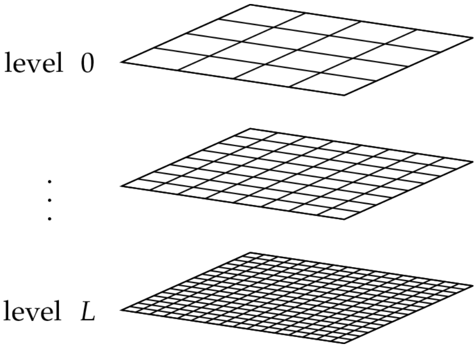

Figure 5.2: Illustration of hierarchy of grids. Original grid with index L on the bottom and lower levels with coarser resolutions above.

In the aforementioned hierarchy of nested grids, the edges size of a grid cell is increased by a factor of two between each level. Then, solving the SWE with FVM on these different levels is associated with varying computational costs and we investigate this here in exemplary manner. Starting from a given level, the number of grid cells on the next coarser grid is reduced by a factor of four. Consequently, the theoretical computational workload to solve the SWE is also diminished by the same factor. This reduction is further amplified by the ability to double the time step size according to the CFL condition in eq. (2.6) which leads to a halving of the number of Runge-Kutta steps. In total, the theoretical cost is significantly reduced by a factor of eight. The computational effort required for the numerical solution of the SWE follows a scaling of $\mathcal{O}(\Delta^{-3})$ in a more general notion [100].

States on all levels essentially describe the same physical quantities in the same domain but on different grids. Then, performing calculations between the vectors of different dimensions necessitates transformations that map a state $\boldsymbol{x}^l$ from level l onto the other levels [48]. For the mathematical description, we denote the projection of a state on level l to a corresponding state on level k as $\boldsymbol{P}_{l\to k} : \mathbb{R}^{N_X^l} \to \mathbb{R}^{N_X^k}$. For a hierarchy of nested grids as before, the projection between two consecutive grids $\boldsymbol{P}_{l\to l-1}$ is a matrix of dimensions $N_X^{l-1} \times N_X^l$ with four $1/4$ per row such that neighbouring values are averaged. Vice versa $\boldsymbol{P}_{l\to l+1}$ is a matrix of dimensions $N_X^{l+1} \times N_X^l$ with four 1 per row such that the same value is repeated on the corresponding finer grid cells. Further projections are generated by repeating these operators. This choice is easy and efficient to implement without explicit construction of these matrices and it preserves global volumes. With these projections, it is possible to execute statistical estimations on any level. Hereby, the following identities hold

$$\mathrm{E}\left[\boldsymbol{P}_{l\to k}\boldsymbol{x}^l\right] = \boldsymbol{P}_{l\to k}\mathrm{E}\left[\boldsymbol{x}^l\right], \tag{5.2a}$$

$$\mathrm{Cov}\left[\boldsymbol{P}_{l\to k}\boldsymbol{x}^l, \boldsymbol{P}_{l\to k}\boldsymbol{x}^l\right] = \boldsymbol{P}_{l\to k}\mathrm{Cov}\left[\boldsymbol{x}^l, \boldsymbol{x}^l\right]\boldsymbol{P}_{l\to k}^\top. \tag{5.2b}$$

where the transposed projection acts column-wise. This means that there is a direct transformation of states and operations between different levels, such that we omit the explicit notation of projections in the remainder.

Next, we consider two SWE models on two consecutive levels that are initialised with the same data. Note that this includes a projection, but we do not symbolise that. Then, these models will still evolve differently due to numerical errors in the FVM scheme, where we usually trust the simulation on the fine grid more than on the coarse grid. Additionally to sharing the same initial conditions, both instances on the different grids can be perturbed with the same realisation of the model error during the simulation window. This leads to a stochastical coupling between both simulations. Such a pair of simulations is then denoted $(\boldsymbol{x}^{l+}, \boldsymbol{x}^{l-})$, where $\boldsymbol{x}^{l+}$ is defined on the grid Δ^l and $\boldsymbol{x}^{l-}$ on Δ^{l-1}. On the finest level, we however elude this notation and set $\boldsymbol{x}^{L+} = \boldsymbol{x}$ as Δ^L is the original grid.

Having defined states and pairs of states on a hierarchy of grids, we return to statistical estimation. We then exploit a telescoping sum, such that the expected value on the finest level L can be written as

$$\mathbb{E}\left[\boldsymbol{x}\right] = \sum_{l=1}^{L}\left(\mathbb{E}\left[\boldsymbol{x}^l - \boldsymbol{x}^{l-1}\right]\right) + \mathbb{E}\left[\boldsymbol{x}^0\right], \tag{5.3}$$

where the linearity of the expected value was used so that the expected values for all levels $l < L$ cancel out. Note that we do not explicitly denote projections in (5.3), as we have justified after (5.2). Here, the telescoping sum acts as a link between the estimation on the finest level and the incorporation of the coarser levels. The analogous formula holds for integrated quantities of interest and motivates the further construction of multi-level estimation methods.

In Section 3.2, the expected value was approximated by the Monte Carlo technique and the use of ensembles. Since all ensemble members in the corresponding estimation in eq. (3.6) are defined on the same grid, we also refer to that classical estimator as a 'single-level estimator'. Moreover, we also use this nomenclature when states first have to be projected onto a common grid, but the same formula is used. Similarly, we continue to approximate the expected values in eq. (5.3). Each of the expected values therein can be estimated by the single-level estimator, but the samples for the estimation of the expected values $\mathbb{E}[\boldsymbol{x}^l - \boldsymbol{x}^{l-1}]$ are coupled in the sense that the simulations share the same stochastic realisation on both levels. Hence, a *multi-level ensemble* consists of

- a set of states on the coarsest level $(\boldsymbol{x}_e^0)_{e=1}^{N_e^0}$ and
- pairs of states $(\boldsymbol{x}_e^{l+}, \boldsymbol{x}_e^{l-})_{e=1}^{N_e^l}$ on all further levels $l = 1, \dots, L$,

where N_e^l are the ensemble sizes per level. The corresponding *multi-level estimator* for $\mathbb{E}\left[\boldsymbol{x}\right]$ is as an unbiased approximation defined as

$$\mathrm{E}^{\mathrm{ML}}\left[\boldsymbol{x}\right] = \mathrm{E}\left[\boldsymbol{x}^0\right] + \sum_{l=1}^{L} \left(\mathrm{E}\left[\boldsymbol{x}^{l+}\right] - \mathrm{E}\left[\boldsymbol{x}^{l-}\right] \right), \tag{5.4}$$

where the single-level estimators are used on the right-hand side. While the single-level Monte Carlo technique originates from an empirical measure as in eq. (3.5), this property is lost for the multi-level Monte Carlo setting. In particular, a Dirac representation associated with the multi-level Monte Carlo approach is in general not a measure, because it can take negative values. Moreover, it is not necessarily bounded by 1, but its approximations of $\mathbb{E}\left[\boldsymbol{x}\right]$ have been proven to converge to the correct limit [53].

Beyond the approximation of the expected value, the multi-level formalism is versatile for handling arbitrary quantities of interest. Most importantly for data assimilation, the multi-level approximation of the covariance [8, 105] can be expressed as

$$\mathrm{Cov}^{\mathrm{ML}}\left[\boldsymbol{x}, \boldsymbol{x}\right] = \mathrm{Cov}\left[\boldsymbol{x}^0, \boldsymbol{x}^0\right] + \sum_{l=1}^{L} \left(\mathrm{Cov}\left[\boldsymbol{x}^{l+}, \boldsymbol{x}^{l+}\right] - \mathrm{Cov}\left[\boldsymbol{x}^{l-}, \boldsymbol{x}^{l-}\right] \right), \tag{5.5}$$

where again the single-level estimators from eq. (3.7) are recycled. Unlike in the classical single-level estimation, there is no guarantee that $\mathrm{Cov}^{\mathrm{ML}}\left[\boldsymbol{x}, \boldsymbol{x}\right]$ is a positive semi-definite matrix.

5.2 Practicalities for Multi-Level Ensembles

Having the formalism for estimators based on multi-level ensembles at hand, we shift our attention more towards the practical implementation. We return to the intention of achieving computational benefits by this procedure, where we aim to retain the statistical quality of the estimator and simultaneously reduce computational costs. Therefore, we start with analysing the computational costs and the associated statistical error, which consequently enables us to choose appropriate ensemble sizes on each level.

To conduct the subsequent discussion slightly more general, we introduce the quantity of interest $\mathbb{E}\left[g(\boldsymbol{x})\right]$ with $g : \mathbb{R}^{N_X} \to \mathbb{R}^{N_g}$ for some N_g. The expected value from eq. (5.4) is then recovered with g equal to the identity mapping. While this notation makes the examination applicable to a larger range of quantities of interest, it also exhibits that the results in the following are intrinsically dependent on g.

Computational Costs

Computational costs manifest in the wall time that it takes to evolve a SWE simulation forward in time on available hardware. We usually simulate until a certain time where we want to conduct an estimation such that this corresponds, in other words, to the generation of the samples for the estimation. The multi-level approach gains advantage from coarse grids, where the SWE are computationally less expensive to solve than on the original grid. We keep all other factors like schemes for FVM fluxes and time integration fixed, such that the computational cost is solely determined by the grid resolution. The computational cost associated with solving the SWE on level 0 are denoted as C^0 and the costs for a pair $(\boldsymbol{x}^{l+}, \boldsymbol{x}^{l-})$ are represented as C^l, where C^l for $l > 0$ actually entails the numerical solution on two grids.

As motivated already in the previous section, the costs scale in theory as $\mathcal{O}(\Delta^{-3})$ over the grids. In practice, the scaling of the computational costs can however be influenced by technical factors. In ocean models, parallelisation is a common strategy to accelerate the run times of simulations. Both parallelisation and multi-level methods are primarily independent efforts for reduced run times, but they follow different pathways and can interfere in certain regards. Here, parallelisation leads typically to reduced computational costs at full scale of the problem, but for very small grid sizes that do not utilise the entire parallelism of the implementation the theoretical scaling may no longer hold true.

Statistical Error

After evolving simulations up to certain time, we consider the accuracy of the statistical estimation itself. The statistical error in the estimation τ_g is defined as the variance of the estimator for $\mathbb{E}\left[g(\boldsymbol{x})\right]$ and is given for a single-level ensemble by

$$\tau_g^2 = \frac{\|\mathbb{V}\mathrm{ar}\left[g(\boldsymbol{x})\right]\|}{N_e}, \tag{5.6}$$

where $\|\cdot\|$ is a norm over $\mathbb{R}^{N_g}$. Both the ensemble size and also the quantity of interest g itself influence the statistical quality. While $\mathbb{V}\mathrm{ar}\left[g(\boldsymbol{x})\right]$ is unknown in practice and has to been estimated itself, the variance term is determined by the inherent distribution of the states and the the function g. Notwithstanding, an increase in ensemble size can reduce the statistical error. In the classical single-level context, the choice of the ensemble size is typically dictated by the available computational resources and it is simply accepted that, e.g. mean and covariance are estimated with different statistical errors.

For a multi-level ensemble, the statistical error for the estimation is analogously described by

$$(\tau_g^{\mathrm{ML}})^2 = \frac{\|\mathbb{V}\mathrm{ar}\left[g(\boldsymbol{x}^0)\right]\|}{N_e^0} + \sum_{l=1}^{L} \frac{\|\mathbb{V}\mathrm{ar}\left[g(\boldsymbol{x}^l) - g(\boldsymbol{x}^{l-1})\right]\|}{N_e^l}, \tag{5.7}$$

where the exact variances are again inaccessible in practise. Moreover, to achieve a small statistical error for the multi-level estimator, the identity

$$\begin{aligned} &\mathbb{C}\mathrm{ov}\left[g(\boldsymbol{x}^l) - g(\boldsymbol{x}^{l-1}), g(\boldsymbol{x}^l) - g(\boldsymbol{x}^{l-1})\right] \\ &\qquad = \mathbb{C}\mathrm{ov}\left[g(\boldsymbol{x}^l), g(\boldsymbol{x}^l)\right] + \mathbb{C}\mathrm{ov}\left[g(\boldsymbol{x}^{l-1}), g(\boldsymbol{x}^{l-1})\right] \\ &\qquad\qquad - 2\mathbb{C}\mathrm{ov}\left[g(\boldsymbol{x}^l), g(\boldsymbol{x}^{l-1})\right] \end{aligned} \tag{5.8}$$

suggests that the levels should be strongly correlated. This correlation is a key indicator of scenarios where the multi-level approach can actually aid computational efficiency. Subsequently, we use the notations $V^0 = \|\mathbb{V}\mathrm{ar}\left[g(\boldsymbol{x}^0)\right]\|$ and $V^l = \|\mathbb{V}\mathrm{ar}\left[g(\boldsymbol{x}^l) - g(\boldsymbol{x}^{l-1})\right]\|$ for $l > 0$.

Multi-Level Ensemble Size

A key design choice for the implementation of multi-level ensembles is the assignment of the ensemble sizes N_e^l on each level. These ensemble sizes are determined by solving an optimisation problem that minimises the computational costs under the constraint of fixed statistical error for the estimation of the quantity of interest [104]. Based on this, we obtain

$$N_e^l = \left\lceil \sqrt{\frac{V^l}{C^l}} C_\tau \right\rceil \qquad \text{with } C_\tau = \frac{1}{\tau_g^2} \sum_{l=0}^{L} \sqrt{V^l C^l}, \tag{5.9}$$

where τ_g is in our case given by the statistical error of a reference single-level ensemble. In relevant conditions, the ensemble sizes will typically increase towards the coarser levels [53].

Beyond the definition herein, it is possible to construct best linear unbiased multi-level estimators where the state pairs extend to more than two levels, both for the scalar case [121] and for the multi-variate case [38]. The multi-level estimation is then reformulated as a linear regression problem and weights are introduced for the coupled simulations. The weights are chosen to minimise the variance of the multi-level estimator further. While it is conceptually possible to integrate this into the preceding definitions, the coupling of more than two levels introduces further computational overhead in the forward step due to the exchange of the perturbation realisations between the different simulation instances such that we restrict our considerations to the case with two coupled levels.

Computational Speed-Up

To evaluate the computational effect of the multi-level approach, we need to examine the total computational costs of the different types of ensemble simulations. In the case of a single-level ensemble, the total costs are obtained from the product of ensemble members N_e and the computational costs c^L for a single simulation on the original level. This amounts to $\mathcal{C} = N_e \cdot c^L$. In the context of multi-level estimation, the costs are aggregated over the levels and summarised as

$$\mathcal{C}^{\mathrm{ML}} = \sum_{l=0}^{L} N_e^l \cdot C^l. \tag{5.10}$$

For ensembles that yield the same statistical error the computational impact is quantified as the speed-up

$$\mathcal{S} = \frac{\mathcal{C}}{\mathcal{C}^{\mathrm{ML}}}. \tag{5.11}$$

An acceleration is indicated if $\mathcal{S} > 1$ and the speed-up provides a measure of how much faster the multi-level ensemble is compared to the single-level ensemble or vice versa how much slower the single-level ensemble is compared to the multi-level ensemble.

Albeit, the multi-level approach harvests the computational efficiency of coarse grids, it will not always yield a speed-up. The potential of multi-level estimation depends crucially on the coupling between the levels. Strong coupling on fine levels in relation to the general variance in the system and steep computational scaling are favourable for a speed-up. If the system we want to simulate is too turbulent on the small scale, meaning that the correlation between levels is weak, we cannot expect any benefits from using coarser levels. The opposite situation can also be imagined, where the correlations between levels are so strong such that there are effectively no extra details to be found on the finest level compared to a coarser level. In that case, the theoretical speed-up is large but the finest simulations do not add any value to the results, such that in practice it would be better to neglect fine levels or to use simply a single-level ensemble on a coarser resolution.

Application to Simplified Ocean Models

As seen in Figure 5.1, the SWE model necessitates increased spatial resolutions for high-quality forecasts. While the computational costs for simulating the SWE grow in accordance with the resolution, the model can be easily run on different resolutions in a hierarchy of nested grids. Moreover, the interpretation of the vorticity suggests that the levels are, to a visual extent, correlated, such that the simplified ocean model appears to be suited for the application of multi-level methods. In this case, for instance, we would be interested in constructing a multi-level SWE ensemble with $\Delta = 200\,\mathrm{m}$ as resolution of interest.

Multi-level estimators enable to gather statistical information from a multi-level SWE ensemble on the original grid. For example, mean velocity and variance can be calculated at certain times. These estimates therefore facilitate a seamless incorporation of a multi-level ensemble for drift prediction according to the trajectory modelling by ensemble statistics in Section 3.2, where the conventional estimators for mean and variance are replaced by their multi-level analogons in eq. (3.11). This promotes the usability of multi-level ensembles for the generation of drift trajectory forecasts for SAR scenarios.

5.3 Multi-Level Ensemble Kalman Filter

Transitioning from multi-level Monte Carlo methods without conditioning on observation data towards multi-level data assimilation (MLDA), we build upon the EnKF method outlined in Section 4.2. The multi-level ensemble Kalman filter (MLEnKF) applies multi-level estimation to the Kalman gain [71] and has been extended by a version for spatio-temporal data assimilation problems [24]. This approach has also been combined

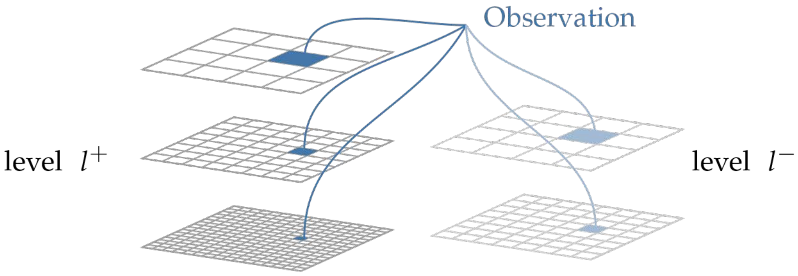

Figure 5.3: Illustration of the observation operations in a multi-level ensemble

with Bayesian model averaging (see e.g. [112]) and applied for reservoir simulations [50, 106].

In the MLDA context, a multi-level ensemble of SWEs is evolved in time until data becomes available. The observation model in eq. (4.2) means then that the data is associated with the finest level. This implies that coarser states have to be upscaled to the finest level before the observation operator is applied. For point observations in the SWE model, this is still equivalent to picking the current values from the grid cell that contains the observation location, see Figure 5.3. Therefore, we introduce the shorthand notation $\boldsymbol{H}^l$ for extracting data from level l.

For the assimilation of observation data into the multi-level ensemble, we adapt the method of Chernov et al. [24] and apply multi-level estimation for the Kalman gain, but phrase it for nested grids as introduced above. In the construction of the Kalman gain, the estimate of the state-observation covariances in eq. (4.12) is replaced with an estimate as in eq. (5.5). At the n-th time step of the sequential data assimilation cycle, we obtain

$$\begin{aligned}\boldsymbol{\Sigma}_{\boldsymbol{x},\boldsymbol{y}}^{n,f,\mathrm{ML}} &= \mathrm{Cov}\left[\boldsymbol{x}^{0,n,f}, \boldsymbol{H}^0\boldsymbol{x}^{0,n,f}\right] \\ &+ \sum_{l=1}^{L}\left(\mathrm{Cov}\left[\boldsymbol{x}^{l+,n,f}, \boldsymbol{H}^l\boldsymbol{x}^{l+,n,f}\right] - \mathrm{Cov}\left[\boldsymbol{x}^{l-,n,f}, \boldsymbol{H}^{l-1}\boldsymbol{x}^{l-,n,f}\right]\right). \end{aligned} \tag{5.12}$$

This multi-level covariance estimate is plugged in to eq. (4.13) and the resulting Kalman gain, denoted by $\boldsymbol{K}^{\mathrm{ML}}$, has the same dimensions as a single-level Kalman on the finest level.

In the update step, all levels are conditioned using $\boldsymbol{K}^{\mathrm{ML}}$. To do so, the spatial dimension of the Kalman gain is downscaled onto the respective level and the analysis multi-level ensemble is given on the coarsest level by

$$\boldsymbol{x}_e^{0,n,a} = \boldsymbol{x}_e^{0,n,f} + \boldsymbol{K}^{\mathrm{ML}} \left(\boldsymbol{y}^n - \boldsymbol{H}^0 \boldsymbol{x}_e^{0,n,f} - \boldsymbol{\nu}_e^{0,n} \right) \tag{5.13a}$$

and on the higher levels by

$$\boldsymbol{x}_e^{l+,n,a} = \boldsymbol{x}_e^{l+,n,f} + \boldsymbol{K}^{\mathrm{ML}} \left(\boldsymbol{y}^n - \boldsymbol{H}^l \boldsymbol{x}_e^{l+,n,f} - \boldsymbol{\nu}_e^{l,n} \right) \tag{5.13b}$$

$$\boldsymbol{x}_e^{l-,n,a} = \boldsymbol{x}_e^{l-,n,f} + \boldsymbol{K}^{\mathrm{ML}} \left(\boldsymbol{y}^n - \boldsymbol{H}^{l-1} \boldsymbol{x}_e^{l-,n,f} - \boldsymbol{\nu}_e^{l,n} \right), \tag{5.13c}$$

where pairs share the same observation noise $\boldsymbol{\nu}_e^{l,n}$, recall eq. (4.10).

The MLEnKF framework enables to combine multi-level ensembles in the forward model and EnKF-based data assimilation. Hereby, a computational speed-up for MLDA can originate from exploiting cost efficient coarser levels in the forward step. While the updating with MLEnKF shares the basic concept with the corresponding single-level data assimilation workflow, the forecast and analysis ensemble are represented on multiple levels. On the one hand, MLEnKF inherits the computational benefits of multi-level Monte Carlo methods in the forward step, but on the other hand it also takes over the shortcomings. In particular, the multi-level ensemble size in a MLDA workflow is fixed, where the optimal configuration is usually chosen for the single estimation of a certain quantity of interest, but the ensemble is used for repeated estimations of multiple quantities of interest. Also negative eigenvalues in the covariance estimation gain new significance since these covariances are used in the update process and thereby corrupted estimations during one update step could be transported into the further evolution of the ensemble.

5.4 Assessment of Multi-Level Ensemble Forecasts

Analogously to the Section 4.3, there arises the need to assess multi-level ensemble forecasts originating from a MLDA workflow with respect to observations. For error metrics like the bias and the root-mean square error, the multi-level estimation framework as in eq. (5.4) can be employed with a relevant quantity of interest. Beyond those, we emphasise the evaluation whether forecast and observation distributions are in accordance. As for single-level ensembles, the assessment of the calibration of multi-level ensemble forecasts with the traditional means relies on approximations of the EPDF or ECDF. However, those are less straight forward to determine for multi-level ensembles, since there is no associated measure [54, 86].

Here, we give a short survey of selected approaches for the assessment of multi-level ensemble forecasts. In the case of scalar observations, Gregory and Cotter [62] suggest to resample a single-level ensemble such that the classical evaluation tools can be employed. Hereby, the resampled ensemble is a set of new scalar values $(y_e^L)_{e=1}^{N_r}$ for $N_r \leq N^0 + \sum_{l=1}^{L}(N^l - 1)$ with dedicated analytical weights. With the resampled single-level ensemble, PIT histograms or the average CRPS can be calculated as in Section 4.3.

Alternative ways, that also work in two dimensions, take advantage of multi-level estimation. Given an observation y, the identity $F(y) = \mathbb{E}[\mathbb{1}_{(-\infty,y]}(y^*)]$, where y^* is distributed according to the CDF F, can be used to re-define the PIT value u from Section 4.3 in terms of an expected value. Then, the expected value can be approximated by the multi-level estimator. However, the multi-level ensemble size is not optimised for this quantity of interest and due to the discontinuity the approximation converges poorly [42]. This leads to artefacts like a non-monotonous ECDF and PIT values outside the interval between 0 and 1. Therefore, the indicator function can be replaced with kernel-based smoothing to diminish artefacts [129].

Moreover, a polynomial approximation to the PDF can be calculated based on Legendre polynomials and the maximisation of the Shannon entropy [9]. In doing so, the coefficients in the optimisation problem are set using the multi-level estimation. The numerical optimisation involves iterative solvers that are not guaranteed to converge, but when converged the resulting ECDF is monotonously increasing from 0 to 1. With approximations of the CDF, it becomes possible to re-use PIT histograms and the CRPS from Section 4.3 also for multi-level ensembles.

Chapter 6

Paper Contributions

The path towards improved local ocean and drift forecasting is genuinely interdisciplinary. Therefore, the papers in this thesis traverse through different scientific fields. While each paper focuses on a particular problem, they all contribute to the same goal and are thereby closely connected. This is a typical example that developments in applied computational statistics require to link knowledge from several mathematical disciplines to solve the problem at hand.

The papers in this thesis cover multiple aspects in the data assimilation value chain. Starting from the design of a simplified ocean model and its numerical simulation, via a filtering case study, to state-of-the-art assimilation with multi-level ensembles, the papers explore the suitability of advanced methods for their application in local ocean drift forecasting systems by proofs-of-concepts. Hereby, each paper is dedicated to one the research objectives from Chapter 1.

Paper I Considerations for the FVM that is used solve the SWE. Field of numerical mathematics.

Paper II Simplified ocean modelling with the SWE respecting different dynamical modes for efficient drift trajectory forecasting. Field of mathematical modelling for EPS in oceanography.

Paper III In-depth comparison of two conceptually different filters and discussion of localisation strategies tailored for sparse observations in simplified oceanographic applications. Field of data assimilation.

Paper IV Combination of the multi-level approach from the field of uncertainty quantification with practical EnKF-based data assimilation.

Open-Source Software

Reproducibility is a key principle in scientific research and refers to the practice of making methodologies, data, and computational workflows openly available so that others can verify and replicate the findings. In computational science, open-source code plays a vital roles in enabling reproducible science, advancing scientific knowledge, and promoting transparency and collaboration [93, 94]. As all papers in this thesis rely essentially on numerical and statistical implementations, all supplementary material is available in an open persistent repository alongside with the manuscripts to foster to the reproduction and extension of the presented results. The source code and data is published under the GNU Public Licence version 3.

Paper I

Reducing Numerical Artifacts by Sacrificing Well-Balance for Rotating Shallow-Water Flow

Håvard Heitlo Holm, Florian Beiser

Finite Volumes for Complex Applications X—Volume 2,
Hyperbolic and Related Problems

DOI: 10.1007/978-3-031-40860-1_19

This contribution was presented by Håvard at the FVCA10 conference 2023 in Strasbourg (France).

The CDKLM scheme is well-balanced for geostrophic jets along the coordinate axes. To achieve this, it employs a reconstruction based on potential energies with respect to geostrophic imbalance and a standard-upwind (SU) flux in one of the vector components instead of the central-upwind (CU) flux as in the other components, recall Section 2.1. In this paper, we show that this choice of fluxes can lead to oscillatory artefacts in cases that differ from geostrophic jets. In particular, by considering an independent implementation of KP, we confirm that the main source of this numerical behaviour is the flux choice and not the reconstruction. Therefore, we propose to use a weighted sum of SU and CU flux instead of the pure SU flux to suppress the unintended artefacts.

For the testing of the scheme, we consider five cases that are relevant for oceanographic applications. We present that already a small fraction of CU is able to reduce oscillations. On the contrary, the well-balance guarantee is lost, but we note that this guarantee for CDKLM anyways only holds for the jets and not for other types of geostrophic steady states. However, for suitable choices of the slope limiter parameter in the reconstruction step, we see that even a pure CU flux preserves geostrophic jets within acceptable tolerances.

While FVM schemes generally have few tuning parameters, we have hereby introduced one more for the weighting of the flux terms. This comes at the advantage of more realistic simulations, though, and based on a test case with challenging topography and currents, we suggest to use a fraction of 0.8 for the SU flux and 0.2 for the CU flux.

Contribution

While the development of generally well-balanced schemes is still ongoing [39], specific FVMs are only well-balanced for particular steady states.

We demonstrate that a FVM that is well-balanced for a superset of steady states compared to another gives more numerical artefacts when applied to other general problems. This shows that the use of a simpler flux expression in favour for the theoretical results is not fruitful for practical applications. With these results, this paper supports the discussion around the choice of numerical solvers for realistic situations where no scheme is well-balanced for all general steady-states.

In particular, the CDKLM scheme for the rotational SWE is well-balanced for a superset of geostrophic steady states compared to the KP scheme, but it replaces a CU with a SU flux. By weighting both flux formulations, we have adapted numerical simulations for simplified ocean model to produce more realistic results.

Further Work

The development of numerical FVM schemes is not the core of this work, but is a necessary ingredient on the way to the full workflow. Therefore, it will be relevant to follow the advances in the development of new well-balanced schemes.

Comments

This paper tackles a problem that has been observed in some debugging cases, but for a long time the cause of these artefacts was not found. Finally, in this paper, we identify the issue and present a pragmatic strategy for how to mitigate these oscillations where we sacrifice the well-balance in favour for the reduction of numerical artefacts. The test cases are taken from previous publications [73, 15] and we see generally only minor improvements compared to the overall flow patterns what implies that their results stay qualitatively valid.

Xing et al. [144] note that well-balanced schemes whose equilibrium is closest to the present case should be used. However, this becomes difficult in practice. Geostrophically balanced states are central in many real-world applications, nonetheless, we still believe that improved realistic simulations are more important than the well-balanced guarantee in academic test cases as long as the loss of well-balance in those cases is within acceptable limits.

Paper II

Combining Barotropic and Baroclinic Simplified Models for Drift Trajectory Predictions

Florian Beiser, Håvard Heitlo Holm, Martin Lilleeng Sætra, Nils Melsom Kristensen, Kai Håkon Christensen

In review

A summary of this paper was presented in the October 2023 instalment of Ocean Modelling Seminar organised by Tor Nordam in SINTEF Ocean under the title 'Combining simplified models in GPU OCEAN*'. The seminar series takes place in Trondheim, but is broadcast online to the interested audience.*

In this study, we place emphasis on simplified ocean models as lightweight decision-support tool for ensemble predictions of drift trajectories. We exploit the SWE and the GPU OCEAN software for the efficient simulation of barotropic and baroclinic dynamics independently, i.e. we use the reduced-gravity model as a simplified model for first-order baroclinic dynamics as outlined in Section 2.2. The choice of using either the barotropic or baroclinic model or both is determined based on the specific local conditions in the area of interest, and the existence of a well-defined mixed layer. We describe how the same structure of equations is re-used and how the system can be parameterised. Given the uncertainties, when complex effects are parameterised and several parameters are not precisely known in realistic scenarios, we sample these randomly from appropriate probability distributions and analyse sensitivities. This means that the model error here is implicit, see eq. (3.3). Yet, the reduced-gravity model can be simulated faster in relation to the barotropic SWE, such that we can afford a large ensembles to represent the uncertainty adequately. By combining the currents from both simplified models, we construct large ensembles of drift trajectories for short-term prediction. As proof-of-concept, we showcase the feasibility of our approach for three distinct regions along the Norwegian coast and generate drift ensembles of up to 27,000 members.

Contribution

In this paper, we promote simplified ocean models as complementary tool. While operational ocean models prioritise physical complexity and become computationally expensive, we explore how lightweight simplified ocean models can be used for ensemble predictions and uncertainty representation. We demonstrate the fast prediction of drift trajectory ensembles using a computationally efficient framework.

In particular, the existing SWE simulation framework is expanded by the reduced-gravity model for respecting simplified baroclinic dynamics. Moreover, we present a concept to efficiently sample a large number of drift trajectories by the combination of simplified models for barotropic and baroclinic modes that pushes the ensemble size to new magnitudes. The efficient generation of large sample sets is fundamental for ensemble-based data assimilation and therewith this work can be seen as enabler for the combination of drift simulations and filtering.

Further Work

To leverage the light-weight computations even further, one could take advantage of non-linear data assimilation methods. Here, parameter choices that turn out to be a good representations of the true dynamics acquire larger weights, while those parameters that fit poorly are rejected. Thereby, the predictive power will be increased.

Moreover, the initialisation of models and ensembles is a well-known challenge in the oceanography community. For example, the definition of meaningful MLDs is non-trivial, but has substantial influence on the results. There is always potential for improving the initial conditions and the models that parameterise, e.g. wind forcing and friction. This will become more relevant when validating the ensemble drift trajectories against real drifter data.

Comments

While we categorised this work first as low-hanging fruit, the reality of ocean states crossed our assessment. The proper initialisation and parameterisation is essential, i.e. we have seen that the MLD and the baroclinic currents as integrated from three-dimensional models may not be geostrophically balanced. Therefore, the reduced-gravity model is easier to initialise in local areas such that this approach is mostly suited for local drift trajectory forecasting, which is in line with our original interests, though. We see significantly improved drift trajectories in the fjords, when also baroclinic dynamics is considered. Moreover, for drift trajectories, the wind acts twofold: on the drifting object itself and the currents in the upper ocean layer. The baroclinic model responds faster to winds than the barotropic model and hereby increases the realism. In a nutshell, this methodology can be useful as one applies the simplified framework and interprets the result with care. Furthermore, the generation of drift trajectory ensembles has direct implication for SAR cases.

Paper III

Comparison of Ensemble-Based Data Assimilation Methods for Sparse Oceanographic Data

Florian Beiser, Håvard Heitlo Holm, Jo Eidsvik

Quarterly Journal of the Royal Meteorological Society

DOI: 10.1002/qj.4637

Early versions of the content of this paper were presented at NORDSTAT 2021 in Tromsø (Norway) under the title 'Comparison of ensemble-based data assimilation methods for drift trajectory forecasting' and at the EnKF Workshop 2022 in Balestrand (Norway) under the title 'Handling sparse observations in ensemble-based filtering with an application to drift trajectory forecasting'.

In this paper, we focus on spatially very sparse in-situ observations and compare two ensemble-based data assimilation methods, namely the IEWPF and the ETKF with localisation. We elaborate on the handling of sparse observations $N_y \ll N_x$ and localisation in the context of both methods. We go step-by-step through the update of the IEWPF and describe how these concepts are built into the IEWPF by design. Hereby, all properties of the IEWPF are tightly dependent on the structure of the model error covariance matrix $\boldsymbol{Q}$. Moreover, we explore what happens if different $\boldsymbol{Q}$ matrices are used in the optimal proposal. For the ETKF, we employ covariance localisation in observation space. Together with serial processing of observations, this gives us good control of the correlations between observations and of the computational costs. We calculate the updates only for grid cells within the localisation radius, and since the Kalman gain is never explicitly constructed in the ETKF, we apply tapering in the final analysis computation step.

As a test case, we use the double jet where the experiment is set up with 450,000 state variables and 120 observation variables. For the comparison of the data assimilation methods, we investigate a broad range of evaluation metrics: quantitative skill scores, qualitative spatial state estimation, and drift trajectory forecasting. First of all, we emphasise that a set of metrics, rather than a single one, should always be used when comparing different methods to gain a deeper insight. Then, we conclude that the IEWPF does not degenerate in this application, but introduces artefacts originating from the model error covariance matrix into the ensemble spread. In the ETKF with localisation, we utilised relaxation-to-prior that is dependent on a tuning factor. Upon proper tuning, the ETKF with localisation outperformed the IEWPF in all metrics.

Contribution

This paper provides the first extensive and structured comparison of the IEWPF with an established version of the EnKF respecting the special scenario of sparse observations. Moreover, we present an elaborate set of metrics to gain insight in the filtering results of two conceptually different methods.

In particular, we dwell on tailored techniques for sparse in-situ buoy observations and on characteristics of the assimilation step itself in the context of the SWE model.

Further Work

Even though this study is rather self-contained, parts of the results open up for a discussion on parameter optimisation in the filter. In particular, the parametrisation of the covariance structures in IEWPF could be a topic of further analytical considerations. From a practical perspective, the parameters in the localisation and relaxation could be more interesting.

Comments

The setting of this paper is motivated by the conditions during SAR operations, i.e. only simplified ocean models are feasible due to their computational efficiency and only sparse in-situ observations are available for assimilation. In this work, we tailor data assimilation methods to these conditions and this study is therefore relevant for the identification of suitable filters. The findings herein support our choice to utilise the EnKF with the employed localisation scheme in our next article.

While Holm et al. [76] focused on GPU-acceleration, we have shifted our focus to the comparison with the ETKF and sacrificed the GPU discussion in this paper. In addition to the SWE model, we also include a linear Gaussian example that provides an analytical reference solution. This example allows us to verify our implementations, analyse the impact of tuning parameters in the localisation, and emphasise the importance of using a comprehensive set of evaluation metrics.

Paper IV

Multi-Level Data Assimilation for Simplified Ocean Models

Florian Beiser, Håvard Heitlo Holm, Kjetil Olsen Lye, Jo Eidsvik
In review

The presentation at the ISDA conference 2023 in Bologna (Italy) with the title 'Rank Histogram Estimators for Multi-level Data Assimilation' originated from discussions around this article.

We pursue the gain of computational efficiency in the data assimilation cycle for the EnKF by employing multi-level methods. Therefore, we commence by revising the MLEnKF for the GPU OCEAN framework. We put special effort into the discussion of the configuration of the multi-level ensemble and of the practical applicability of the MLEnKF in a relevant setting with simplified ocean models. To that end, we investigate the discrepancy between theoretical and practical scaling of computational costs, analyse the coupling between the levels, and their effects for the multi-level speed-up. This means that we determine trial experiments to set the values for computational costs C^l and the variances V^l from Section 5.2. While the choice of the quantity of interest, i.e. the function g, emerges as a central design choice for the configuration of a multi-level ensemble, we disclose that data assimilation routines necessitate the estimation of various quantities of interest. Moreover, we incorporate localisation into the Kalman gain construction and a mitigation strategy for negative eigenvalues in the estimated covariance matrices.

We resume to the double jet case, but in contrast to Paper III we use a finer resolution and a Karhunen-Loeve-type model error. On a hierarchy of four nested grid levels, the coarsest grid clearly lacks details that are resolved on the finer grids. We set up three multi-level configurations that share the same theoretical statistical error for a quantity of interest as a given single-level ensemble, but achieve a theoretical speed-up of up to more than a factor 2 in the forward step. Numerical experiments for the double jet case confirm that the state estimation with the MLEnKF is of the same quality as with the corresponding single-level EnKF while the spread of the multi-level ensemble is slightly higher. Finally, we present the usability of the multi-level ensemble for drift trajectory forecasting by exploiting ensemble statistics, see Section 3.2.

Contribution

Multi-level Monte Carlo estimation is an established tool in the uncertainty quantification community, but the application of the multi-level idea to spatio-temporal data assimilation problems is so far still limited. With this paper, we elevate the MLEnKF one step from analytical test cases to application-driven proof-of-concept studies. Moreover, we provide an extensive discussion around the construction of suited multi-level ensembles.

In particular, we design multi-level data assimilation for simplified ocean models, where the forward step exploits simulations on different resolutions, and investigate the applicability of the MLEnKF for the shallow-water equations with sparse observations.

Further Work

This work can be extended in several directions. Our example was only one step towards more realistic settings, and we had periodic boundary conditions and a flat sea bed. To continue this direction, the consistent incorporation of a varying bathymetry and land mask will become relevant. Hereby, special care has to be dedicated again to the coupling between the levels such that artificial noise is avoided.

The calculation of computational costs is purely based on the forward step, while the update step is assumed to be of negligible cost for all methods. For a naive implementation of the MLEnKF, we have observed that it takes longer than a naive implementation of the single-level EnKF. Naturally, it could be worth to examine this effect and do the technical labour to tune the implementation of the update step itself as the total run time matters.

In addition, we have discussed that suboptimal scaling of the GPU OCEAN simulator on very coarse grids diminishes the speed-up through the use of multi-level methods. Also the multi-level ensemble benefits from the fast computation on the fine levels, but the potential of MLDA could be increased when approaches for the acceleration of coarse levels are inspected. While the computational costs of small problem sizes is usually not relevant in the development of ocean modelling software, it matters for multi-level methods.

Furthermore, it is conceptually not necessary to use the same model equation on all levels. While keeping the variables projectable and the perturbations transferable, the simplified models in our study could be extended by levels $l > L$ from more complex models. In such multi-fidelity hierarchies [64], the increased accuracy of the results does not only come from increased resolution but also from increased physical complexity.

Comments

While we keep structurally the same data assimilation method as in Paper III, the multi-level method focuses on accelerating the data assimilation cycle by a speed-up in the forward step. As computational efficiency is a key for drift predictions in SAR scenarios, reducing computational time for the generation of trajectories is beneficial.

With the formulation of the MLEnKF, we stay close to the formulation of Chernov et al. [24], but we use practical evaluation metrics as we do not restrict ourselves to analytical cases. Also Fossum et al. [50] employ multi-level data assimilation in a practically relevant case, but we do not decouple the higher levels by hybridisation with Bayesian model averaging in our notion. Still, it is remarkable how little the MLEnKF results are sensitive to the evaluated configurations. Moreover, in the composition of the paper, the design of the model error became a discussion in itself, since it has to be communicated between two levels each and has to be appropriately parameterised.

Finally, the application of MLDA is only beneficial in very specific conditions. On the one hand, the correlation between the finest levels has to be sufficiently strong to obtain a speed-up, and on the other hand, there is no need to refine if the fine resolution does not contribute with increased detail information. Hereby, the double jet is actually a representative case and it is challenging for multi-level estimators since the dynamics between the jets becomes turbulent with many small-scale details.

Chapter 7

Concluding Remarks and Outlook

In this thesis, we have pursued a complementary approach for local drift forecasting motivated by search-and-rescue scenarios. Rather than relying on a single prediction from a complex model, we have employed ensembles of simplified ocean models to represent the probability distribution of the currents and to assimilate observation data from in-situ measurements into the forecasts. The computational efficiency of the shallow-water model and the flexibility of the numerical solvers have facilitated the generation of large ensembles on different resolutions and multi-level data assimilation has enabled to refine the statistics for high-resolution forecasts.

Numerical simulations of simplified ocean models can be nested locally into operational forecasts and predict drift trajectories on demand. Here, we have utilised the shallow-water equations for the simplified modelling of barotropic and, in the presence of a distinct mixed-layer, also baroclinic dynamics.

In a Monte Carlo approach, we used ensembles of simulations to represent uncertainty in the forecast arising, among others, from the initial states and the dynamical model. Furthermore, this approach has taken benefit of assimilating measurements that had not been considered in the operational workflow. While we assume that observational data is sparse in time-critical applications, we have analysed tailored data assimilation techniques that steer the ensemble forecasts towards the observations and generally improve the forecast skills.

Finally, as computational efficiency plays a crucial role in search-and-rescue operations, we have explored ensembles on a hierarchy of levels and their potential for further computational speed-ups. Therefore, we have used the multi-level ensemble Kalman filter to assimilate observational data into shallow-water ensembles.

7.1 Concluding Remarks

Seen in the bigger picture, the combination of simplified models and data assimilation enables rapid forecasts with flexible resolutions and uncertainty information in local areas, making this approach a well-suited addition for search-and-rescue scenarios. The work in this thesis constitutes a proof-of-concept and an in-depth study of the methods in the development chain towards a complementary system for drift trajectory forecasting.

While simplified methods do not aim to replace the operational forecasting systems, the concepts in this thesis represent novel pathways and build a base for further steps to establish the combination of simplified models and data assimilation as on-demand tool. In the frame of developing such a complementary system, this thesis provides scientific contributions for the proof-of-concept of the involved dynamical model and data assimilation techniques. Also in the scientific context, our considerations are motivated by the application in mind and the results show the value, but also limitations, of shallow-water models and multi-level data assimilation as a special-purpose ensemble prediction system for drift trajectory forecasting.

For the simplified ocean models, we have confronted well-balanced finite-volume methods and purely barotropic models with realistic conditions accentuating the need for pragmatic solutions. In the finite-volume scheme, we have discussed the trading of well-balance in favour for reducing numerical artefacts in classical oceanographic cases and have improved the results for general applications. Moreover, we have investigated an extension of the barotropic shallow-water model by the reduced-gravity models and have manifested the efficient generation of large ensembles of drift trajectories.

Continuing with ensemble-based data assimilation, we have compared two conceptually different filtering methods for the handling of sparse observations. Here, we have evaluated a recent particle filter and a version of the ensemble Kalman filter, such that we have gained further insights into their implicit or explicit localisation. In this assessment, we exhibit that the use of advanced non-linear data assimilation methods does not always lead to better forecast statistics than linear updating methods.

Last, we have brought multi-level data assimilation one step ahead and have addressed practical challenges on the way. We have presented the applicability of multi-level ensemble and the associated potential for computational speed-ups for challenging data assimilation problems. Here, we have succeeded to apply the ensemble Kalman filter for simplified ocean models.

From my personal perspective, as if our project leader Jan Erik Stiansen would ask for an appraisal of the research in this thesis, the general approach of simplified models and multi-level data assimilation can find its place in future ensemble prediction systems for drift trajectories. While offline drift models will stay faster and complex models will stay more precise, ensembles of simplified models fit in between. The advantages of efficient forecasts with realistic uncertainty representation and the assimilation of observations that would have otherwise been ignored are prevalent.

However, to add value to trajectory predictions, all methods have to be adequate. While the barotropic shallow-water model is hereby rarely sufficient for drifter modelling in protected fjords, the supplementary reduced-gravity model enables even larger ensembles, but its robust initialisation in complex conditions remains a challenge for further research.

We have identified suitable data assimilation methods for sparse in-situ observations. Moreover, we have incorporated multi-level ensembles into the architecture, where the theoretical computational cost was halved in an exemplary scenario with the shallow-water equations. Transferring the acquired knowledge to the broader perspective of a complementary forecast system for search-and-rescue systems, the practical impact of multi-level data assimilation for local high-resolution ensemble forecasts depends on multiple factors. The computational scaling is one aspect and, for parallel code infrastructures, this depends on the number of grids cell on the level of interest. While the restriction to local domains casts scepticism whether the massive parallelisation in the GPU OCEAN simulation framework will be fully occupied, yielding suboptimal scaling, the high resolution of interest indicates big problem sizes and allures the utilisation of cost efficient coarser grids. In addition, the correlation of the levels in relation to the ensemble variance on the coarsest level indicates whether one can expect a reduction of computational costs in the ensemble simulation compared to single-level ensembles. These variances are still unknown for real-word scenarios, but could be subject of further investigations.

7.2 Outlook

For practical impact on search-and-rescue operations at sea, it would be necessary to elevate the discussed methods onto a robust operational level with support for all potentially occurring real-world conditions. This would involve a lot of technical work, but also gives rise to further scientific investigations.

As the complex ocean models and data assimilation frameworks will develop in future, those will also become computationally more efficient. However, if simplified models with rapid data assimilation ripens further, they can find their place as complementary first-response systems in the operational architecture. As mentioned in Chapter 6 for each individual paper, there are several directions to expand the research. Most prominently for the technology readiness of the general approach are developments for respecting real-world conditions. Beyond this, multi-resolution simulations, transfer to other application scenarios or machine learning forecasts are interesting topics.

Real-world Conditions

The most natural extension would be to take the methods from this thesis to real-world domains. As the SWE model already accommodates for real-world domains and topographies, the challenges will lie in the ensemble initialisation and generating a realistic ensemble spread through out the simulation.

The initial conditions are not perfectly known and the ensemble is supposed to properly account for this uncertainty. However, for instance in the case of NorKyst, only a single forecast is available such that it requires innovative ways to initialise an ensemble that represents a realistic uncertainty. Moreover, we have used two different types of model errors in this thesis for temporal perturbations of the ocean states, but for both types it remains an open challenge to create a realistic ensemble spread respecting the actual uncertainty in the dynamics [49]. These facts demand the analysis of real-world data compared to the simplified models and identification of suitable perturbation designs, this can, for instance, include machine learning techniques for error corrections [140].

The aforementioned steps will be relevant to both single-level and multi-level ensemble methods. For the multi-level case also further work, e.g. for mismatching land masks on different levels, see Chapter 6, is needed and the variances between the levels should be analysed to evaluate the potential for a computational speed-up through the use of multi-level methods.

Thereafter, it will be interesting to benchmark the approach of simplified ocean models and data assimilation against operational drift trajectory forecasts and real drifter data.

Assessment of Multi-Level Ensemble Forecasts

With real-world data, the proper assessment of ensemble forecast will become pivotal. For the evaluation of multi-level ensemble forecasts with respect to observational data by conventional techniques, like probability integral transform histograms or scoring rule, multiple approaches have been presented in Chapter 5. Hereby, all methods involve preparatory steps, such as resampling, smoothing, or polynomial approximation, before the actual assessment. Consequently, it could be interesting to study the potential effect of these methods on the validation outcomes in more detail.

Multi-resolution Models

In Paper IV, we have employed global coarsening in our examples, but it may be prohibitive to coarsen in the full domain as too many features are lost, e.g. in some coastal or turbulent areas, whilst in other areas coarsening is still feasible. Therefore, it could be relevant to keep high-resolution in some areas and coarsen only in others [84].

Vice versa, the ambition can be to even increase the resolution in specific areas of interest [116]. High-resolution data of the topography may be easier accessible than corresponding forecasts for the ocean currents on such a fine grid. Hereby, challenges will occur, for example, when initialising currents around small islands that have not been resolved in the operational data. For ensembles of multi-resolution models, the same locally refined grid could be used for all ensemble members or a hierarchy of such grids could supply a multi-level ensemble. Accordingly, either the single-level or the multi-level data assimilation methods from this thesis could be applied. In contrast, super resolution data assimilation [4] follows an alternative approach and simulates only coarse ensemble members globally, but uses neural nets to fill in high-resolution features. Here it can be interesting to compare both approaches in the end.

Combined Barotropic and Baroclinic Simplified Models

Foremost, the initialisation of the reduced-gravity model could be further explored. Such simplified approaches do not have the ambition to be a perfect model of the real dynamics, but enhanced by observational data they could be advanced to special-purpose tools for drift trajectory prediction. Therefore, the impact of data assimilation on combined barotropic and baroclinic simplified models could be analysed. For details, see Chapter 6.

Other Applications

Search-and-rescue operations have motivated the setting of this thesis, but the developed methods are not restricted to this. Storm surges are dominantly a barotropic phenomenon, such that the barotropic shallow-water model could be re-used for storm surge modelling and rapid sea level rise forecasting [85]. In addition to current observations, measurements of the sea level would be a relevant data source for assimilation in such an application [138]. The framework could be extended to other current-driven tracers as long as the interest lies in local short-term trajectories. For ice berg drift [23], the use of an ensemble of simplified ocean model together with stochastic drift and forcing parameters could represent the uncertainty in the driving currents better than a single deterministic current field with corresponding parameter samples. Observations in the arctic would rather originate from satellite pictures than from buoys. Furthermore, supplementary models, for instance for feed or waste in fish farming, and data collection types could be coupled with the shallow-water model and the ensemble Kalman filter. Also in other societal and economical relevant contexts, such a combination of models can be applied. For example, the predictions for the spread of an acute algae bloom require efficient models and fast updates [120]. In all cases, the data assimilation techniques would need to be adapted to the specific application. This may include multi-level formulations of other versions of the EnKF, when the data is no longer sparse.

Machine Learning Models

Machine learning models are an emerging technology also in typical data assimilation applications, like meteorology or oceanography. After an extensive training period, these models produce partial or full forecasts very fast as they circumvent to solve the physical equations directly. These methods can either be used in combination with classical data assimilation [13, 12] or replace the traditional workflow completely as presented very recently for weather forecasting [109, 89, 7, 83]. During all further development on simplified models for drift trajectory forecasting, it could be reasonable to keep an eye on the progress of machine learning models whether those can be a useful and practical enhancement or supplement.

Bibliography

[1] J. Albretsen and L. Asplin. Hvilken betydning har oppløsning for kyst-og fjordmodeller?-Validering og representasjonsberegninger av strømmodeller med eksempler fra Sulafjorden, Møre og Romsdal. Technical report, Institute of Marine Research, 2021.

[2] J. Albretsen, A. K. Sperrevik, A. Staalstrøm, A. D. Sandvik, F. Vikebø, and L. Asplin. NorKyst-800 Report No. 1 User Manual and Technical Descriptions. *Fisken og Havet*, 2:1–48, 2011.

[3] R. N. Bannister. A review of operational methods of variational and ensemble-variational data assimilation. *Quarterly Journal of the Royal Meteorological Society*, 143(703):607–633, 2017.

[4] S. Barthélémy, J. Brajard, L. Bertino, and F. Counillon. Super-resolution data assimilation. *Ocean Dynamics*, 72(8):661–678, 2022.

[5] M. Bentsen, I. Bethke, J. B. Debernard, T. Iversen, A. Kirkevåg, Ø. Seland, H. Drange, C. Roelandt, I. A. Seierstad, C. Hoose, et al. The Norwegian earth system model, NorESM1-M–Part 1: Description and basic evaluation of the physical climate. *Geoscientific Model Development*, 6(3):687–720, 2013.

[6] M. J. Berger and J. Oliger. Adaptive mesh refinement for hyperbolic partial differential equations. *Journal of computational Physics*, 53(3):484–512, 1984.

[7] K. Bi, L. Xie, H. Zhang, X. Chen, X. Gu, and Q. Tian. Pangu-weather: A 3D high-resolution model for fast and accurate global weather forecast. *arXiv preprint arXiv:2211.02556*, 2022.

[8] C. Bierig and A. Chernov. Convergence analysis of multilevel Monte Carlo variance estimators and application for random obstacle problems. *Numerische Mathematik*, 130(4):579–613, 2014.

[9] C. Bierig and A. Chernov. Approximation of probability density functions by the multilevel monte carlo maximum entropy method. *Journal of Computational Physics*, 314:661–681, 2016.

[10] C. H. Bishop, B. J. Etherton, and S. J. Majumdar. Adaptive sampling with the ensemble transform Kalman filter. Part I: Theoretical aspects. *Monthly weather review*, 129(3):420–436, 2001.

[11] R. Bleck. An oceanic general circulation model framed in hybrid isopycnic-Cartesian coordinates. *Ocean Modelling*, 4(1):55 – 88, 2002. doi: 10.1016/S1463-5003(01)00012-9.

[12] M. Bocquet. Surrogate modeling for the climate sciences dynamics with machine learning and data assimilation. *Frontiers in Applied Mathematics and Statistics*, 9:1133226, 2023.

[13] J. Brajard, A. Carrassi, M. Bocquet, and L. Bertino. Combining data assimilation and machine learning to infer unresolved scale parametrization. *Philosophical Transactions of the Royal Society A*, 379:20200086, 2021.

[14] A. Brodtkorb. *Scientific Computing on Heterogeneous Architectures*. PhD thesis, University of Oslo, 2010.

[15] A. Brodtkorb and H. Holm. Coastal ocean forecasting on the gpu using a two-dimensional finite-volume scheme. *Tellus, Series A: Dynamic Meteorology and Oceanography*, 73(1):1–22, 2021.

[16] A. R. Brodtkorb, C. Dyken, T. R. Hagen, J. M. Hjelmervik, and O. O. Storaasli. State-of-the-art in heterogeneous computing. *Scientific Programming*, 18(1):1–33, 2010.

[17] U. Brönner, M. Sonnewald, and M. Visbeck. Digital twins of the ocean can foster a sustainable blue economy in a protected marine environment. *The International Hydrographic Review*, 29(1):26–40, 2023.

[18] K. Brusdal, J.-M. Brankart, G. Halberstadt, G. Evensen, P. Brasseur, P. J. van Leeuwen, E. Dombrowsky, and J. Verron. A demonstration of ensemble-based assimilation methods with a layered OGCM from the perspective of operational ocean forecasting systems. *Journal of Marine Systems*, 40:253–289, 2003.

[19] G. Burgers, P. J. Van Leeuwen, and G. Evensen. Analysis scheme in the ensemble Kalman filter. *Monthly weather review*, 126(6):1719–1724, 1998.

[20] A. Carrassi, M. Bocquet, L. Bertino, and G. Evensen. Data assimilation in the geosciences: An overview of methods, issues, and perspectives. *Wiley Interdisciplinary Reviews: Climate Change*, 9(5):e535, 2018.

[21] M. Castro-Díaz, E. Fernández-Nieto, J. González-Vida, and C. Parés-Madroñal. Numerical treatment of the loss of hyperbolicity of the two-layer shallow-water system. *Journal of Scientific Computing*, 48(1):16–40, 2011.

[22] Y. Chen and D. S. Oliver. Localization and regularization for iterative ensemble smoothers. *Computational Geosciences*, 21(1):13–30, 2017.

[23] S. Cheng, A. Aydoğdu, P. Rampal, A. Carrassi, and L. Bertino. Probabilistic forecasts of sea ice trajectories in the Arctic: Impact of uncertainties in surface wind and ice cohesion. *Oceans*, 1(4):326–342, 2020. doi: 10.3390/oceans1040022.

[24] A. Chernov, H. Hoel, K. Law, F. Nobile, and R. Tempone. Multilevel ensemble Kalman filtering for spatio-temporal processes. *Numerische Mathematik*, 147(1):71–125, 2021. doi: 10.1007/s00211-020-01159-3.

[25] A. Chertock, M. Dudzinski, A. Kurganov, and M. Lukácová-Medvidová. Well-balanced schemes for the shallow water equations with Coriolis forces. *Numer. Math.*, 138(4):939–973, 2017. doi: 10.1007/s00211-017-0928-0.

[26] N. Chopin, O. Papaspiliopoulos, et al. *An introduction to sequential Monte Carlo*, volume 4. Springer, 2020.

[27] K. H. Christensen, Ø. Breivik, K.-F. Dagestad, J. Röhrs, and B. Ward. Short-term predictions of oceanic drift. *Oceanography*, 31(3):59–67, 2018.

[28] K. A. Cliffe, M. B. Giles, R. Scheichl, and A. L. Teckentrup. Multilevel Monte Carlo methods and applications to elliptic PDEs with random coefficients. *Computing and Visualization in Science*, 14:3–15, 2011.

[29] J. Cummings, L. Bertino, P. Brasseur, I. Fukumori, M. Kamachi, M. J. Martin, K. Mogensen, P. Oke, C. E. Testut, J. Verron, et al. Ocean data assimilation systems for GODAE. *Oceanography*, 22(3):96–109, 2009.

[30] K.-F. Dagestad, J. Röhrs, Ø. Breivik, and B. Ådlandsvik. OpenDrift v1.0: A generic framework for trajectory modelling. *Geoscientific Model Development*, 11(4):1405–1420, 2018.

[31] S. B. Dalsøren, J. Albretsen, and L. Asplin. New validation method for hydrodynamic fjord models applied in the Hardangerfjord, Norway. *Estuarine, Coastal and Shelf Science*, 246:107028, 2020.

[32] F. J. Davidson, A. Allen, G. B. Brassington, Ø. Breivik, P. Daniel, M. Kamachi, S. Sato, B. King, F. Lefevre, M. Sutton, et al. Applications of GODAE ocean current forecasts to search and rescue and ship routing. *Oceanography*, 22(3):176–181, 2009.

[33] H. Davies. A lateral boundary formulation for multi-level prediction models. *Quarterly Journal of the Royal Meteorological Society*, 102(432):405–418, 1976.

[34] V. de Aguiar, J. Röhrs, A. M. Johansson, and T. Eltoft. Assessing ocean ensemble drift predictions by comparison with observed oil slicks. *Frontiers in Marine Science*, 10:1122192, 2023.

[35] M. de la Asunción, M. Castro, J. Mantas, and S. Ortega. Numerical simulation of tsunamis generated by landslides on multiple GPUs. *Advances in Engineering Software*, 99:5–2, 2016.

[36] P. De Mey-Frémaux, N. Ayoub, A. Barth, R. Brewin, G. Charria, F. Campuzano, S. Ciavatta, M. Cirano, C. A. Edwards, I. Federico, et al. Model-observations synergy in the coastal ocean. *Frontiers in Marine Science*, 6:436, 2019.

[37] D. P. Dee. Bias and data assimilation. *Quarterly Journal of the Royal Meteorological Society: A journal of the atmospheric sciences, applied meteorology and physical oceanography*, 131(613):3323–3343, 2005.

[38] M. Destouches, P. Mycek, and S. Gürol. Multivariate extensions of the multilevel best linear unbiased estimator for ensemble-variational data assimilation. *arXiv preprint arXiv:2306.07017*, 2023.

[39] V. Desveaux and A. Masset. A fully well-balanced scheme for shallow water equations with Coriolis force. *Communications in Mathematical Sciences*, 20 (7):187–900, 2022.

[40] T. J. Dodwell, C. Ketelsen, R. Scheichl, and A. L. Teckentrup. A hierarchical multilevel Markov chain Monte Carlo algorithm with applications to uncertainty quantification in subsurface flow. *SIAM/ASA Journal on Uncertainty Quantification*, 3(1):1075–1108, 2015. doi: 10.1137/130915005.

[41] A. Doucet, S. Godsill, and C. Andrieu. On sequential Monte Carlo sampling methods for Bayesian filtering. *Statistics and computing*, 10:197–208, 2000.

[42] D. Elfverson, F. Hellman, and A. Målqvist. A multilevel monte carlo method for computing failure probabilities. *SIAM/ASA Journal on Uncertainty Quantification*, 4(1):312–330, 2016.

[43] K. L. Elmore. Alternatives to the chi-square test for evaluating rank histograms from ensemble forecasts. *Weather and forecasting*, 20(5):789–795, 2005.

[44] G. Evensen. Sequential data assimilation with a nonlinear quasi-geostrophic model using monte carlo methods to forecast error statistics. *Journal of Geophysical Research: Oceans*, 99(C5):10143–10162, 1994.

[45] G. Evensen. The ensemble Kalman filter: Theoretical formulation and practical implementation. *Ocean dynamics*, 53:343–367, 2003.

[46] G. Evensen, F. C. Vossepoel, and P. J. van Leeuwen. *Data assimilation fundamentals: A unified formulation of the state and parameter estimation problem*. Springer Nature, 2022.

[47] G. Evensen et al. *Data assimilation: The ensemble Kalman filter*, volume 2. Springer, 2009.

[48] C. Farmer. Upscaling: a review. *International journal for numerical methods in fluids*, 40(1-2):63–78, 2002.

[49] M. Fisher. Background error covariance modelling. In *Seminar on Recent Development in Data Assimilation for Atmosphere and Ocean*, pages 45–63. Shinfield Park, Reading, 2003.

[50] K. Fossum, T. Mannseth, and A. Stordal. Assessment of multilevel ensemble-based data assimilation for reservoir history matching. *Computational Geosciences*, 24(1):21–39, 2020. doi: 10.1007/s10596-019-09911-x.

[51] J. Galewsky, R. K. Scott, and L. M. Polvani. An initial-value problem for testing numerical models of the global shallow-water equations. *Tellus A: Dynamic Meteorology and Oceanography*, 56(5):429–440, 2004.

[52] M. B. Giles. Multilevel Monte Carlo path simulation. *Operations Research*, 56 (3):607–617, 2008. doi: 10.1287/opre.1070.0496.

[53] M. B. Giles. Multilevel Monte Carlo methods. *Acta numerica*, 24:259–328, 2015.

[54] M. B. Giles, T. Nagapetyan, and K. Ritter. Multilevel monte carlo approximation of distribution functions and densities. *SIAM/ASA journal on Uncertainty Quantification*, 3(1):267–295, 2015.

[55] T. Gneiting and M. Katzfuss. Probabilistic forecasting. *Annual Review of Statistics and Its Application*, 1:125–151, 2014.

[56] T. Gneiting and A. E. Raftery. Strictly proper scoring rules, prediction, and estimation. *Journal of the American statistical Association*, 102(477):359–378, 2007.

[57] T. Gneiting, F. Balabdaoui, and A. E. Raftery. Probabilistic forecasts, calibration and sharpness. *Journal of the Royal Statistical Society Series B: Statistical Methodology*, 69(2):243–268, 2007.

[58] T. Gneiting, L. I. Stanberry, E. P. Grimit, L. Held, and N. A. Johnson. Assessing probabilistic forecasts of multivariate quantities, with an application to ensemble predictions of surface winds. *Test*, 17:211–235, 2008.

[59] N. Gordon, D. Salmond, and A. Smith. Novel approach to nonlinear/non-Gaussian Bayesian state estimation. *IEE Proceedings F Radar and Signal Processing*, 140(2):107, 1993. doi: 10.1049/ip-f-2.1993.0015.

[60] S. Gottlieb and C.-W. Shu. Total variation diminishing Runge-Kutta schemes. *Math. Comput.*, 67(221):73–85, 1998. doi: 10.1090/s0025-5718-98-00913-2.

[61] A. Gregory. *Multilevel ensemble data assimilation*. PhD thesis, Imperial College London, 2017.

[62] A. Gregory and C. Cotter. On the calibration of multilevel monte carlo ensemble forecasts. *Quarterly Journal of the Royal Meteorological Society*, 143 (705):1929–1935, 2017.

[63] S. Griffies. *Fundamentals of ocean climate models*. Princeton university press, 2018.

[64] A. Gruber, M. Gunzburger, L. Ju, R. Lan, and Z. Wang. Multifidelity Monte Carlo estimation for efficient uncertainty quantification in climate-related modeling. *Geoscientific Model Development*, 16(4):1213–1229, 2023.

[65] K. Gundersen, A. Oleynik, N. Blaser, and G. Alendal. Semi-conditional variational auto-encoder for flow reconstruction and uncertainty quantification from limited observations. *Physics of Fluids*, 33(1), 2021.

[66] T. R. Hagen, M. O. Henriksen, J. M. Hjelmervik, and K.-A. Lie. How to solve systems of conservation laws numerically using the graphics processor as a high-performance computational engine. *Geometric Modelling, Numerical Simulation, and Optimization: Applied Mathematics at SINTEF*, pages 211–264, 2007. doi: 10.1007/978-3-540-68783-2_8.

[67] T. Haiden, M. Dahoui, B. Ingleby, P. De Rosnay, C. Prates, E. Kuscu, T. Hewson, L. Isaksen, D. Richardson, H. Zuo, et al. Use of in situ surface observations at ECMWF. Technical report, European Centre for Medium Range Weather Forecasts, 2018.

[68] D. Ø. Halvorsen, A. Dallolio, and M. O. Alver. Assimilation of heterogeneous measurements at different spatial scales in the Arctic ocean and Norwegian sea. In *OCEANS 2022, Hampton Roads*, pages 1–10. IEEE, 2022. doi: 10.1109/oceans47191.2022.9977376.

[69] T. M. Hamill. Interpretation of rank histograms for verifying ensemble forecasts. *Monthly Weather Review*, 129(3):550–560, 2001.

[70] S. Heinrich. Multilevel Monte Carlo methods. In *Large-Scale Scientific Computing: Third International Conference, LSSC 2001 Sozopol, Bulgaria, June 6–10, 2001 Revised Papers 3*, pages 58–67. Springer, 2001.

[71] H. Hoel, K. J. H. Law, and R. Tempone. Multilevel ensemble Kalman filtering. *SIAM Journal on Numerical Analysis*, 54(3):1813–1839, 2016. doi: 10.1137/15m100955x.

[72] H. H. Holm. *Efficient Forecasting of Drift Trajectories using Simplified Ocean Models and Nonlinear Data Assimilation on GPUs*. PhD thesis, NTNU, 2020.

[73] H. H. Holm, A. R. Brodtkorb, G. Broström, K. H. Christensen, and M. L. Sætra. Evaluation of selected finite-difference and finite-volume approaches to rotational shallow-water flow. *Communications in Computational Physics*, 27(4):1234–1274, 2020.

[74] H. H. Holm, A. R. Brodtkorb, and M. L. Sætra. GPU computing with Python: Performance, energy efficiency and usability. *Computation*, 8(1): 4, 2020. doi: 10.3390/computation8010004.

[75] H. H. Holm, M. L. Sætra, and A. R. Brodtkorb. Data assimilation for ocean drift trajectories using massive ensembles and GPUs. In *Finite Volumes for Complex Applications IX-Methods, Theoretical Aspects, Examples: FVCA 9, Bergen, Norway, June 2020 IX*, pages 715–723. Springer, 2020.

[76] H. H. Holm, M. L. Sætra, and P. J. Van Leeuwen. Massively parallel implicit equal-weights particle filter for ocean drift trajectory forecasting. *Journal of Computational Physics: X*, 6:100053, 2020.

[77] P. L. Houtekamer and H. L. Mitchell. Data assimilation using an ensemble Kalman filter technique. *Monthly Weather Review*, 126(3):796–811, 1998.

[78] P. L. Houtekamer and H. L. Mitchell. A sequential ensemble Kalman filter for atmospheric data assimilation. *Monthly Weather Review*, 129(1):123–137, 2001.

[79] P. L. Houtekamer and F. Zhang. Review of the ensemble Kalman filter for atmospheric data assimilation. *Monthly Weather Review*, 144(12):4489–4532, 2016.

[80] B. R. Hunt, E. J. Kostelich, and I. Szunyogh. Efficient data assimilation for spatiotemporal chaos: A local ensemble transform Kalman filter. *Physica D: Nonlinear Phenomena*, 230(1-2):112–126, 2007.

[81] M. Idžanović, E. S. U. Rikardsen, and J. Röhrs. Forecast uncertainty and ensemble spread in surface currents from a regional ocean model. *Frontiers in Marine Science*, 10, 2023. doi: 10.3389/fmars.2023.1177337.

[82] A. Jasra, K. Kamatani, K. J. H. Law, and Y. Zhou. Multilevel particle filters. *SIAM Journal on Numerical Analysis*, 55(6):3068–3096, 2017. doi: 10.1137/17m1111553.

[83] R. Keisler. Forecasting global weather with graph neural networks. *arXiv preprint arXiv:2202.07575*, 2022.

[84] Ø. Klemetsdal, O. Møyner, A. Moncorgé, H. Nilsen, K.-A. Lie, et al. High-resolution compositional reservoir simulation with dynamic coarsening and local timestepping for unstructured grids. *SPE Journal*, 26(06):4157–4173, 2021.

[85] N. M. Kristensen, L. P. Røed, and Ø. Sætra. A forecasting and warning system of storm surge events along the Norwegian coast. *Environmental Fluid Mechanics*, pages 1–23, 2022. doi: 10.1007/s10652-022-09871-4.

[86] S. Krumscheid and F. Nobile. Multilevel monte carlo approximation of functions. *SIAM/ASA Journal on Uncertainty Quantification*, 6(3):1256–1293, 2018.

[87] A. Kurganov and G. Petrova. A second-order well-balanced positivity preserving central-upwind scheme for the Saint-Venant system. *Commun Math Sci*, 5(1):133–160, 2007. doi: 10.4310/cms.2007.v5.n1.a6.

[88] A. Kurganov, S. Noelle, and G. Petrova. Semidiscrete central-upwind schemes for hyperbolic conservation laws and Hamilton-Jacobi equations. *SIAM J Sci Comput*, 23(3):707–740, 2001. doi: 10.1137/s1064827500373413.

[89] R. Lam, A. Sanchez-Gonzalez, M. Willson, P. Wirnsberger, M. Fortunato, F. Alet, S. Ravuri, T. Ewalds, Z. Eaton-Rosen, W. Hu, et al. GraphCast: Learning skillful medium-range global weather forecasting. *arXiv preprint arXiv:2212.12794*, 2022.

[90] J. Latz, I. Papaioannou, and E. Ullmann. Multilevel sequential2 Monte Carlo for Bayesian inverse problems. *Journal of Computational Physics*, 368:154–178, 2018.

[91] P. F. Lermusiaux. Estimation and study of mesoscale variability in the Strait of Sicily. *Dynamics of Atmospheres and Oceans*, 29(2-4):255–303, 1999.

[92] R. LeVeque. *Finite Volume Methods for Hyperbolic Problems*. Cambridge University Press, 2004.

[93] R. J. LeVeque, I. M. Mitchell, and V. Stodden. Reproducible research for scientific computing: Tools and strategies for changing the culture. *Computing in Science & Engineering*, 14(04):13–17, 2012.

[94] K.-A. Lie. On Holden's seven guidelines for scientific computing and development of open-source community software. *preprint*, 2017.

[95] K.-A. Lie and S. Noelle. On the artificial compression method for second-order nonoscillatory central difference schemes for systems of conservation laws. *SIAM J Sci Comput*, 24(4):1157–1174, 2003. doi: 10.1137/s1064827501392880.

[96] K. Lye. *Computation of statistical solutions of hyperbolic systems of conservation laws*. PhD thesis, ETH Zurich, 2020.

[97] G. Madec and the NEMO team. *NEMO ocean engine*. Note du Pôle de modélisation, Institut Pierre-Simon Laplace (IPSL), France, No 27, 2008.

[98] M. J. Martin, M. Balmaseda, L. Bertino, P. Brasseur, G. Brassington, J. Cummings, Y. Fujii, D. Lea, J.-M. Lellouche, K. Mogensen, et al. Status and future of data assimilation in operational oceanography. *Journal of Operational Oceanography*, 8(sup1):s28–s48, 2015.

[99] A. Melsom, F. Counillon, J. H. LaCasce, and L. Bertino. Forecasting search areas using ensemble ocean circulation modeling. *Ocean Dynamics*, 62:1245–1257, 2012.

[100] S. Mishra and C. Schwab. Sparse tensor multi-level Monte Carlo finite volume methods for hyperbolic conservation laws with random initial data. *Mathematics of Computation*, 81(280):197–018, 2012. doi: 10.1090/s0025-5718-2012-02574-9.

[101] S. Mishra, C. Schwab, and J. Šukys. Multilevel Monte Carlo finite volume methods for shallow water equations with uncertain topography in multi-dimensions. *SIAM Journal on Scientific Computing*, 34(6):B761–B784, Jan. 2012.

[102] S. Mishra, U. Fjordholm, and R. Abgrall. Numerical methods for conservation laws and related equations. Lecture notes for Numerical Methods for Partial Differential Equations, ETH Zurich, 2019.

[103] M. Morzfeld, D. Hodyss, and C. Snyder. What the collapse of the ensemble Kalman filter tells us about particle filters. *Tellus A: Dynamic Meteorology and Oceanography*, 69(1):1283809, 2017.

[104] F. Müller. *Stochastic methods for uncertainty quantification in subsurface flow and transport problems*. PhD thesis, ETH Zurich, 2014.

[105] P. Mycek and M. De Lozzo. Multilevel Monte Carlo covariance estimation for the computation of Sobol' indices. *SIAM/ASA Journal on Uncertainty Quantification*, 7(4):132–348, 2019.

[106] M. Nezhadali. *Multilevel assimilation of inverted seismic data*. PhD thesis, University of Bergen, 2023.

[107] P. R. Oke, G. Larnicol, E. M. Jones, V. Kourafalou, A. Sperrevik, F. Carse, C. A. Tanajura, B. Mourre, M. Tonani, G. Brassington, et al. Assessing the impact of observations on ocean forecasts and reanalyses: Part 2, Regional applications. *Journal of Operational Oceanography*, 8(sup1):s63–s79, 2015.

[108] E. Ott, B. R. Hunt, I. Szunyogh, A. V. Zimin, E. J. Kostelich, M. Corazza, E. Kalnay, D. Patil, and J. A. Yorke. A local ensemble Kalman filter for atmospheric data assimilation. *Tellus A: Dynamic Meteorology and Oceanography*, 56(5):415–428, 2004.

[109] J. Pathak, S. Subramanian, P. Harrington, S. Raja, A. Chattopadhyay, M. Mardani, T. Kurth, D. Hall, Z. Li, K. Azizzadenesheli, et al. FourCastNet: A global data-driven high-resolution weather model using adaptive fourier neural operators. *arXiv preprint arXiv:2202.11214*, 2022.

[110] J. Poterjoy. A localized particle filter for high-dimensional nonlinear systems. *Monthly Weather Review*, 144(1):59–76, 2016.

[111] J. Rabault, T. Nose, G. Hope, M. Müller, Ø. Breivik, J. Voermans, L. R. Hole, P. Bohlinger, T. Waseda, T. Kodaira, et al. OpenMetBuoy-v2021: An easy-to-build, affordable, customizable, open-source instrument for oceanographic measurements of drift and waves in sea ice and the open ocean. *Geosciences*, 12(3):110, 2022.

[112] A. E. Raftery, T. Gneiting, F. Balabdaoui, and M. Polakowski. Using bayesian model averaging to calibrate forecast ensembles. *Monthly weather review*, 133 (5):1155–1174, 2005.

[113] L. Røed. *Atmospheres and Oceans on Computers*. Springer, 2019.

[114] L. P. Røed. Documentation of simple ocean models for use in ensemble predictions. Technical Report 3, MET Norway, 2012.

[115] J. Röhrs, Y. Gusdal, E. Rikardsen, M. Durán Moro, J. Brændshøi, N. M. Kristensen, S. Fritzner, K. Wang, A. K. Sperrevik, M. Idžanović, et al. Barents-2.5 km v2.0: An operational data-assimilative coupled ocean and sea ice ensemble prediction model for the Barents Sea and Svalbard. *Geoscientific Model Development Discussions*, 2023:1–31, 2023.

[116] M. Sætra, A. Brodtkorb, and K.-A. Lie. Efficient GPU-implementation of adaptive mesh refinement for the shallow-water equations. *Journal of Scientific Computing*, 63:23–48, 2015.

[117] Ø. Saetra, H. Hersbach, J.-R. Bidlot, and D. S. Richardson. Effects of observation errors on the statistics for ensemble spread and reliability. *Monthly Weather Review*, 132(6):1487–1501, 2004.

[118] P. Sakov and L. Bertino. Relation between two common localisation methods for the EnKF. *Computational Geosciences*, 15:225–237, 2011.

[119] P. Sakov, F. Counillon, L. Bertino, K. Lisæter, P. Oke, and A. Korablev. TOPAZ4: an ocean-sea ice data assimilation system for the North Atlantic and Arctic. *Ocean Science*, 8(4):633–656, 2012. doi: 10.5194/os-8-633-2012.

[120] I. Samdal and B. Edvardsen. Massive salmon mortalities during a chrysochromulina leadbeateri bloom in northern norway. *Harmful Algae News*, 64:4–5, 2020.

[121] D. Schaden and E. Ullmann. On multilevel best linear unbiased estimators. *SIAM/ASA Journal on Uncertainty Quantification*, 8(2):601–635, 2020.

[122] D. W. Scott. *Multivariate density estimation: Theory, practice, and visualization*. John Wiley & Sons, 2015.

[123] A. F. Shchepetkin and J. C. McWilliams. The regional oceanic modeling system (ROMS): A split-explicit, free-surface, topography-following-coordinate oceanic model. *Ocean Modelling*, 9(4):347–404, 2005. doi: 10.1016/j.ocemod.2004.08.002.

[124] J. Skauvold, J. Eidsvik, P. J. Van Leeuwen, and J. Amezcua. A revised implicit equal-weights particle filter. *Quarterly Journal of the Royal Meteorological Society*, 145(721):1490–1502, 2019.

[125] C. Snyder, T. Bengtsson, P. Bickel, and J. Anderson. Obstacles to high-dimensional particle filtering. *Monthly Weather Review*, 136(12):4629–4640, 2008.

[126] A. K. Sperrevik, K. H. Christensen, and J. Röhrs. Constraining energetic slope currents through assimilation of high-frequency radar observations. *Ocean Science*, 11(2):237–249, 2015.

[127] M. Sæatra. *Shallow Water Simulations on Graphics Hardware*. PhD thesis, University of Oslo, 2014.

[128] O. Talagrand, R. Vautard, and B. Strauss. Evaluation of probabilistic prediction systems. *Workshop on Predictability, 20-22 October 1997*, pages 1–26, 1997 1997.

[129] S. Taverniers, S. B. Bosma, and D. M. Tartakovsky. Accelerated multilevel monte carlo with kernel-based smoothing and latinized stratification. *Water Resources Research*, 56(9):e2019WR026984, 2020.

[130] P. G. Thoppil, S. Frolov, C. D. Rowley, C. A. Reynolds, G. A. Jacobs, E. Joseph Metzger, P. J. Hogan, N. Barton, A. J. Wallcraft, O. M. Smedstad, et al. Ensemble forecasting greatly expands the prediction horizon for ocean mesoscale variability. *Communications Earth & Environment*, 2(1):89, 2021.

[131] T. L. Thorarinsdottir, M. Scheuerer, and C. Heinz. Assessing the calibration of high-dimensional ensemble forecasts using rank histograms. *Journal of computational and graphical statistics*, 25(1):105–122, 2016.

[132] M. Tonani, M. Balmaseda, L. Bertino, E. Blockley, G. Brassington, F. Davidson, Y. Drillet, P. Hogan, T. Kuragano, T. Lee, et al. Status and future of global and regional ocean prediction systems. *Journal of Operational Oceanography*, 8(sup2):s201–s220, 2015.

[133] E. F. Toro. *Riemann solvers and numerical methods for fluid dynamics: a practical introduction*. Springer Science & Business Media, 2013.

[134] G. K. Vallis. *Essentials of atmospheric and oceanic dynamics*. Cambridge university press, 2019.

[135] P. J. Van Leeuwen. Efficient nonlinear data-assimilation in geophysical fluid dynamics. *Computers & Fluids*, 46(1):52–58, 2011.

[136] P. J. Van Leeuwen. A consistent interpretation of the stochastic version of the ensemble Kalman filter. *Quarterly Journal of the Royal Meteorological Society*, 146(731):2815–2825, 2020.

[137] P. J. Van Leeuwen, H. R. Künsch, L. Nerger, R. Potthast, and S. Reich. Particle filters for high-dimensional geoscience applications: A review. *Quarterly Journal of the Royal Meteorological Society*, 145(723):2335–2365, 2019.

[138] M. Verlaan, T. Zijlker, F. Zijl, and J. Sumihar. A bias-Kalman filter for operational storm-surge forecasting. In *9th International Symposium on Data Assimilation*, 2023.

[139] S. Vetra-Carvalho, P. J. Van Leeuwen, L. Nerger, A. Barth, M. U. Altaf, P. Brasseur, P. Kirchgessner, and J.-M. Beckers. State-of-the-art stochastic data assimilation methods for high-dimensional non-Gaussian problems. *Tellus A: Dynamic Meteorology and Oceanography*, 70(1):1–43, 2018.

[140] P. A. Watson. Applying machine learning to improve simulations of a chaotic dynamical system using empirical error correction. *Journal of Advances in Modeling Earth Systems*, 11(5):1402–1417, 2019.

[141] J. S. Whitaker and T. M. Hamill. Ensemble data assimilation without perturbed observations. *Monthly weather review*, 130(7):1913–1924, 2002.

[142] D. Wilks. On the reliability of the rank histogram. *Monthly Weather Review*, 139(1):311–316, 2011.

[143] D. S. Wilks. *Statistical methods in the atmospheric sciences*, volume 100. Academic press, 2011.

[144] Y. Xing, C.-W. Shu, and S. Noelle. On the advantage of well-balanced schemes for moving-water equilibria of the shallow water equations. *Journal of scientific computing*, 48(–):339–349, 2011.

[145] M. Zhu, P. J. Van Leeuwen, and J. Amezcua. Implicit equal-weights particle filter. *Quarterly Journal of the Royal Meteorological Society*, 142(698):1904–1919, 2016.

Part II

Scientific Papers

Paper I

Reducing Numerical Artifacts by Sacrificing Well-Balance for Rotating Shallow-Water Flow

Håvard Heitlo Holm, Florian Beiser

Finite Volumes for Complex Applications X—Volume 2,
Hyperbolic and Related Problems

DOI: 10.1007/978-3-031-40860-1_19

Reducing Numerical Artifacts by Sacrificing Well-Balance for Rotating Shallow-Water Flow

Håvard Heitlo Holm[1] and Florian Beiser[1,2]

[1]Mathematics and Cybernetics, SINTEF Digital, Oslo, Norway
[2]Department of Mathematical Sciences, NTNU, Trondheim, Norway

Abstract

We consider the problem of rotational shallow-water flow for which non-trivial rotating steady-state solutions are of great importance. In particular, we investigate a high-resolution central-upwind scheme that is well-balanced for a subset of these stationary solutions and show that the well-balanced design is the source of numerical artifacts when applied to more general problems. We propose an alternative flux evaluation that sacrifices the well-balanced property and demonstrate that this gives qualitatively better results for relevant test cases and real-world oceanographic simulations.

Keywords: high-resolution finite-volume schemes, rotating shallow-water equations, oceanography, numerical artifacts

1 Introduction

Over the past few years, we have developed a GPU-accelerated simulation framework [1] for oceanographic applications and ensemble prediction systems. At the core of the framework is a simplified ocean model based on the shallow-water equations in a rotational frame of reference. This hyperbolic system is solved using a slightly modified version of the numerical scheme proposed by Chertock et al. [2] (abbreviated as CDKLM). This is an explicit high-resolution finite-volume scheme that is conservative, second order, and consistent, formulated on Cartesian grids. Its main advantage compared to similar schemes is that it is well-balanced with respect to some non-trivial steady-state solutions in geostrophic balance, namely geostrophic jets along the coordinate axes. Hereby, the rotational pull on the jets is equal to the gravity-induced potential energy from a non-flat ocean surface. The geostrophic jets are however not the only steady-state solutions based on geostrophic balance, and in real-world oceanographic applications, rotational steady-states are often of greater importance.

The CDKLM scheme is based on central-upwind schemes [3], which are attractive as "black-box" solvers as they do not require solutions to the Riemann problem. An alternative to CDKLM is the earlier scheme proposed by Kurganov and Petrova [4] (abbreviated as KP), which also uses central-upwind flux evaluations but is not well-balanced for any non-trivial rotational steady-state solutions. When considering alternative numerical schemes, one that is well-balanced for some geostrophic steady-state solutions and one that is not, it is easy to choose to implement the former also for more complex applications. However, as we will show in this paper, one should be more careful in this selection.

In this work, we demonstrate that the CDKLM scheme gives oscillatory artifacts and show that we can achieve solutions that are qualitatively better for rotational flow by using a non-well-balanced variation of CDKLM. Thereafter, we continue by investigating how to tune the resulting finite-volume scheme when applied to real-world oceanographic problems.

2 Rotational Shallow Water Equations

The shallow water equations in a rotational frame of reference are given by

$$\begin{bmatrix} \eta \\ hu \\ hv \end{bmatrix}_t + \begin{bmatrix} hu \\ hu^2 + \frac{1}{2}gh^2 \\ huv \end{bmatrix}_x + \begin{bmatrix} hv \\ huv \\ hv^2 + \frac{1}{2}gh^2 \end{bmatrix}_y = \begin{bmatrix} 0 \\ fhv \\ -fhu \end{bmatrix} + \begin{bmatrix} 0 \\ ghH_x \\ ghH_y \end{bmatrix} \tag{1}$$

and conserve mass and momentum. The variable η represents the water surface as a deviation from the mean equilibrium depth H, so that $h = H + \eta$ becomes the total water depth. Momentum is given by hu and hv in x- and y-direction, respectively. Furthermore, g is the gravitational constant, and f is the Coriolis parameter, which is a function of latitude. We define the vector $\mathbf{q} = [\eta, hu, hv]^T$ to contain the conserved variables, so that we can write (1) as

$$\mathbf{q}_t + \boldsymbol{\mathcal{F}}(\mathbf{q})_x + \boldsymbol{\mathcal{G}}(\mathbf{q})_y = \mathbf{S}(\mathbf{q}) \ . \tag{2}$$

Rotating steady-states solutions of (1) are given by geostrophic balances, where

$$u_x + v_y = 0 \ , \qquad g\eta_x = fv \ , \quad \text{and} \quad g\eta_y = -fu \ . \tag{3}$$

In [2], the last two expressions are rewritten in terms of potential energies as

$$K(x,y) := g\left(\eta - \int_{-\infty}^{x} \frac{f}{g} v \, \mathrm{d}x'\right), \qquad L(x,y) := g\left(\eta - \int_{-\infty}^{y} \frac{f}{g} u \, \mathrm{d}y'\right), \tag{4}$$

so that they can be written as $K_x = 0$ and $L_y = 0$. In particular, the CDKLM scheme is well-balanced with respect to the geostrophic jets

$$u \equiv 0, \quad v_y \equiv 0, \quad \eta_y \equiv 0, \quad H_y \equiv 0, \quad K \equiv \text{const}, \tag{5}$$

$$v \equiv 0, \quad u_x \equiv 0, \quad \eta_x \equiv 0, \quad H_x \equiv 0, \quad L \equiv \text{const}, \tag{6}$$

which are special cases of (3).

3 Finite Volume Schemes

In the following, we summarize only the relevant parts of the CDKLM scheme; the reader can find all details in [2]. We start by discretizing the domain in a regular Cartesian grid with cells of size $(\Delta x, \Delta y)$, and define $\mathbf{Q}_{j,k}$ to be the average of $\mathbf{q}$ within the cell with center at $\big((j+\frac{1}{2})\Delta x,\ (k+\frac{1}{2})\Delta y\big)$. Equation (2) can then be written in semi-discrete form as

$$\frac{\partial \mathbf{Q}_{j,k}}{\partial t} = -\frac{\mathbf{F}_{j+1/2,k} - \mathbf{F}_{j-1/2,k}}{\Delta x} - \frac{\mathbf{G}_{j,k+1/2} - \mathbf{G}_{j,k-1/2}}{\Delta y} + \mathbf{S}(\mathbf{Q}_{j,k}). \tag{7}$$

The system is solved in time with the second-order total-variation-diminishing Runge-Kutta scheme [5] with time steps satisfying the CFL condition. In the rest of the paper, we focus on the spatial reconstruction and fluxes.

3.1 Well-balanced scheme

To design a well-balanced finite-volume scheme for (1) with respect to (5) and (6), Chertock et al. [2] propose to reconstruct the face values of $\mathbf{q}$ by computing the slopes of the equilibrium variables $\mathbf{p} = [u, v, K, L]^T$ rather than the slopes of $\mathbf{q}$ directly. Values for $K_{j,k}$ and $L_{j,k}$ are obtained by evaluating the integrals in (4) by a recursive sum starting from zero at the boundary. Note that the recursive sums for K and L mostly cancel in the reconstruction and are reduced to local operations [1, Sect. 3.1]. The slopes are then found by the generalized minmod limiter (c.f. [6]), which in the x-direction is

$$(\mathbf{p}_x)_{j,k} = \operatorname{minmod}\left(\theta \frac{\mathbf{p}_{j+1,k} - \mathbf{p}_{j,k}}{\Delta x}, \frac{\mathbf{p}_{j+1,k} - \mathbf{p}_{j-1,k}}{2\Delta x}, \theta \frac{\mathbf{p}_{j,k} - \mathbf{p}_{j-1,k}}{\Delta x}\right), \tag{8}$$

where $\theta \in [1, 2]$ controls numerical dissipation.

Using $(\mathbf{p}_x)_{j,k}$ and $(\mathbf{p}_x)_{j+1,k}$, we can reconstruct one-sided point values for $\mathbf{q}$ at the face between the two cells as $\mathbf{Q}^r_{j+1/2,k}$ and $\mathbf{Q}^l_{j+1/2,k}$ from the right and left, respectively, using the discretized version of (4) to reconstruct values for η. The flux terms in (7) are computed using the central-upwind (CU) scheme [3]

$$\mathbf{F}^{(i)}_{j+1/2,k} = \frac{a^+ \boldsymbol{\mathcal{F}}\left(\mathbf{Q}^l\right) - a^- \boldsymbol{\mathcal{F}}\left(\mathbf{Q}^r\right)}{a^+ - a^-} + \frac{a^+ a^-}{a^+ - a^-}\left(\mathbf{Q}^r - \mathbf{Q}^l\right) \tag{9}$$

for $i = 1, 2$, where we have omitted the subscript $(\cdot)_{j+1/2,k}$ for all $\mathbf{Q}$ (including its entries) and a variables for readability. The variables a^+ and a^- represent the largest positive and negative wave speeds at the cell interface, respectively,

$$a^{\pm} = \begin{matrix}\max\\ \min\end{matrix} \left\{u^l \pm \sqrt{gh^l}, \quad u^r \pm \sqrt{gh^r}, \quad 0\right\}. \tag{10}$$

For the scheme to be well-balanced with respect to (6), however, Chertock et al. [2] propose to use a standard-upwind (SU) scheme for $\mathbf{F}^{(3)}_{j+1/2,k}$, given by

$$\mathbf{F}^{(3)}_{j+1/2,k} = \begin{cases} h^r u^r v^r, & \text{if } u^r + u^l > 0, \\ h^l u^l v^l, & \text{otherwise.} \end{cases} \tag{11}$$

The scheme is defined analogously in the y-direction, where the CU flux in (9) is used for $\mathbf{G}^{(i)}_{j,k+1/2}$, $i = 1, 3$, and the SU in (11) is used for $\mathbf{G}^{(2)}_{j,k+1/2}$.

3.2 Unbalanced alternatives

As we will see in Section 4, the use of the SU flux in (11) produces artifacts when applying CDKLM to rotational and realistic problems. To investigate the problem, we consider a convex combination of the two fluxes

$$\mathbf{F}^{(3)}_{j+1/2,k} = \phi(\mathbf{F}_{SU})^{(3)}_{j+1/2,k} + (1-\phi)(\mathbf{F}_{CU})^{(3)}_{j+1/2,k}, \tag{12}$$

in which $\mathbf{F}_{CU}$ comes from (9), $\mathbf{F}_{SU}$ comes from (11), and $\phi \in [0, 1]$.

In contrast to CDKLM, KP reconstructs the slopes of $\mathbf{q}$ using the conserved variables directly and evaluates all flux components using the central-upwind scheme. We implement (12) also for KP and compare it with CDKLM to better assess the effects of different reconstructions and flux terms in isolation.

4 Numerical Experiments

We consider five experiments to evaluate the pros and cons of using the reconstruction and flux that make the scheme well-balanced for geostrophic jets.

Case A: Radial wave without rotation. First, we consider a simple radial wave in a non-rotating domain (meaning $f = 0$), initialized by

$$\eta(x, y, 0) = \exp^{-10^{-5}(x^2+y^2)}, \quad \text{and} \quad hu(x, y, 0) = hv(x, y, 0) = 0. \tag{13}$$

The domain consists of 400 × 400 cells with $\Delta x = \Delta y = 100\,\text{m}$, centered at the origin. The equilibrium depth is $H(x, y) = 60\,\text{m}$.

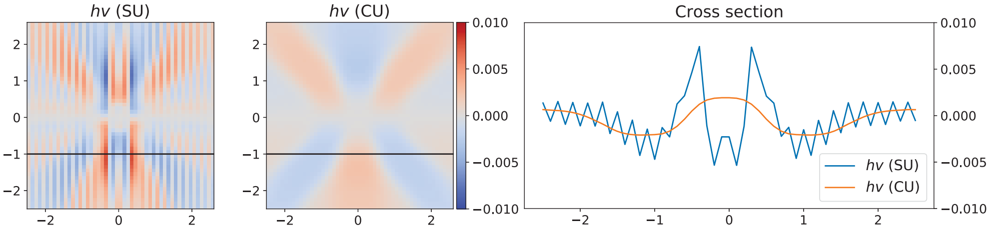

Figure 1: Artifacts in hv from an initial bump using CDKLM with SU flux (left) and CU flux (center), and cross section of hv at $y = -1\,\mathrm{km}$ (right).

Figure 1 shows hv at $t = 1000\,\mathrm{s}$ in the central part of the domain after most of the energy has traveled outwards. In the plots of the y-momentum shown in the two leftmost plots for the CDKLM scheme with SU and CU fluxes, we clearly see an oscillating artifact when using SU. This is even more pronounced in the right-hand plot of Fig. 1, which shows a cross section at $y = -1\,\mathrm{km}$. The CU flux gives numerical artifacts along the grid diagonals, but these are smooth in contrast to the SU artifacts. Both solutions are symmetric in hv and hu, and the artifacts are observed for any spatiotemporal resolution satisfying the CFL conditions with Courant number less or equal to 0.5.

Note that with $f = 0$, the CDKLM reconstruction reduces to that of the the KP scheme. We have implemented the KP scheme independently, and get exactly the same results as for CDKLM using both types of fluxes. This excludes the possibility that the artifacts are caused by a programming bug.

Case B: Rossby adjustment. We continue by considering Rossby adjustment, in which a rotational steady state is generated when running Case A with $f = 0.0012\,\mathrm{s}^{-1}$. The presence of Coriolis forces will establish a rotating bump in the center of the domain and create a steady-state that is not covered by the jets described in (5) and (6).

In Fig. 2, we consider the flux in (12) and assess different values for ϕ. The leftmost plot uses $\phi = 1.0$, which corresponds to a pure SU flux as in the original CDKLM scheme, whereas $\phi = 0.0$ to the far right corresponds to the CU flux. Again, hu and hv are symmetric, so we only show results for hv. We see a similar nonphysical oscillation pattern as in Case A when using the SU flux, and the rotating bump is dragged along the grid axes. In contrast, the CU flux results in a circular bump that captures (3) much better. It is interesting that it is sufficient to introduce just a small CU contribution to the SU flux to improve the numerical behavior, and the results are already significantly better with $\phi = 0.9$. The figures are visually the same when using KP.

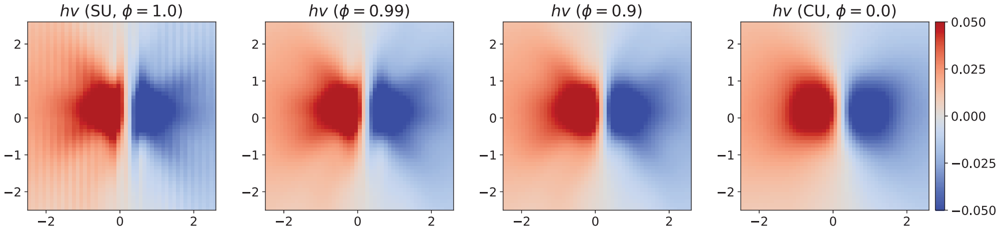

Figure 2: Numerical steady-states in hv from an initial bump with different ϕ-values in flux (12) in the presence of Coriolis forces.

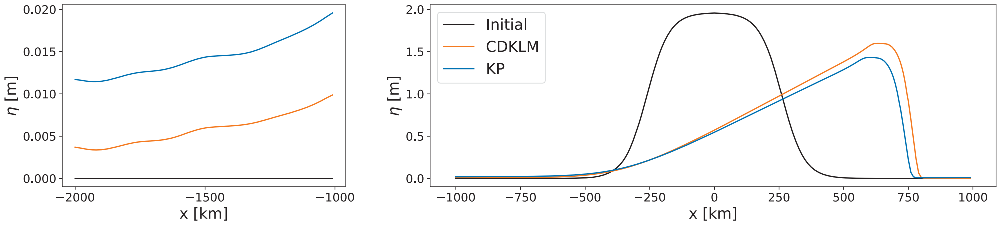

Figure 3: Cross-sectional plots of a Kelvin wave after ten periods for CDKLM and KP with CU flux and $\theta = 1.5$. Tail on the left and wave center on the right panel.

Case C: Kelvin wave. Kelvin waves are relatively fast travelling waves trapped along the coast by the Coriolis forces. They are travelling with the coast to their right on the Northern hemisphere and are important in realistic applications, as the tides often form them. Here, we consider a periodic domain in the east-west direction with wall boundary conditions in the north and south, and initialize a wave travelling eastwards along the southern wall. Sufficiently small waves follow linear physics and give periodic solutions, but the amplitudes used herein give nonlinear responses that develop a shock over time; see [7, Sect. 4.4] for details.

Figure 3 compares the CDKLM and KP schemes when using the CU flux and $\theta = 1.5$ for both, meaning that the only difference is in the slope reconstruction. The figure shows the solution after ten periods, corresponding to more than 60,000 time steps, at two cross sections for fixed y. We see how both schemes capture the nonlinear behavior of large waves. CDKLM manages, however, to maintain a taller wave front than KP, whereas KP produces a long nonzero tail. We argue that these results favor CDKLM for this case.

Case D: Geostrophic jets. We consider a double geostrophic jet that satisfies the steady-state given by (6), with one jet travelling eastward in the northern part of the domain and an westward jet in the southern part. We use periodic boundary conditions; the case is described in full in [8, Sect. 5]. This case exposes what we lose by not using the well-balanced SU flux for CDKLM, as this flux preserves this steady state for any slope limiter θ.

Figure 4 shows a cross section along y after running CDKLM for a long time using the CU flux with different values for θ. With $\theta = 1.0$, the numerical dispersion smooths out the jet streams significantly, but a moderate increase in θ compensates for using a non-balanced flux, and the jets stay captured and only cap the extrema slightly. With the maximal possible $\theta = 2.0$, we lose only 4.5% of the momentum in the center

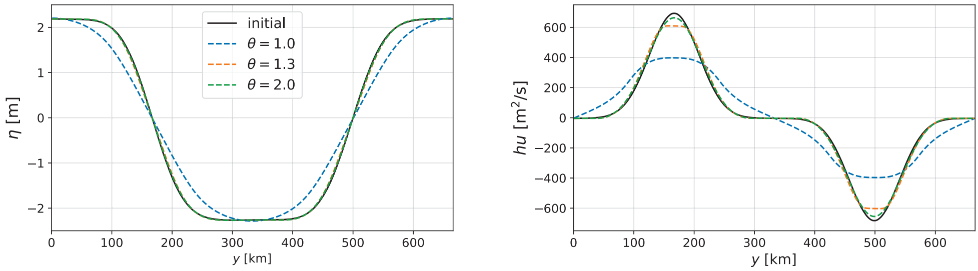

Figure 4: A double jet state after 9 simulation days with the CU flux: the plots show cross-sections of η (left) and hu (right).

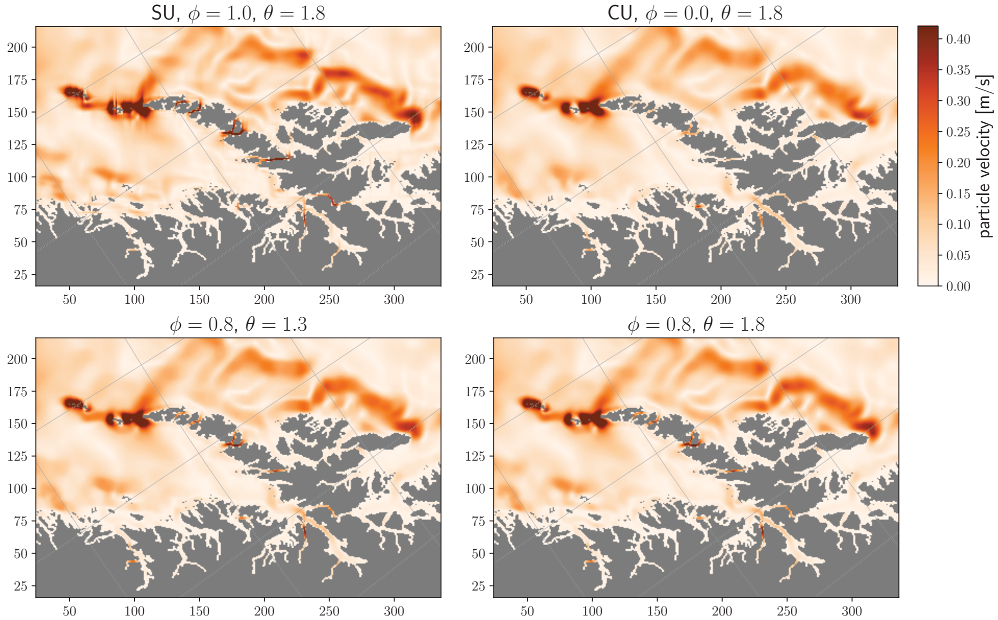

Figure 5: Real-world simulation for the Lofoten archipelago in Northern Norway. The axes show position within the computational domain in km.

of the jets.

To see how much of the CU flux we can incorporate without diminishing the preservation of geostrophic jets, we run the experiment for decreasing values of ϕ with fixed $\theta = 1.8$. For all $\phi \geq 0.52$, we conserve the maximum momentum within 4.5%.

Case E: Real-world simulation. Finally, we study the consequence of using different flux terms and slope limiters when using the CDKLM scheme for simulating a real-world oceanographic scenario. Here, we utilize the full GPU-accelerated framework from [1], in which land mask, bathymetry, initial and boundary conditions, domain orientation, and wind forcing are taken from the operational model NorKyst800 [9], with 800 m horizontal resolution.

Figure 5 shows water velocity at 23 h for a few selected values of ϕ and θ for CDKLM. The first thing to notice is how the SU flux gives visible artifacts around the outermost islands at $(100, 150)$. Secondly, the CU scheme gives visibly slower currents than SU, e.g., at $(300, 150)$. Since the tidal Kelvin wave follows the coast from left towards right, the Lofoten islands trap the tidal wave, causing strong currents in between the islands. With CU, we do not resolve this, but setting $\phi = 0.8$ helps significantly. It is hard to see visual differences between setting $\theta = 1.3$ and $\theta = 1.8$, but examining cross sections (not shown) reveals that we indeed get sharper fronts but no oscillations with the latter, which is preferred.

5 Conclusion

We have demonstrated numerical artifacts in the CDKLM scheme in cases that differ from geostrophic balanced jets along the coordinate axes. We identified the source of the oscillations to be the standard-upwind flux in the huv fluxes. By combining the standard-upwind flux with the central-upwind flux with a factor ϕ, we reduced unintended numerical behavior significantly and made the results more physical, even though we lose the well-balanced property for the jets.

We have illustrated the artifacts in Cases A and B, where Case B indicates that combining the SU flux with a small factor of CU is sufficient to smooth out these oscillations. In Case C, we see that the slope reconstruction in CDKLM still gives a small advantage over the more standard reconstruction used by the KP scheme. By using a large value θ in the slope limiter, we demonstrated that also pure CU can preserve the geostrophic jets from Case D within acceptable tolerances. Case E, however, shows that the pure CU flux is unable to capture strong realistic currents in narrow straits. The conclusion is then to use values close to $\phi = 0.8$ and $\theta = 1.8$ as flux parameter and slope limiter, respectively, for real-world oceanographic applications. This reduces the observed artifacts and gives a practical compromise between the well-balanced SU flux and the smoother behaving CU flux.

Acknowledgement This work is supported by the Research Council of Norway (RCN) through grant number 310515 (Havvarsel). The numerical examples are made with the GPU Ocean software [10], and can be reproduced by [11].

References

[1] A. Brodtkorb and H. Holm. Coastal ocean forecasting on the GPU using a two-dimensional finite-volume scheme. *Tellus A*, 73(1):1–22, 2021.

[2] A. Chertock, M. Dudzinski, A. Kurganov, and M. Lukácová-Medvidová. Well-balanced schemes for the shallow water equations with Coriolis forces. *Numer. Math.*, 138(4):939–973, 2017.

[3] A. Kurganov, S. Noelle, and G. Petrova. Semidiscrete central-upwind schemes for hyperbolic conservation laws and Hamilton-Jacobi equations. *SIAM J Sci Comput*, 23(3):707–740, 2001.

[4] A. Kurganov and G. Petrova. A second-order well-balanced positivity preserving central-upwind scheme for the Saint-Venant system. *Commun Math Sci*, 5(1):133–160, 03 2007.

[5] S. Gottlieb and C.-W. Shu. Total variation diminishing Runge-Kutta schemes. *Math. Comput.*, 67(221):73–85, 1998.

[6] K.-A. Lie and S. Noelle. On the artificial compression method for second-order nonoscillatory central difference schemes for systems of conservation laws. *SIAM J Sci Comput*, 24(4):1157–1174, 2003.

[7] H. Holm, A. Brodtkorb, G. Broström, K. Christensen, and M. Sætra. Evaluation of selected finite-difference and finite-volume approaches to rotational shallow-water flow. *Commun Comput Phys*, 27(4):1234–1274, 2020.

[8] H. Holm, M. Sætra, and P. van Leeuwen. Massively parallel implicit equal-weights particle filter for ocean drift trajectory forecasting. *J. Comput. Phys.: X*, 6(0314):100053, 2020.

[9] J. Albretsen, A. Sperrevik, A. Staalstrøm, A. Sandvik, and F. Vikebø. NorKyst-800 report no. 1: User manual and technical descriptions. Technical Report 2, Fisken og Havet, Institute of Marine Research, 2011.

[10] A. Brodtkorb, H. Holm, M. Sætra, and F. Beiser. GPU Ocean, 2023. DOI: 10.5281/zenodo.7938844.

[11] H. Holm and F. Beiser. Supplementary material for "Reducing numerical artifacts by sacrificing well-balance for rotating shallow-water flow", 2023. DOI: 10.5281/zenodo.7938887.

Paper II

Combining Barotropic and Baroclinic Simplified Models for Drift Trajectory Predictions

Florian Beiser, Håvard Heitlo Holm, Martin Lilleeng Sætra, Nils Melsom Kristensen, Kai Håkon Christensen

In review

This paper is under review for publication and is therefore not included.

Paper III

Comparison of Ensemble-Based Data Assimilation Methods for Sparse Oceanographic Data

Florian Beiser, Håvard Heitlo Holm, Jo Eidsvik

Quarterly Journal of the Royal Meteorological Society

DOI: 10.1002/qj.4637

Comparison of Ensemble-Based Data Assimilation Methods for Sparse Oceanographic Data

Florian Beiser[1,2], Håvard Heitlo Holm[1], and Jo Eidsvik[2]

[1]Mathematics and Cybernetics, SINTEF Digital, Oslo, Norway
[2]Department of Mathematical Sciences, NTNU, Trondheim, Norway

Abstract

Probabilistic forecasts in oceanographic applications, such as drift trajectory forecasts for search-and-rescue operations, face challenges due to high-dimensional complex models and sparse spatial observations. We discuss localisation strategies for assimilating sparse point observations and compare the implicit equal-weights particle filter and a localised version of the ensemble-transform Kalman filter. First, we verify these methods thoroughly against the analytic Kalman filter solution for a linear advection diffusion model. We then use a non-linear simplified ocean model to do state estimation and drift prediction. The methods are rigorously compared using a wide range of metrics and skill scores. Our findings indicate that both methods succeed in approximating the Kalman filter reference for linear models of moderate dimensions, even for small ensemble sizes. However, in high-dimensional settings with a non-linear model, we discover that the outcomes are significantly influenced by the dependence of the ensemble Kalman filter on relaxation and the particle filter's sensitivity to the chosen model error covariance structure. Upon proper relaxation and localisation parametrisation, the ensemble Kalman filter version outperforms the particle filter in our experiments.

Keywords: Spatio-temporal Statistics, Data Assimilation, Sparse Observations, Oceanographic Applications

1 Introduction

Data assimilation plays an essential role in enhancing the reliability of operational oceanographic and atmospheric forecasts by providing a framework to update and calibrate numerical models using observed data (Evensen, 2009; Asch et al., 2016). There is typically a wide array of available observations, such as satellite imagery, radar measurements, weather stations, and ocean buoys. These observations represent various physical quantities and can exhibit diverse connections to the dynamical model, necessitating substantial pre-processing efforts in operational prediction systems. Furthermore, assimilating the observations and running the complex numerical simulations often demands substantial computational resources.

In addition to regularly updated operational forecasts, there is a crucial need to provide targeted predictions for localized and time-sensitive scenarios, including search-and-rescue operations or sea contamination incidents (Breivik et al., 2013; Röhrs et al., 2018). To gain a better understanding of the local conditions in such situations, it is possible to deploy and gather in-situ observations using drifters. However, due to the fixed schedules for the operational forecasts, such in-situ observations will rarely be processed immediately by the operational data assimilation cycle. Instead, we aim to concurrently assimilate these observations into ensembles of efficient simplified models. This approach complements the traditional operational framework by enabling rapid predictions with quantification of associated uncertainties, possibly without requiring access to supercomputers. This study aims to investigate efficient data assimilation methods tailored for sparse observations for such scenarios.

We limit our scope to point observations, such as information gathered from buoys and drifters. Although these observations provide valuable insight into the ocean state at their respective locations, they are often separated by significant distances, necessitating spatio-temporal modelling to fill the gaps between sparse data points. In this paper, we utilize buoy information for two purposes: i) to constrain an advection diffusion process for particle concentration (Foss et al., 2021), and ii) to constrain drift trajectories in an simplified ocean model (Holm et al., 2020). Case i) involves a linear system in space-time, allowing us to explore the properties of the targeted data assimilation methods for sparse observations by comparing their results to the optimal analytic Kalman Filter (KF) solution. In contrast, case ii) deals with a highly non-linear dynamical model, prompting us to compare the different approaches using various performance metrics through synthetic simulation studies. Our primary motivation for focusing on case ii) is to improve short-term predictions for search-and-rescue missions by leveraging the utilisation of spatially sparse buoy observations.

To effectively model and estimate the uncertainty associated with discretised high-dimensional state variables governed by (non-)linear partial differential equations, we base our work on ensemble prediction and ensemble-based data assimilation. From a statistical perspective, data assimilation methods share the objective of representing a conditional distribution given the available observations. In our case, as we are motivated by search-and-rescue applications, we focus on filtering distributions rather than smoothers that also give improved estimates of past states. The ensemble Kalman filter (EnKF) proposed by Evensen (1994) is widely used in practice, and various numerical adaptions have been developed to address specific practical challenges and problems. Sparse observations pose challenges related to filtering efficiency and quality and our focus centers around the ensemble transform Kalman filter (ETKF, Bishop et al. (2001)) and explores localisation strategies for Kalman filters. In contrast to EnKF and its variants, particle filters (PFs, see, e.g. Van Leeuwen (2009) or Chopin and Papaspiliopoulos (2020)) are appealing as they do not rely on assumptions of a linear model and Gaussian probability distributions, at least in their most basic forms. However, PFs are less commonly employed in high-dimensional real-world applications due to the issue of degeneracy. Holm et al. (2020) demonstrated a modern PF approach based on the implicit equal-weight particle filter (IEWPF) proposed by Zhu et al. (2016), which shows promising forecasting results for drift trajectories.

In this paper, we systematically compare the statistical properties and performance of two ensemble-based data assimilation methods for sparse observations in practical oceanographic applications. We compare the ETKF with localisation for sparse observations against the state-of-the-art particle filter IEWPF. The comparison involves appraising their ability to reproduce analytic solutions for the linear model in the first case by assessing a range of statistical performance metrics and evaluating forecast skills in the non-linear case. Furthermore, we provide comprehensive discussions on the localisation techniques applied to the ETKF and the inherent localisation mechanism within the IEWPF.

The remainder of this article is organised as follows: Section 2 explicates state-of-the-art ensemble-based data assimilation techniques and reviews localisation strategies in the context of sparse observations. In Section 3, we use the dynamical model based on the advection diffusion equation to verify the relevant ensemble-based filtering methods against an analytical solution. Section 4 outlines the non-linear simplified ocean model for drift trajectory prediction, and we compare the performance of the data assimilation methods in this context. Finally, closing remarks are in Section 5.

2 The Data Assimilation Problem and Ensemble-based Filtering

Spatio-temporal quantities are denoted by $\boldsymbol{x}(t, \boldsymbol{s})$, for time $t > 0$ and location $\boldsymbol{s}$ where we restrict ourselves to $\boldsymbol{s} \in \mathbb{R}^2$. Upon discretisation of the spatio-temporal domain of interest, the locations are represented at grid nodes of spatial locations $(\boldsymbol{s}_i)_{i=1}^{N_s}$ and time steps t^n, $n = 1, \dots, N_T$, where we will work with equidistant time steps without loss of generality. The *state vector* at time t^n is denoted $\boldsymbol{x}^n \in \mathbb{R}^{N_X}$ and can hold more than one physical variable per location if necessary ($N_X \geq N_s$). In oceanographic applications, the dimension N_X is usually very high due to large domains and several physical variable.

The numerical model is embraced in the *model operator* $\mathcal{M}$. It propagates the state vector from the previous time step t^{n-1} to the current t^n, defining the so-called forecast state. The model usually describes the physics of the ocean. To account for uncertainty coming from external factors, unknown model parameters and non-modelled physics, a Gaussian model error $\boldsymbol{\nu}^n \sim \mathcal{N}(0, \boldsymbol{Q})$ is added every time step. It is assumed that $\boldsymbol{Q}$ is known, and that the error terms are uncorrelated in time. Starting from initial state $\boldsymbol{x}^0$, the model evolves as

$$\boldsymbol{x}^n = \mathcal{M}\boldsymbol{x}^{n-1} + \boldsymbol{\nu}^n, \qquad n = 1, \dots \; . \tag{2.1}$$

The oceanographic state $\boldsymbol{x}^n$ is often only partially observed and sometimes even indirectly. An *observation* is extracted from the true state vector by the measurement operator $\boldsymbol{H}$. Due to the nature of the problems within this work, we impose the restriction that this operator is linear, and that $\boldsymbol{H}$ only extracts variables directly from a subset of spatial locations, meaning that the matrix consists of at most one 1 entry per row and otherwise 0 entries. The observation locations could change every time step, but for the sake of eased reading we ignore this in our notation. Measurement and representation inaccuracies are represented by the addition of a zero-mean Gaussian error $\boldsymbol{\epsilon}^n \sim \mathcal{N}(0, \boldsymbol{R})$ with known covariance matrix $\boldsymbol{R}$ and no correlations in time. We model observations $\boldsymbol{y}^n \in \mathbb{R}^{N_Y}$ by

$$\boldsymbol{y}^n = \boldsymbol{H}\boldsymbol{x}^n + \boldsymbol{\epsilon}^n, \tag{2.2}$$

and assume that data comes from this observation model employed on the unknown true state. The covariance matrix $\boldsymbol{R}$ is assumed to be diagonal, representing conditional independence between the observations given the state variables. A characteristic of many oceanographic applications, and a key assumption in our setting, is that in-situ observations are spatially sparse and of low dimension compared to the high-dimensional state vector, i.e.,

$$N_Y \ll N_X. \tag{2.3}$$

Sequential *data assimilation* refers to the workflow of sequentially updating the probability density of the state variables as more data gets available. Often, this results in reduced uncertainty, especially in the neighbourhood of the observed variables. This kind of data assimilation is formalised in Bayes' rule. Using the state's density conditioned on all previous observations $p(\boldsymbol{x}^n|\boldsymbol{y}^{1:n-1})$ as the *forecast* (prediction or *prior*), this rule is used to assimilate the new observation $\boldsymbol{y}^n$ and thus provides the *analysis* (filtering or *posterior*) density $p(\boldsymbol{x}^n|\boldsymbol{y}^{1:n})$ of the state. With the independence assumption for the observation noise terms, this formalism can be applied recursively as

$$p(\boldsymbol{x}^n|\boldsymbol{y}^{1:n}) \propto p(\boldsymbol{y}^n|\boldsymbol{x}^n)p(\boldsymbol{x}^n|\boldsymbol{y}^{1:n-1}), \quad n = 1, 2, \dots, \tag{2.4}$$

starting with only prior information at the first time step.

Kalman filtering In the case of a linear model $\mathcal{M} = \boldsymbol{M}$ and an initial Gaussian distribution for the state $\boldsymbol{x}^0 \sim \mathcal{N}(\boldsymbol{\mu}^0, \boldsymbol{\Sigma}^0)$, all forecast and analysis distributions remain Gaussian. The data assimilation problem is then Gauss-linear and Bayes' formula (2.4) takes closed form solutions for the mean vectors and covariance matrices. Assuming that we have an analysis (superscript a) distribution characterised by the mean $\boldsymbol{\mu}^{n-1,a}$ and covariance matrix $\boldsymbol{\Sigma}^{n-1,a}$, the forecast (superscript f) distribution $\boldsymbol{x}^n|\boldsymbol{y}^{1:n-1} \sim \mathcal{N}(\boldsymbol{\mu}^{n,f}, \boldsymbol{\Sigma}^{n,f})$ is obtained by evolving the first and second moments from the previous time step to the next by

$$\boldsymbol{\mu}^{n,f} = \boldsymbol{M}\boldsymbol{\mu}^{n-1,a} \tag{2.5a}$$

$$\boldsymbol{\Sigma}^{n,f} = \boldsymbol{M}\boldsymbol{\Sigma}^{n-1,a}\boldsymbol{M}^\top + \boldsymbol{Q}. \tag{2.5b}$$

The analysis distribution $\boldsymbol{x}^n|\boldsymbol{y}^{1:n} \sim \mathcal{N}(\boldsymbol{\mu}^{n,a}, \boldsymbol{\Sigma}^{n,a})$ is achieved by assimilating the latest observation $\boldsymbol{y}^n$ via Bayes' rule for the given Gaussian model, resulting in

$$\boldsymbol{\mu}^{n,a} = \boldsymbol{\mu}^{n,f} + \boldsymbol{K}(\boldsymbol{y}^n - \boldsymbol{H}\boldsymbol{\mu}^{n,f}) \tag{2.6a}$$

$$\boldsymbol{\Sigma}^{n,a} = \boldsymbol{\Sigma}^{n,f} - \boldsymbol{K}\boldsymbol{\Sigma}^{n,f}\boldsymbol{K}^\top. \tag{2.6b}$$

Here, $\boldsymbol{K} = \boldsymbol{\Sigma}^{n,f}\boldsymbol{H}^\top(\boldsymbol{H}\boldsymbol{\Sigma}^{n,f}\boldsymbol{H}^\top + \boldsymbol{R})^{-1}$ is the Kalman gain, which in eq. (2.6a) maps the so-called innovation, $\boldsymbol{y}^n - \boldsymbol{H}\boldsymbol{\mu}^{n,f}$, to the state space using the state covariance matrix and the observation model. From the numerical perspective, note that the Kalman filter requires storage and propagation of the size $N_X \times N_X$ covariance matrix, which can be infeasible for high-dimensional systems.

Ensemble-based data assimilation In oceanographic applications the linearity assumptions of the Kalman filter are rarely met, and linearised approaches can suffer from divergence challenges. There is hence a need for more flexible methods, and ensemble-based approaches have been employed as a computationally feasible method to represent statistical solutions of non-linear systems, even for large N_X.

Therein, the continuous distribution of the state variable is approximated by an ensemble of realisations $(\boldsymbol{x}_e^n)_{e=1}^{N_e}$ and potentially by corresponding weights $(w_e)_{e=1}^{N_e}$. Following the Monte Carlo idea, the marginal distribution of $\boldsymbol{x}^n$ at time t^n becomes

$$p(\boldsymbol{x}^n) \approx \sum_{e=1}^{N_e} w_e^n \delta\left(\boldsymbol{x}^n - \boldsymbol{x}_e^n\right), \tag{2.7}$$

where δ is the Dirac delta function and $\sum_{e=1}^{N_e} w_e^n = 1$.

In the statistical literature (see, e.g. Asch et al. (2016) and Vetra-Carvalho et al. (2018)), there are two popular groups of methods for ensemble-based data assimilation, whose foundations and latest variants for the aforementioned problems is outlined in the next subsections.

2.1 Particle filters in oceanographic applications

PFs are ensemble-based methods for solving the data assimilation problem using the Monte Carlo approach. In their simplest form, starting from a weighted ensemble approximation for $p(\boldsymbol{x}^0)$ or $p(\boldsymbol{x}^{n-1}|\boldsymbol{y}^{1:n-1})$ in the form of eq. (2.7), the forecast distribution $p(\boldsymbol{x}^n|\boldsymbol{y}^{1:n-1})$ can be approximated by propagating each ensemble member $\boldsymbol{x}_e^{n-1}$ individually by the model eq. (2.1) to obtain $\boldsymbol{x}_e^n$. Plugging this into Bayes formula (2.4), the weights are updated as

$$w_e^n \propto p(\boldsymbol{y}^n|\boldsymbol{x}_e^n)p(\boldsymbol{x}_e^n|\boldsymbol{x}_e^{n-1})w_e^{n-1}. \tag{2.8}$$

Since ensemble members that have weights very close to zero do not contribute to the posterior probability distribution, it is common to combine eq. (2.8) with a discrete resampling of the ensemble members based on their weights (see, e.g. Van Leeuwen (2009); Chopin and Papaspiliopoulos (2020) for reviews of resampling schemes). In practice, this means that we discard ensemble members with low weights and duplicate those with higher weights, thus ensuring that computational resources are used to describe the non-negligible part of the probability distribution. In high-dimensional applications, however, these basic PFs are prone to degenerate, i.e. all but one ensemble member get a weight close to zero, leading to loss of statistical properties (Snyder et al., 2008).

Among other concepts, one way to counteract such degeneracy is to sample from a proposal density q_e instead of evolving the ensemble directly according to $p(\boldsymbol{x}_e^n|\boldsymbol{x}_e^{n-1})$ (van Leeuwen et al., 2019). The proposal density can be conditioned on the latest observation $\boldsymbol{y}^n$ and the previous state $\boldsymbol{x}_e^{n-1}$ for all ensemble members $e = 1, \dots, N_e$. The weights are then modified to

$$w_e^{n,*} = \frac{w_e^n}{q_e(\boldsymbol{x}_e^n|\boldsymbol{x}_{1:N_e}^{n-1}, \boldsymbol{y}^n)}.$$

The variance in the weights can be reduced in this way, and the minimal variance is achieved by $q_e(\boldsymbol{x}^n|\boldsymbol{x}_{1:N_e}^{n-1}, \boldsymbol{y}^n) = p(\boldsymbol{x}^n|\boldsymbol{x}_e^{n-1}, \boldsymbol{y}^n)$ as described in Doucet et al. (2000) and often referred to as the optimal proposal. Under the assumption of Gaussian errors and linear observation operator, which applies to our case, this proposal is a Gaussian distribution $\mathcal{N}\left(\boldsymbol{x}_e^{n,\text{opt}}, \boldsymbol{P}\right)$ with

$$\boldsymbol{x}_e^{n,\text{opt}} = \mathcal{M}\boldsymbol{x}_e^{n-1} + \boldsymbol{Q}\boldsymbol{H}^\top\left(\boldsymbol{H}\boldsymbol{Q}\boldsymbol{H}^\top + \boldsymbol{R}\right)^{-1}\left(\boldsymbol{y}^n - \boldsymbol{H}\mathcal{M}\boldsymbol{x}_e^{n-1}\right) \tag{2.9a}$$

$$\boldsymbol{P} = \boldsymbol{Q} - \boldsymbol{Q}\boldsymbol{H}^\top\left(\boldsymbol{H}\boldsymbol{Q}\boldsymbol{H}^\top + \boldsymbol{R}\right)^{-1}\boldsymbol{H}\boldsymbol{Q}. \tag{2.9b}$$

Note that the expression for $\boldsymbol{x}_e^{n,\mathrm{opt}}$ is similar to the KF update in eq. (2.6a), but it uses the covariance structure from the model error $\boldsymbol{Q}$ instead of the forecast $\boldsymbol{\Sigma}^{n,f}$. Even this formulation of the PF will degenerate for high-dimensional systems, see, e.g. Morzfeld et al. (2017).

The optimal proposal density filter can be modified such that all posterior ensemble members obtain a certain target weight w^n_{target}, and thus avoiding ensemble collapse and the need of resampling. Instead of drawing realisations from the proposal distribution directly, the IEWPF first samples $\boldsymbol{\xi}_e$ and $\boldsymbol{\zeta}_e$ from $\mathcal{N}(0, \boldsymbol{I}_{N_X})$ and next implicitly transforms the samples to a target distribution. This filter, introduced by Zhu et al. (2016) and modified by Skauvold et al. (2019), utilises a version of the optimal proposal density where $\boldsymbol{\xi}_e$ and $\boldsymbol{\zeta}_e$ are constructed to be perpendicular and scaled according to factors $\alpha_e^{1/2}$ for $e = 1, ..., N_e$ and $\beta^{1/2}$, respectively, before being transformed by $\boldsymbol{P}$ according to

$$\boldsymbol{x}_e^n = \boldsymbol{x}_e^{n,\mathrm{opt}} + \boldsymbol{P}^{1/2}\left(\alpha_e^{1/2}\boldsymbol{\xi}_e + \beta^{1/2}\boldsymbol{\zeta}_e\right). \tag{2.10}$$

Here, the constant β is a tuning parameter that influences the statistical quality of the results, whereas the α_e values are calculated implicitly for each ensemble member to ensure equal weights. To get an intuition of the idea behind IEWPF, we observe that eq. (2.9a) develops the state using $\mathcal{M}$ but with no model error. These unperturbed states are then used to get $\boldsymbol{x}_e^{n,\mathrm{opt}}$ by assimilating the observations. We then perturb $\boldsymbol{x}_e^{n,\mathrm{opt}}$ in (2.10), but instead of using the model error, which is sampled from $\mathcal{N}(0, \boldsymbol{Q})$, we sample perturbations from $\mathcal{N}(0, \alpha_e\boldsymbol{P})$ and $\mathcal{N}(0, \beta\boldsymbol{P})$ in such a way that we counteract the change of weights in the ensemble. Note that $\boldsymbol{P}$ is constructed from $\boldsymbol{Q}$ as seen in eq. (2.9b), so that these perturbations can be thought of as targeted sampling of the model error.

The tuning parameter β needs to be selected with care. A small value gives small spread of the ensemble that likely underestimates the variability, whereas a bigger β increases the spread. Holm et al. (2020, Appendix A) derived lower and upper bounds for this tuning parameter. In the subsequent experiments, we tune β manually, mainly by calibration of coverage probabilities as suggested in Skauvold et al. (2019). By experience it seems that β values around 0.5 are a good start. Albeit the choice of β is independent of the ensemble size, it is influenced by the dynamics of the problem. Hence, one can find a suitable choice of β for a specific kind of scenario and then keep it fixed in future experiments with similar characteristics.

It should be noted that in contrast to general PFs, the IEWPF requires that the model error is additive and from a Gaussian distribution. Furthermore, there are no guarantees on how the IEWPF performs, even when the ensemble size goes to infinity. Still, the performance tends to be very good in large-size systems. With $\beta = 0$, the implicit transform has a gap that leads to asymptotic bias (Skauvold et al., 2019), but this seems to be adjusted reasonably well by the second part having $\beta > 0$. The IEWPF has recently been shown to be applicable and efficient for assimilating point-based observations into a simplified ocean model based on the shallow water equations (Holm et al., 2020). Herein, this method represents a state-of-the-art PF and is investigated more thoroughly.

2.2 Ensemble Kalman filters in oceanographic applications

The EnKF (Evensen, 1994, 2009) is an ensemble-based version of the KF, given in eqs. (2.5) and (2.6). Originally presented as a data assimilation method for non-linear systems, it also solves the problem of having to store and propagate the $N_X \times N_X$ state covariance matrix $\boldsymbol{\Sigma}$.

In the ensemble representation from eq. (2.7), all weights are kept equal, and the state of each ensemble member is propagated by the model in eq. (2.1). The forecast state covariance is estimated from the ensemble, as

$$\widehat{\boldsymbol{\Sigma}}^{n,f} = \frac{1}{N_e - 1}\sum_{e=1}^{N_e}\left(\boldsymbol{x}_e^{n,f} - \overline{\boldsymbol{x}}^{n,f}\right)\left(\boldsymbol{x}_e^{n,f} - \overline{\boldsymbol{x}}^{n,f}\right)^\top, \tag{2.11}$$

where $\overline{\boldsymbol{x}}^{n,f}$ denotes the ensemble mean. The ensemble members are then updated along the same linear projection

$$\boldsymbol{x}_e^{n,a} = \boldsymbol{x}_e^{n,f} + \widehat{\boldsymbol{K}}\left(\boldsymbol{y}^n - \boldsymbol{H}\boldsymbol{x}_e^{n,f} - \boldsymbol{\epsilon}_e^n\right), \tag{2.12}$$

where the Kalman gain becomes $\widehat{\boldsymbol{K}} = \widehat{\boldsymbol{\Sigma}}^{n,f}\boldsymbol{H}^\top(\boldsymbol{H}\widehat{\boldsymbol{\Sigma}}^{n,f}\boldsymbol{H}^\top + \boldsymbol{R})^{-1}$. In eq. (2.12), the perturbation $\boldsymbol{\epsilon}_e^n \sim \mathcal{N}(0, \boldsymbol{R}^n)$ is added to adjust the variance in the solution ensemble, motivated by exact sampling in the linear Gaussian situation. This solution is therefore termed the stochastic EnKF (SEnKF, see (Burgers et al., 1998; Houtekamer and Mitchell, 1998; van Leeuwen, 2020)). The classical SEnKF in eq. (2.12) requires that we obtain and store the relevant covariances from the ensemble, and then factorize matrices to solve a linear system. For high-dimensional applications, this quickly becomes expensive, and it is therefore common to circumvent the covariance assembling (Evensen, 2003) or to use so-called deterministic square-root formulations instead (Whitaker and Hamill, 2002).

To avoid working in the state space, the ensemble transform Kalman filter (ETKF, Bishop et al. (2001)) reformulates eq. (2.12) via linear algebraic identities into a particular example of a deterministic square-root filter, which works in ensemble dimensions instead. Mathematically, let $\boldsymbol{X}^{n,f} = \left[\boldsymbol{x}_1^{n,f}, \ldots, \boldsymbol{x}_{N_e}^{n,f}\right]$ be the matrix of prior ensemble states, and let $\overline{\boldsymbol{X}}^{n,f}$ be a $N_X \times N_e$ matrix where all columns are $\overline{\boldsymbol{x}}^{n,f}$. The ETKF then works on the state perturbation matrix $\boldsymbol{X}_{\text{pert}}^{n,f} = \boldsymbol{X}^{n,f} - \overline{\boldsymbol{X}}^{n,f}$, and calculates the mean of the analysis ensemble

$$\overline{\boldsymbol{X}}^{n,a} = \overline{\boldsymbol{X}}^{n,f} + \boldsymbol{X}_{\text{pert}}^{n,f}\boldsymbol{A}(\boldsymbol{H}\boldsymbol{X}_{\text{pert}}^{n,f})^\top \boldsymbol{R}^{-1}\left(\boldsymbol{y}^n - \boldsymbol{H}\overline{\boldsymbol{x}}^{n,f}\right), \tag{2.13}$$

where

$$\boldsymbol{A} = \left((N_e - 1)\boldsymbol{I}_{N_e} + (\boldsymbol{H}\boldsymbol{X}_{\text{pert}}^{n,f})^\top \boldsymbol{R}^{-1}\boldsymbol{H}\boldsymbol{X}_{\text{pert}}^{n,f}\right)^{-1} \tag{2.14}$$

plays the role of the analysis covariance matrix. The ensemble members are then spread around $\overline{\boldsymbol{x}}^{n,a}$ according to

$$\boldsymbol{X}^{n,a} = \overline{\boldsymbol{X}}^{n,a} + \boldsymbol{X}_{\text{pert}}^{n,f}\left((N_e - 1)\boldsymbol{A}\right)^{1/2}, \tag{2.15}$$

where we use a singular-value decomposition to find the square-root of $\boldsymbol{A}$. The properties of the ETKF remain the same as for the EnKF and we refer to Li (2007) for further details on the transform.

The derivation of these methods assume a linear model, and asymptotic convergence results for increased ensemble size cannot be proved for non-linear cases. Still, the EnKF and its variants have been prevalent and successfully used in oceanographic applications (see, e.g. Carrassi et al. (2018)).

The error covariance matrix in this kind of filters is estimated from the ensemble and can lead to systematic underestimation. Typical approaches to counteract this are inflation or localisation. Anderson and Anderson (1999) introduced *covariance inflation* by a multiplicative factor to keep more variability in the ensemble, where several suggestions for the determination of an adaptive factor exist in literature, see, e.g. Desroziers et al. (2006); Anderson (2009); Sætrom and Omre (2013); Raanes et al. (2019). Similarly, additive inflation was presented by (Ott et al., 2004). However, Li et al. (2009) also point out that covariance inflation may not work appropriately in large complex models. Hence, we will mainly concentrate on localisation.

2.3 Sparse observations

The focus of this paper is on assimilating spatially sparse point observations. This naturally suggests to look closer on *localisation* in the filters. Although localisation is important for general applications, the sparse observations scenario considered here motivates one to study specific methods with good assimilation quality and algorithmic efficiency.

Localisation and sparse observation handling in the IEWPF The need for localisation in EnKF-based schemes arises from the spurious correlations introduced by the term $\widehat{\boldsymbol{\Sigma}}^{n,f}\boldsymbol{H}^\top$, which represents the estimated covariance terms between all state variables and all observations in eq. (2.12). As pointed out in Section 2.1, the optimal proposal distribution in eq. (2.9a) updates the state vector with a similar expression, but it uses the correlations in the model error, $\boldsymbol{Q}\boldsymbol{H}^\top$, rather than the empirical $\widehat{\boldsymbol{\Sigma}}^{n,f}\boldsymbol{H}^\top$. This means that the optimal proposal filter by design does not lead to spurious correlations. Still, the structure of $\boldsymbol{Q}$ of course influences the distribution, and in particular a local structure in $\boldsymbol{Q}$ that do not overlap between observation sites, entails updates in eq. (2.9a) that are local as well.

To show that the IEWPF updates in eqs. (2.9a) and (2.10) are local if $\boldsymbol{Q}$ is local, we consider the pattern of non-zero values in the matrix operations in the two equations. First, let us use r_Q to denote the radius in terms of number of grid cells that information is spread through the model error covariance matrix. This means that $\boldsymbol{Q}^{1/2}$ contains at most $(2r_Q+1)^2$ non-zero elements, whereas $\boldsymbol{Q} = \boldsymbol{Q}^{\top/2}\boldsymbol{Q}^{1/2}$ spreads the information twice as far, thus having at most $(4r_Q+1)^2$ non-zero elements. Second, we observe that eq. (2.9b) can be rewritten as

$$\boldsymbol{P} = \boldsymbol{Q}^{\top/2}\Big(\boldsymbol{I}_{N_X} - \underbrace{\boldsymbol{Q}^{1/2}\boldsymbol{H}^\top(\boldsymbol{H}\boldsymbol{Q}\boldsymbol{H}^\top + \boldsymbol{R})^{-1}\boldsymbol{H}\boldsymbol{Q}^{\top/2}}_{=:\boldsymbol{S}}\Big)\boldsymbol{Q}^{1/2}, \tag{2.16}$$

where we for convenience use $\boldsymbol{S}$ to represent the longest matrix expression. This means that $\boldsymbol{P}^{1/2} = (\boldsymbol{I}_{N_X} - \boldsymbol{S})^{1/2}\boldsymbol{Q}^{1/2}$, which is what we need in eq. (2.10).

In Table 1, we give upper bounds on the number of non-zero elements when stepping through the matrix operations in eqs. (2.9a) and (2.16). In the rightmost column, we assume that observations are sufficiently sparse so that both $\boldsymbol{H}\boldsymbol{Q}\boldsymbol{H}^\top$ and $\boldsymbol{R}$ are diagonal, whereas we make no such assumption in the second column from the right. We do however assume that $\boldsymbol{H}$ maps a subset of the state variables directly to observational space. If we now consider a single observation, meaning $N_Y = 1$ and scalar $(\boldsymbol{H}\boldsymbol{Q}\boldsymbol{H}^\top + \boldsymbol{R})^{-1}$, we see from Table 1 that the innovation in eq. (2.9a) is spread in the neighbourhood of the observation location within a radius of $2r_Q$ grid cells. Thus, $\boldsymbol{x}_e^{n,\text{opt}}$ differs from $\mathcal{M}\boldsymbol{x}_e^{n-1}$ only locally around the observation.

To see the resulting non-zero pattern for $\boldsymbol{S}$ in eq. (2.16), we realize that $\boldsymbol{H}\boldsymbol{Q}^{\top/2}$ consists of a single row from $Q^{\top/2}$. Furthermore, we have that the leftmost term $\boldsymbol{Q}^{1/2}\boldsymbol{H}^\top$ is the same as $(\boldsymbol{H}\boldsymbol{Q}^{\top/2})^\top$. Consequently, $\boldsymbol{S}$ is simply the (scaled) outer product of the column from $\boldsymbol{Q}^{1/2}$ corresponding to the observation, and therefore has the local correlation pattern in both its rows and columns, but zero in all rows and columns for which the observed state variable is not correlated with through $\boldsymbol{Q}^{1/2}$. This then means that $(\boldsymbol{I}_{N_X} - \boldsymbol{S})$ differs from the identity only locally to the observed state variable as well, which finally means that $\boldsymbol{P}^{1/2} = (\boldsymbol{I}_{N_X} - \boldsymbol{S})^{1/2}\boldsymbol{Q}^{1/2}$ differs from $\boldsymbol{Q}^{1/2}$ only locally to the observations as well.

It should be noted though, that the values of α_e and β depend on the innovation obtained from all observations in the domain. These parameters are therefore global parameters, but since they are scalars, they do not contribute to any change in the local correlation structures. Related discussions on how to utilize local covariance structures and sparse observations for efficient implementations of the IEWPF can be found in Holm (2020).

In addition to demonstrating the built-in localisation in the IEWPF, Table 1 shows how sensitive the IEWPF is to the structure of the model error covariance matrix $\boldsymbol{Q}$ for spreading observed information in the state space. In the extreme case of a diagonal $\boldsymbol{Q}$ (meaning $r_Q = 0$) all matrix operations will contain exactly N_Y non-zeros, and only the observed state variables will be affected by the data assimilation.

Localisation in the EnKF In a statistical sense, the spurious correlations in the EnKF are due to a poor Monte Carlo approximation of the true covariance matrix, see, e.g. Houtekamer and Zhang (2016). In the spatio-temporal physical model, information propagates at finite speed and long-distance correlations are unlikely to be significant. Prevailing techniques to counteract these artefacts are covariance or observation localisation as they are outlined in Sakov and Bertino (2011). Both of these exploit the physical distance between two points in space to reduce information propagation effects, and this has been demonstrated to work well in practice, see e.g. Soares et al. (2021). For many oceanographic applications, it is important that the geostrophic imbalance introduced by the localisation in the EnKF does not outweigh the natural imbalance - Greybush et al. (2011) provide a discussion and representative experiments to this issue.

For the ETKF, Ott et al. (2004) introduce an efficient localisation scheme and this is referred to as LETKF. Further developed implementations using parallelisation and observation batching exist, see e.g.

Table 1: Number of non-zero elements in the matrix operations used in IEWPF

Eq.	Matrix operations	Dims	# non-zeros for any $(\boldsymbol{HQH}^\top + \boldsymbol{R})^{-1}$	# non-zeros for diag $(\boldsymbol{HQH}^\top + \boldsymbol{R})^{-1}$
	$\boldsymbol{Q}^{1/2}$	$N_X \times N_X$	$\leq (2r_Q + 1)^2 N_X$	$\leftarrow$
	$\boldsymbol{Q}$	$N_X \times N_X$	$\leq (4r_Q + 1)^2 N_X$	$\leftarrow$
	$\boldsymbol{H}$	$N_Y \times N_X$	N_Y	$\leftarrow$
	$(\boldsymbol{HQH}^\top + \boldsymbol{R})^{-1}$	$N_Y \times N_Y$	$\leq {N_Y}^2$	N_Y
	$\boldsymbol{H}^\top(\boldsymbol{HQH}^\top + \boldsymbol{R})^{-1}$	$N_X \times N_Y$	$\leq {N_Y}^2$	N_Y
(2.9a)	$\boldsymbol{QH}^\top(\boldsymbol{HQH}^\top + \boldsymbol{R})^{-1}$	$N_X \times N_Y$	$\leq (4r_Q + 1)^2 {N_Y}^2$	$\leq (4r_Q + 1)^2 N_Y$
	$\boldsymbol{HQ}^{\top/2}$	$N_Y \times N_X$	$\leq (2r_Q + 1)^2 N_Y$	$\leftarrow$
	$(\boldsymbol{HQH}^\top + \boldsymbol{R})^{-1}\boldsymbol{HQ}^{\top/2}$	$N_Y \times N_X$	$\leq (2r_Q + 1)^2 {N_Y}^2$	$\leq (2r_Q + 1)^2 N_Y$
	$\boldsymbol{H}^\top(\boldsymbol{HQH}^\top + \boldsymbol{R})^{-1}\boldsymbol{HQ}^{\top/2}$	$N_X \times N_X$	$\leq (2r_Q + 1)^2 {N_Y}^2$	$\leq (2r_Q + 1)^2 N_Y$
$\boldsymbol{S}$ in (2.16)	$\boldsymbol{Q}^{1/2}\boldsymbol{H}^\top(\boldsymbol{HQH}^\top + \boldsymbol{R})^{-1}\boldsymbol{HQ}^{\top/2}$	$N_X \times N_X$	$\leq (2r_Q + 1)^4 {N_Y}^2$	$\leq (2r_Q + 1)^4 N_Y$

Hunt et al. (2007), and the LETKF variants are popular in numerical weather prediction, see e.g., Szunyogh et al. (2007), where for example global satellite data is common. In the LETKF, one loops over the state locations or sets of state locations in a batch area. Doing so, one updates state variables by means of the ETKF using only a specified set of local observations per batch.

Sparse observation handling in the ETKF In an oceanographic scenario with observations at only a few locations, we prefer to use covariance localisation (Houtekamer and Mitchell, 2001) to achieve computational control as we explain further down. One then defines local domains around each observation site only, where the size N_X^{loc} of a local area is significantly smaller than the full state space. For the choice of the radius of the resulting local domains, several approaches exist, see e.g. Kirchgessner et al. (2014), but we advocate using model-informed radii such as the model error range. We next assume that observations with non-overlapping local areas have negligible correlation, and they can be updated separately. Due to the motivating case with sparse observations, we expect to have few overlapping areas. The reduced dimension of the local area compared to the full state vector will make computations more efficient.

Still, with non-linear dynamical models, it is sometimes difficult to predict the possibly undesired effects of local approximations. Using sequential data integration, one can run through the data in multiple assimilation steps and in doing so one properly accounts for the correlations. In cases of overlapping local observation areas, we therefore recommend splitting the observations into observational batches $\mathcal{B}_b, b = 1, \ldots, B$ of assumed uncorrelated observations for serial processing as originally introduced in Houtekamer and Mitchell (1998). In our context, the batches at each step are constructed from far-apart observations. The local areas and the sequential processing give good control for handling correlations from sparse spatial observations. Nerger (2015) discusses how interactions of localisation and serial observation processing could destabilise the filter, but with reasonably set local areas and minimal correlation within a batch, this effect seems to be minuscule.

Figure 2.1(left) illustrates the definition of local areas around depicted observation sites. The figure further indicates the splitting into batches (middle and right display), with observations sites within a batch being sufficiently far apart from each other.

For the covariance localisation, we consider weighting vectors $\boldsymbol{w}_b$ and assume a tapering that assures $\boldsymbol{w}_b = 1$ at an observation site and $\boldsymbol{w}_b = 0$ outside the local areas. While veering away from an observation site, $\boldsymbol{w}$ should transit decreasingly monotone and smoothly from one to zero. An example of a kernel fulfilling those requirements locally in continuous space is the Gaspari-Cohn function (GC) introduced in Gaspari and Cohn (1999), which enjoys popularity in EnKF-localisation. We let $\boldsymbol{w}_{\text{loc},j} \in \mathbb{R}^{N_X^{\text{loc}}}$ be a properly scaled discretisation of the GC kernel around observation j, such that its support matches the radius of the

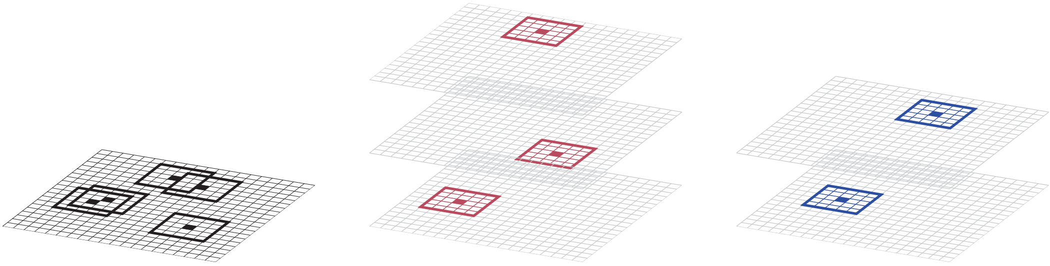

Figure 2.1: Schematic decomposition of the physical space (left panel) into local areas $N_X^{\mathrm{loc}} \ll N_X$ around observations, indicated by a filled grid cell, and the separation into two batches of uncorrelated observations (middle and right panel)

local area. With the same notation, the weighting is composed as

$$\boldsymbol{w}_b = \sum_{j \in \mathcal{B}_b} \boldsymbol{w}_{\mathrm{loc},j}. \tag{2.17}$$

For the observation batch from Figure 2.1, the weighting vectors $\boldsymbol{w}_1$ and $\boldsymbol{w}_2$ are illustrated in Figure 2.2 together with the contributions from $\boldsymbol{w}_{\mathrm{loc},1}, \ldots, \boldsymbol{w}_{\mathrm{loc},5}$.

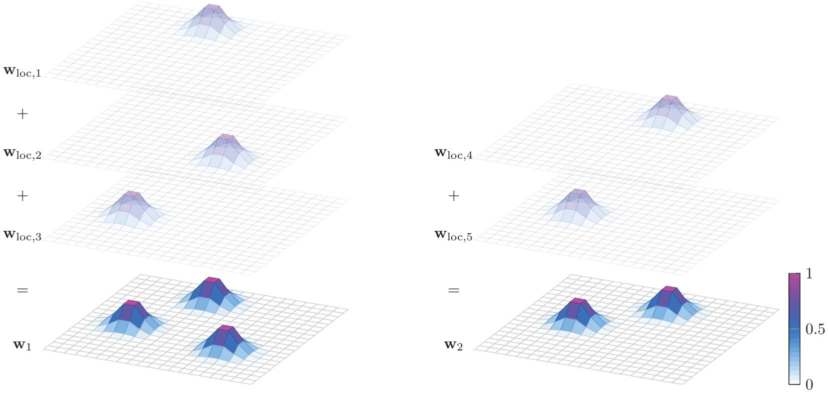

Figure 2.2: Schematic construction of the weighting $\boldsymbol{w}_b$ using the $\boldsymbol{w}_{\mathrm{loc},j}$ within the groups: For batch 1 and 2 from Figure 2.1, the weighting vectors $\boldsymbol{w}_1$ and $\boldsymbol{w}_2$ are built from the Gaspari-Cohn kernel around each observation with in the two groups. At the corresponding center, each $\boldsymbol{w}_{\mathrm{loc},j}$ equals one and decays towards the boundary of the local domains. By definition the supports are non-overlapping and the contributions are added up.

Within the recursion of batches $\mathcal{B}_b$, the local analysis states $\boldsymbol{x}^{n,a}(j) \in \mathbb{R}^{N_X^{\mathrm{loc}}}$ are calculated independently in each local area around the observation sites $j \in \mathcal{B}_b$, whereby the computational overhead in presence of sparse observations is implicitly controlled as the assimilation scheme operates in much smaller dimensions than N_X. Note that the processing of a batch can hence influence the ensemble that is used as the next forecast. The analyses only take values in their respective small local regions, but to avoid cumbersome notation for transformations, we abuse the same notation for their extension to the full state size $\boldsymbol{x}^{n,a}(j) \in \mathbb{R}^{N_X}$.

Because the ETKF constructs neither the covariance matrix nor the Kalman gain, we do not incorporate the weights directly into the Kalman update, but rather calculate the ETKF analysis state by eq. (2.15) and weight it with the forecast afterwards. (Recall that $\boldsymbol{x}^{n,a}(j)$ are the columns of $\boldsymbol{X}^{n,a}$ in eq. (2.15).) For the SEnKF, we see that this corresponds to tapering the Kalman gain and both approaches boil down to equivalent implementations. The weighting reads

$$\boldsymbol{x}_e^{n,a,b} = (1-\boldsymbol{w}_b)\boldsymbol{x}_e^{n,a,b-1} + \boldsymbol{w}_b \sum_{j\in\mathcal{B}_b} \boldsymbol{x}_e^{n,a}(j), \tag{2.18}$$

where $\boldsymbol{x}^{n,a,0} = \boldsymbol{x}^{n,f}$ and after the last batch, we set $\boldsymbol{x}^{n,a} = \boldsymbol{x}^{n,a,B}$ to obtain a final analysis state. For the global analysis state, this means that most analysis information is used near observation sites, whereas the forecast with its full spread is retained far away from data. The formulation of covariance location in the form of eq. (2.18) is furthermore convenient since the ETKF analysis scheme can be used as black-box without interference of the localisation weights. From a principled statistical perspective, one could process each individual observation in a serial manner, but the collection in prescribed batches reduces iterations. In doing so, one assimilates the spatial data recursively, similar to the assimilation over time, albeit without the dynamical state evolution because all updates happen at the time when the data gets available. For computational efficiency one again imposes some kind of local routine, and in practice this may rely on GC tapering of the matrices involved. This is commonly done in implementations of Kriging, or in applications with sequential uncertainty reduction, where the analysis can depend on the choice of conditioning order, see, e.g. Nussbaumer et al. (2018).

Complementary to inflation as mentioned in Section 2.2, Zhang et al. (2004) present relaxation-to-prior to counteract overfitting. Introducing a scaling parameter $\phi \in [0,1]$, the weighting vector can be constructed with neatly integrated relaxation as

$$\boldsymbol{w}_b^{\text{relax}} = \sum_{j\in\mathcal{B}_b} \phi\ \boldsymbol{w}_{\text{loc},j}. \tag{2.19}$$

Here, $\phi = 0$ represents a pure Monte-Carlo simulation while $\phi = 1$ is the previously presented scheme without relaxation.

Algorithm 1 summarizes the ETKF with covariance localisation as we will use it later on. We will refer to it as "SparseObsETKF" in order to avoid mixing up with the LETKF. This implementation help us to keep good control of correlations as well as computational overhead in the presence of sparse observations, and it provides a convenient integration of tapering and relaxation.

Algorithm 1 Analysis scheme with localisation for sparse observations (SparseObsETKF)

```
Given $\boldsymbol{X}^{n,f}$. Parameters: localisation radius and relaxation $\phi$
Set $\boldsymbol{X}^{n,a,0} = \boldsymbol{X}^{n,f}$
for $b = 1,\dots,B$ do
    Allocate $\boldsymbol{w}_b^{\text{relax}}$                                              ▷ $N_X$
    for $j \in \mathcal{B}_b$ do
        Calculate local $\boldsymbol{X}^{n,a}(j)$ using the ETKF where $\boldsymbol{X}^{n,a,b-1}$ is the forecast    ▷ $N_X^{\text{loc}}$
        $\boldsymbol{w}_b^{\text{relax}}$ += $\phi\boldsymbol{w}_{\text{loc},j}$
    end for
    $\boldsymbol{X}^{n,a,b} = (1-\boldsymbol{w}_b^{\text{relax}})\boldsymbol{X}^{n,a,b-1} + \boldsymbol{w}_b^{\text{relax}}\sum_{j\in\mathcal{B}_b}\boldsymbol{X}^{n,a}(j)$    ▷ $N_X$
end for
$\boldsymbol{X}^{n,a} = \boldsymbol{X}^{n,a,B}$
```

3 Comparison against the Analytical Kalman Filter in a Linear Gaussian Advection Diffusion Model

In this section, we examine a linear Gaussian spatio-temporal model. As mentioned in Section 2, this means that the analytic KF in eqs. (2.5) and (2.6) defines the optimal solution. Ensemble-based approximations and localisation effects of the different filtering techniques from Section 2 can be verified against the KF.

3.1 Advection diffusion model

Inspired by Sigrist et al. (2015), we consider a stochastic advection diffusion equation for state c given by

$$\frac{\partial c(t, \boldsymbol{s})}{\partial t} = \nabla \cdot d \nabla c(t, \boldsymbol{s}) - \boldsymbol{v}_t \cdot \nabla c(t, \boldsymbol{s}) + \zeta c(t, \boldsymbol{s}) + W(t, \boldsymbol{s}). \tag{3.1}$$

The model's parameters are $d = 0.25$ for the diffusion, $\boldsymbol{v} = (1.0, 0.1)^\top$ for the advection, and $\zeta = -0.0001$ for the damping. We assume the stochastic error process W has uncorrelated elements over time but smooth dependent spatial components at each time, and that eq. (3.1) holds for one sampled path (realisation) of W. We consider a rectangular spatial domain $[0, 5] \times [0, 3]$ with periodic boundary conditions, and c will be initialised at time $t = 0$ as a Gaussian random field.

Equation (3.1) can be used to represent for instance marine pollution dynamics (Foss et al., 2021), where the goal is to predict the concentration $c = c(t, \boldsymbol{s})$ of a contaminant over time and space in the ocean. In that case, the advection parameter $\boldsymbol{v}$ would typically come from a full ocean model if vertical currents are ignored.

In the discretised setting, the spatial domain is covered by a uniform Cartesian grid with center points $(\boldsymbol{s}_i)_{i=1}^{N_s}$ in quadratic cells of size 0.1×0.1. The state vector $\boldsymbol{x}^n$ collects all concentrations $c(t^n, \boldsymbol{s}_i)$ at regular time steps t^n. The initial state is represented by $\boldsymbol{x}^0 \sim \mathcal{N}(\boldsymbol{\mu}^0, \boldsymbol{\Sigma}^0)$ with mean vector $\boldsymbol{\mu}^0$ and covariance matrix $\boldsymbol{\Sigma}^0$ having Matérn-type

$$\boldsymbol{\Sigma}^0_{k,l} = \sigma^2 (1 + \psi D_{k,l}) \exp(-\psi D_{k,l}),$$

where $\sigma = 0.5$ is the standard deviation (assumed constant at all locations) and $\psi = 3.5$ is the Matérn correlation decay parameter, and $D_{k,l}$ is the distance between $\boldsymbol{s}_k$ and $\boldsymbol{s}_l$. The mean $\boldsymbol{\mu}^0$ equals 10 in the north-east with higher bell-shaped concentration values in the south-west, see Figure 3.2 (left).

For the numerical solution of the SPDE in eq. (3.1), a temporal forward and spatial central finite-difference scheme is employed such that the model resembles eq. (2.1) with the linear operator $\mathcal{M} = \boldsymbol{M}$. With periodic boundary conditions the low-concentration area leaves the domain on the east boundary and enters from the west. The model error $\boldsymbol{\nu}$ is again represented by a Gaussian random field with a covariance matrix $\boldsymbol{Q}$ of a similar Matérn-type. A smaller standard deviation $\sigma = 0.125$ is used, and larger correlation decay parameter $\psi = 7.0$ leading to model noise with smaller correlation.

3.2 Experiment design and analytic solution

A single realisation of the advection diffusion generated by the forward model is used to retrieve observations for the filtering, see Figure 3.1. It is simulated for 250 time steps with $\Delta t = 0.01$ on a grid of size 50×30. The simulated process is observed at $t^n = 25n, n = 1, \ldots, 10$ at 15 grid cells marked red in Figure 3.1. These direct state observations are made with a small observation error $\boldsymbol{\epsilon}^n \sim \mathcal{N}(0, r^2 \boldsymbol{I})$, $r = 0.1$.

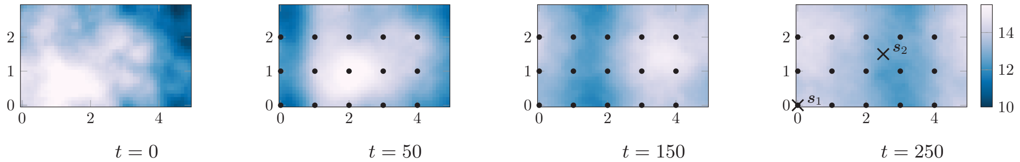

Figure 3.1: The "truth" realisation of the stochastic process at the initialisation and selected observation times with black dots marking the observation sites and black crosses signifying two selected locations of interest.

The KF reference solution is depicted for a selection of time steps in Figure 3.2. As for the truth in Figure 3.1, the filtering mean (Figure 3.2, top) shows an east north-east movement of the concentrations as expected from the advection term. The standard deviations (Figure 3.2, bottom) are clearly reduced by the data assimilation, especially around the observation sites and in the advection direction. With time, however, the accuracy of the solution converges as the corrections from doing data assimilation are balanced out by the dynamic model errors.

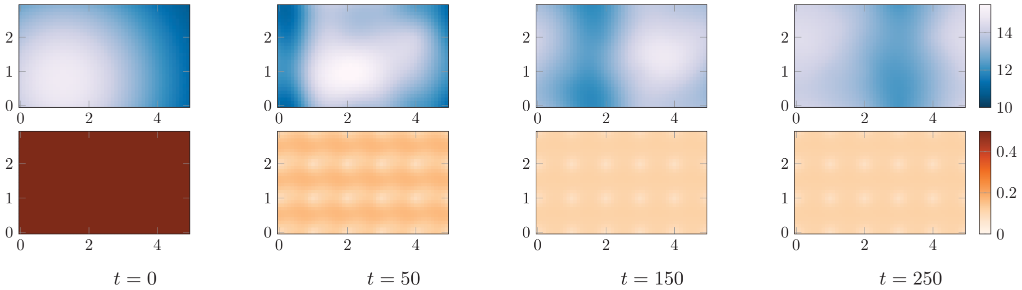

Figure 3.2: For the same times as in Figure 3.1, the resulting analysis mean (upper row) and standard deviation (lower row) of the KF.

3.3 Numerical results and evaluation metrics

We now solve this concentration advection diffusion problem using the ensemble-based methods IEWPF, ETKF, and SparseObsETKF from Section 2. The parameter β emerging in the IEWPF is tuned manually and set to 0.55, and this will be discussed further in relation to some of the results. We set the localisation radius of the SparseObsETKF equal to the correlation range of the model error, which leads to four observational batches. First, we do not use any relaxation in the perfect linear model, as suggested by Raanes et al. (2019). The performance of ensemble-based solutions are opposed to the KF reference solution. We use a set of metrics to evaluate different statistical aspects of the data assimilation methods.

Root-mean-squared error The ensemble mean $\overline{\boldsymbol{x}}^a$ is compared with the KF mean $\boldsymbol{\mu}^a$. Here, we consider the state at $t = 250$ after assimilating all available observations. The error in the mean at each position is then the vector $\mathbf{err}_{\text{mean}}^{\text{KF}} = (\boldsymbol{\mu}^a - \overline{\boldsymbol{x}}^a)$. As a scalar metric to compute the behaviour over all grid cells, we use the root-mean-squared error (RMSE)

$$\text{RMSE} = \|\mathbf{err}_{\text{mean}}^{\text{KF}}\|_2. \tag{3.2}$$

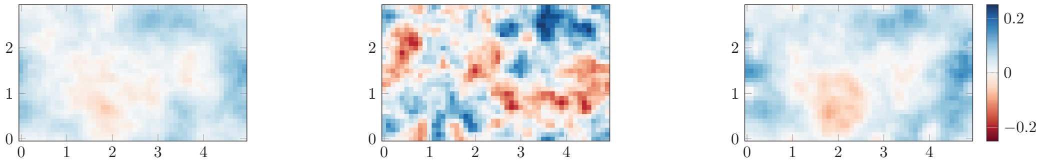

(a) IEWPF [1.76] (b) ETKF [3.35] (c) SparseObsETKF [2.26]

Figure 3.3: Mean error $\mathbf{err}_{\text{mean}}^{\text{KF}}$ at $t = 250$ for assimilation experiments with $N_e = 50$ ensemble members. RMSE is given in the bracket for each specified method.

Figure 3.3 shows $\mathbf{err}_{\text{mean}}$ at each grid cell for a single data assimilation experiment with $N_e = 50$ ensemble members for each method. The RMSEs are the caption brackets. All three ensemble-based data assimilation methods lead to means that closely resemble the KF reference solution. The mean error is in general low and smoothly distributed for both IEWPF and SparseObsETKF, whereas the errors of EKTF are somewhat bigger. Based on RMSE, IEWPF performs slightly better than SparseObsETKF, whereas the RMSE for ETKF is about twice that of IEWPF.

To deduce reliable conclusions beyond one data set and single ensembles, we repeat the data assimilation experiment multiple times for several independently generated true states. In Table 2, we report averaged results for 20 replicate synthetic truths and five ensemble-based data assimilation experiments each. For this relatively small ensemble size of $N_e = 50$, the localisation in the SparseObsETKF halves the RMSE compared to the standard ETKF, and the RMSE of the IEWPF lies in the middle of the ETKF with and without localisation.

Frobenius covariance difference We contrast the empirical covariance estimates $\widehat{\boldsymbol{\Sigma}}^a$ in eq. (2.11) with the KF reference $\boldsymbol{\Sigma}^a$. We compute the Frobenius covariance difference (FCD) to compare these covariance matrices:

$$\mathrm{FCD} = \|\boldsymbol{\Sigma}^a - \widehat{\boldsymbol{\Sigma}}^a\|_{\mathrm{F}},$$

where $\|\cdot\|_{\mathrm{F}}$ denotes the Frobenius norm (elementwise sum). Averaged results for the FCD over replicate experiments are presented in Table 2 using $N_e = 50$. Here, we see that the FCD for IEWPF and SparseObsETKF are very similar for all cases. The covariance approximations show smaller errors for the ETKF solution than for the other methods. At a single step, the ETKF approximation to the covariance is unbiased, while the other methods have no such guarantee. Still, it is not obvious that the ETKF performs better after many data assimilation steps. Also, when we test the entries close and far from the diagonal of the covariance matrix, we cannot see any other behaviour in the results.

Integrated quadratic distance We next study a metric for the marginal distribution mismatch of discrete ensemble-based distribution approximations to the Gaussian KF reference solution. The reference cumulative distribution function (CDF) of the KF is denoted F^a. The empirical cumulative distribution function (ECDF) of the ensemble-based solutions are denoted $\widehat{F}^a$.

In the analysis two specific locations shown in the far right panel of Figure 3.1 are studied based on their different characteristics: $\boldsymbol{s}_1 = (0,0)$ is an observation site and $\boldsymbol{s}_2 = (2.5, 1.5)$ is as far away from observation data as possible.

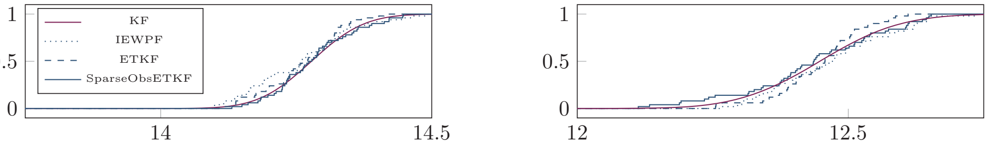

(a) CDF and ECDFs at $\boldsymbol{s}_1$ (b) CDF and ECDFs at $\boldsymbol{s}_2$

Figure 3.4: For two distinct positions, $\boldsymbol{s}_1$ as observation site and $\boldsymbol{s}_2$ far away from observation sites, at $t = 250$ the CDF of the Kalman filter is compared to the ECDFs of IEWPF [0.0242, 0.0238], ETKF [0.0164, 0.0254], and SparseObsETKF [0.0093, 0.0117], respectively, with $N_e = 50$. In brackets, the integrated quadratic difference d_{IQ} for $\boldsymbol{s}_1$ and $\boldsymbol{s}_2$, respectively.

In Figure 3.4, the CDF of the KF is depicted in comparison with the ECDFs of IEWPF, SparseObsETKF, and ETKF at the two different locations for a small ensemble size. First, since the scales of the x-axis in both displays are the same, it becomes obvious that the standard deviation at an observation site is much smaller than at an unobserved location. Next, we see that the different filtering methods differ in quality when compared to the analytic solution. For the observation site $\boldsymbol{s}_1$, there is no clear qualitative difference, but at $\boldsymbol{s}_2$ one may already identify a slight divergence in ETKF's ECDF, whereas SparseObsETKF and IEWPF still approximate the reference CDF quite well.

The tuning parameter β steers the spread in the analysis ensemble of the IEWPF and among the presented evaluation metrics the ECDF reveals the scale the best. We used it to optimise the filtering distribution manually and found 0.55 as best choice. For smaller values, the ECDF gets too sharp and for higher values the spread gets too large. Similarly, the variance in the SparseObsETKF-ensemble usually increases as the relaxation parameter ϕ decreases. When using $\phi < 1$ we observed that the spread in the ensemble becomes too big compared to the CDF and the best match is achieved for $\phi = 1$.

Thorarinsdottir et al. (2013) suggest a proper divergence function to compare marginal CDFs, condensing the error into a scalar number. The integrated quadratic difference is defined by

$$d_{\mathrm{IQ}} = \int \left(F^a - \widehat{F}^a\right)^2 \mathrm{d}x,$$

where the quadratic error is integrated over the sample space of the variable. Errors captured in d_{IQ} can originate from either a lack of Gaussianity, or a wrong scaling or a bias, or a combination.

Table 2 shows averaged results for d_{IQ} at $\boldsymbol{s}_1$ and $\boldsymbol{s}_2$ for the three ensemble methods. IEWPF and ETKF produce similar results, while SparseObsETKF clearly gives the best results. The reason is twofold: First, the IEWPF and ETKF update the entire field at each data assimilation time, even at locations like $\boldsymbol{s}_2$ that are far away. With the limited ensemble size, this is likely to induce some undesired bias and variability far from data. Second, the SparseObsETKF is rather accurate near the observations sites, like the other filters, and because the advection and diffusion are known, the local updating propagates reasonably over time to the far location $\boldsymbol{s}_2$.

Probability coverage level Based on the mean and variance of the ensemble-based solutions, we can check how often a prediction interval covers the true realisation. For the KF reference, we will have near nominal coverage because the truth is simulated from the same model. Coverage probabilities (CPs) of the analysis after the first observation time are

$$CP^1_{1.64} := P\left(\boldsymbol{x}^1_{\mathrm{true}} \in \left[\boldsymbol{\mu}^{1,a} \pm 1.64\boldsymbol{\sigma}^{1,a}\right]\right) \approx 0.90.$$

This means that the probability that the truth is covered in the interval of 1.64 standard deviations from the mean is 90%. For all methods, we use replicated synthetic truths, and estimate the CPs.

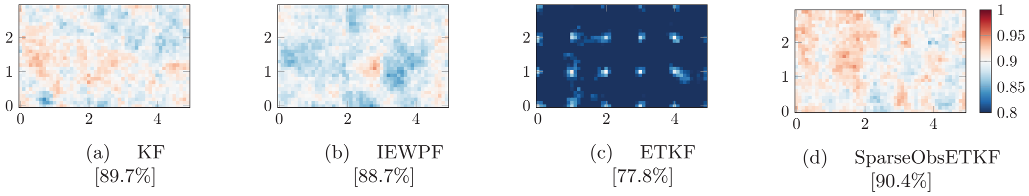

(a) KF [89.7%] (b) IEWPF [88.7%] (c) ETKF [77.8%] (d) SparseObsETKF [90.4%]

Figure 3.5: Estimated $CP^1_{1.64}$ using 500 replication experiments for the KF and the ensemble-based methods with $N_e = 50$. The brackets show the averaged estimated coverage probabilities. The color scale is centered at the target probability of 90%.

Figure 3.5 shows the estimates of the CPs averaged over 500 runs. The KF results cover the nominal 90% very well, with a variability as expected from 500 replicates. Even though that the KF is analytic, the truths are generated stochastically and we see the Monte Carlo error here. The IEWPF and the SparseObsETKF also give very good estimates even though the ensemble size of 50 members is low, and there are no visible structures around observation sites. In contrast, the ETKF without localisation suffers from strong under-coverage in this experiment. The CPs are around 0.9 near observation sites but fall to lower levels, which are outside the truncation interval of the plot, away from these.

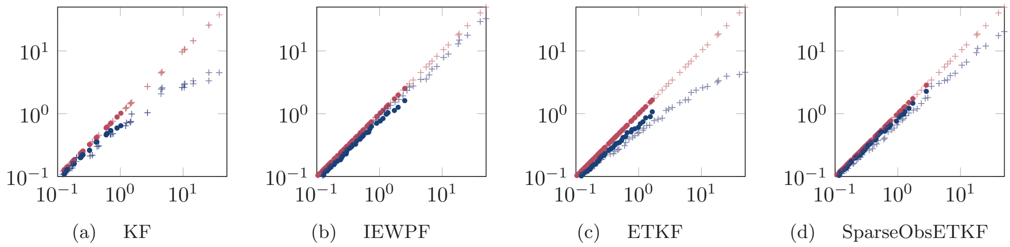

(a) KF (b) IEWPF (c) ETKF (d) SparseObsETKF

Figure 3.6: Eigenvalue update in the very first (crosses) and very last (dots) data assimilation step. Prior-vs-prior in red, prior-vs-posterior in blue.

Eigenvalues analysis An eigendecomposition of the covariance matrix yields eigenvalues representing the variability among orthogonal axes of linear combinations of state variables. The largest (first) eigenvalue is the variance in the direction of the first eigenvector, and for a Gaussian distribution this represents the largest half-axis in the ellipsoid defined via the quadratic form. Further, for a Gaussian distribution, the entropy (disorder) is defined via the log-determinant of the covariance matrix which is the sum of the log-eigenvalues. By studying the eigenvalues of the covariance matrices of the different data assimilation methods, we hence gain insight in the variability reduction and the disorder of the distributions. Since it does not make sense to average eigenvalues over multiple realisation, we leave the spectral analysis to a qualitative view with cross-plots of eigenvalues for the different methods.

Figure 3.6 shows cross-plots of the covariance matrix eigenvalues of forecast (first axis) and assimilated (second axis). In all displays, the crosses represent the first data assimilation step while the dots are at the last data assimilation step. For the KF, eigenvalues are computed directly from the covariance matrix and for the ETKF variants this is the eigenvalues of the estimated covariance matrix in eq. (2.11). In the case of the IEWPF, the prior ensemble is without model error and hence we perturb the prior before plotting.

In Figure 3.6, the forecast-vs-forecast points (red) lie on a straight line, but we still notice that all the red dots are closer to the origin than some of the crosses. Hence, the eigenvalues are clearly smaller at the last step, indicating that the data assimilation over time gives smaller entropy. Going from forecast (red) to assimilated (blue), the eigenvalues of the covariance matrix are reduced. Taking the KF as a benchmark, this reduction is particularly large for the biggest eigenvalues, indicating the updating is not only local but also shrinks the variability of dominating linear combinations and the entropy of the distribution. At the first step (crosses), the ETKF updating appears very similar to that of the KF. At the last step, the eigenvalues of the ETKF are larger and not reduced quite like for the KF. This indicates that even though the ETKF undercovers the distribution (Figure 3.5), there is not quite sufficient reduction in the largest eigenvalues. Both IEWPF and SparseObsETKF get smaller reduction in eigenvalues than the KF. At the first data assimilation step the reduction is larger for SparseObsETKF than for the IEWPF, while the IEWPF has more reduction at the last data assimilation step.

Spatial connectivity While the previous metrics have considered the marginal solution at one time step only, the correlation between different time steps and between different spatial positions gives further insight into the statistical quality of the filtering methods.

Given data up to time t^{n-1}, the correlation between the concentration at $\boldsymbol{s}_k$ at $t^{n-1} = 225$ and $\boldsymbol{s}_l$ at t^n can then be calculated from the KF results via

$$\mathbb{C}\mathrm{orr}\left(\boldsymbol{x}_k^{n-1,a}, \boldsymbol{x}_l^{n,f}\right) = \frac{\mathbb{C}\mathrm{ov}\left(\boldsymbol{x}_k^{n-1,a}, \boldsymbol{x}_l^{n,f}\right)}{\sigma_k^{a,n-1}\sigma_l^{f,n}} = \frac{\boldsymbol{M}\boldsymbol{\Sigma}_{k,l}^{a,n-1}}{\sqrt{\boldsymbol{\Sigma}_{k,k}^{a,n-1}}\sqrt{\boldsymbol{\Sigma}_{l,l}^{f,n}}}. \tag{3.3}$$

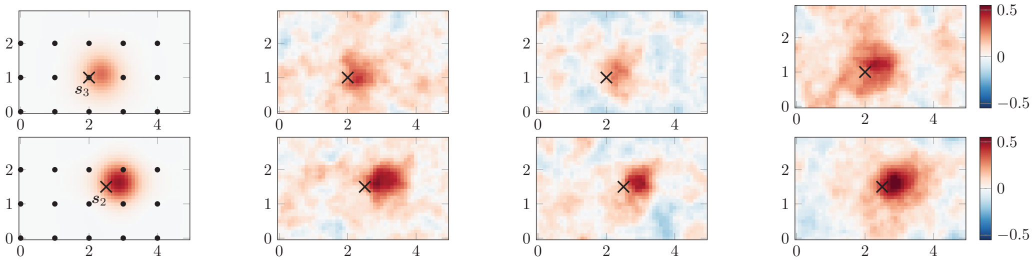

(a) KF (b) IEWPF $[2.73, 2.71]$ (c) ETKF $[2.32, 2.64]$ (d) SparseObsETKF $[3.86, 3.13]$

Figure 3.7: Correlations $\mathbb{C}\text{orr}\left(\boldsymbol{x}_k^9, \boldsymbol{x}_l^{10}\right)$ and $\widehat{\mathbb{C}\text{orr}}\left(\boldsymbol{x}_k^9, \boldsymbol{x}_l^{10}\right)$ between fixed locations $\boldsymbol{s}_k$ and all other grid points in the domain $\boldsymbol{s}_l$, for $k = 3$ in the upper and $k = 2$ in the lower row, respectively. The ensemble-based methods use $N_e = 250$ ensemble members, and the respective CE estimates are given in the square brackets.

Similarly, we can estimate these correlations from the ensemble-based methods by

$$\widehat{\mathbb{C}\text{orr}}\left(\boldsymbol{x}_k^{n-1,a}, \boldsymbol{x}_l^{n,f}\right) = \frac{1}{N_e - 1} \frac{1}{\hat{\sigma}_k^{n-1,a} \hat{\sigma}_l^{n,f}} \sum_{e=1}^{N_e} (\boldsymbol{x}_{e,k}^{n-1,a} - \overline{\boldsymbol{x}}_k^{n-1,a})(\boldsymbol{x}_{e,l}^{n,f} - \overline{\boldsymbol{x}}_l^{n,f}).$$

In Figure 3.7, we show the correlation fields of the state between a reference grid cell at $t^9 = 225$ and all other grid cells at $t^{10} = 250$. As reference locations $\boldsymbol{s}_k$, we consider $\boldsymbol{s}_2$ positioned far away from any observations in the top row, and $\boldsymbol{s}_3$ at an observation site in the middle of the domain displayed in the lower row. First, from the KF solution (left), we recognise the advection field in the model that transports information towards east-north-east from both locations, as well as the diffusion causing the correlation to have longer range than the model error correlation radius. Second, the maximal correlation to the reference point is higher when $\boldsymbol{s}_k$ is not an observation site. In spatial statistics, conditioning on data breaks up some of the prior correlations. Since most of the update from the data assimilation occurs near the observation locations, the conditional correlation tends to be smaller in the proximity of data. At locations that are far from observations, more of the prior correlation remains.

In the three rightmost columns of Figure 3.7, we see the correlations estimated with the three ensemble-based methods using an ensemble with $N_e = 250$ members. We see that all methods capture a similar correlation structure with respect to the advection and diffusion, and the relative balance between prior model and information from the observation. With $N_e = 250$, results are less smooth than the KF solution. In the upper scenario, the area of high analytical correlations becomes less apparent among background noise, while in the lower scenario the respective regions are easier to identify in all methods.

The spatial error in the approximation of correlation between two consecutive model steps for the reference location $\boldsymbol{s}_k$ is evaluated collectively across all grid cells as

$$\text{CE}(\boldsymbol{s}_k)^2 = \sum_{l=1}^{N_s} \left| \mathbb{C}\text{orr}\left(\boldsymbol{x}_k^{n-1,a}, \boldsymbol{x}_l^{n,f}\right) - \widehat{\mathbb{C}\text{orr}}\left(\boldsymbol{x}_k^{n-1,a}, \boldsymbol{x}_l^{n,f}\right) \right|^2. \tag{3.4}$$

The CE for the specific data assimilation run shown in Figure 3.7 are given in square brackets in the figure captions. These results for a single run with $N_e = 250$ already reveal that the contribution to CE can come from multiple sources, such as over- or under-estimation of the actual correlations and from spurious correlations. The final CE does not qualitatively expose which of the error sources are present to which extent, but it quantifies how well the analytical structure is approximated. The chosen $\mathbb{C}\text{orr}$ and $\widehat{\mathbb{C}\text{orr}}$ suggest that spurious correlations are a present error source in all methods, but IEWPF and SparseObsETKF tend to overestimate the high correlations. Meanwhile, ETKF underestimates the correlations, thus leading to a smaller CE.

3.4 Sensitivity to localisation

In the IEWPF the localisation properties are steered by the structure of the model error covariance $\boldsymbol{Q}$ and in the SparseObsETKF by the definition of the localisation radius, which we again defined according to the correlation range of $\boldsymbol{Q}$, see Section 2.3. In the rest of the section those choices are hold fixed, but here we showcase their influence. To do so, we consider four different ψ for the model error covariance matrix, while keeping everything else unaltered, i.e. the standard derivation and the IEWPF tuning parameter β. Analogously, we vary the localisation radius in the SparseObsETKF. The parameter $\psi = 3.0$ corresponds to no localisation and $\psi = 5.0, 11.0$ represent roughly a doubling and halving of the localisation radius, respectively. Importantly, it should be noted that the GC and the Matérn-type covariance kernel decay with different rates such that the results are not one-to-one comparable, but we can still record trends within each method.

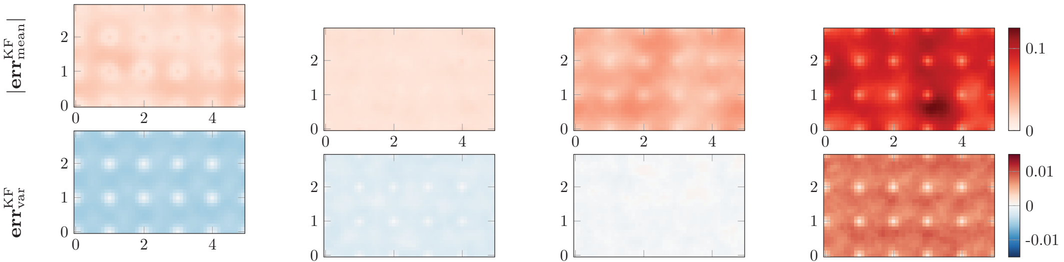

(a) Extra wide localisation (b) Wide localisation (c) Default localisation (d) Slim localisation

Figure 3.8: Different localisation parametrisations for the IEWPF. Averaged results over 20 truth realisations and 5 ensemble initialisation each.

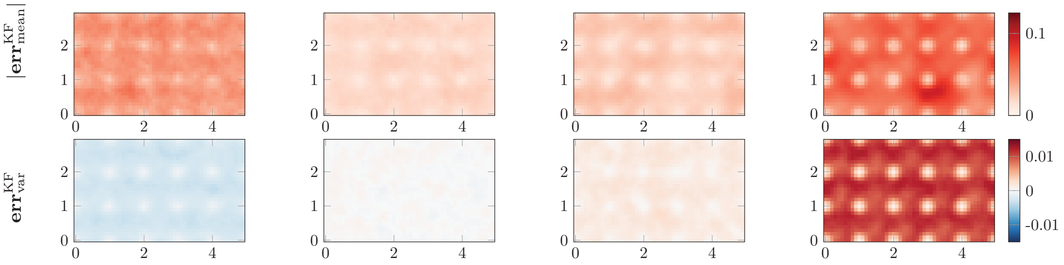

(a) No localisation (b) Wide localisation (c) Default localisation (d) Slim localisation

Figure 3.9: Different localisation parametrisations for the SparseObsETKF. Averaged results over 20 truth realisations and 5 ensemble initialisation each.

Figure 3.8 and Figure 3.9 allow to get an impression of the RMSE together with spatial effects. Since the localisation is in-build into the IWEPF, one has to be careful with the interpretation of the left-most

Table 2: Metrics for marginal distribution averaged over 20 synthetic truths and 5 ensemble realisations, each with $N_e = 50$. Standard deviations are given in brackets.

	RMSE	FCD	d_{IQ} at $\boldsymbol{s}_1$	d_{IQ} at $\boldsymbol{s}_2$
MC	8.27 [2.88]	47.0 [8.35]	12.8E-02	13.5E-02
IEWPF	1.67 [0.43]	2.77 [0.14]	2.51E-02	2.58E-02
ETKF	2.14 [0.40]	2.14 [0.04]	2.57E-02	2.86E-02
SparseObsETKF	1.15 [0.24]	2.79 [0.15]	1.29E-02	1.68E-02

row (a). Nevertheless, there are clear unintended artefacts in mean and variance errors. Even though the mean for $\psi = 5.0$ in row (b) is very well calibrated in the entire field, the variance is slightly underestimated and the error shows structures around observation locations. Note that an increase of β may counteract the underestimation. For the standard IEWPF, this is the opposite way around, here the error in the variances is minuscules, but the mean is not eqully well calibrated. The IEWPF with reduced localisation radius performs poorly when further away from observation locations. The ETKF without localisation underestimates the variance of the KF. The SparseObsETKF with a localisation radius that spans the full y-extent of the domain (row (b)) performs for mean and variance estimation slightly better than the parametrisation as we have chosen in the rest of the section. We remind that the usually used localisation yields a computational advantage due to reduced analysis dimensions. Again the smallest localisation parametrisation fails to assimilate the entire domain.

We note that the localisation parametrisation as used in the rest of the section work reasonably well. Nevertheless we notice that there is potential to fine-tune both methods further, but in the interest of a limited number of tuning parameters we continue with the native parameters.

3.5 Discussion of evaluation metrics

The set of comparative metrics from the previous subsection has given us a collection of metrics that quantify some statistical qualities of the ensemble-based data assimilation methods in reference to the analytical KF solution.

Table 2 shows the statistically averaged results for these performance scores at $t = 250$. These results are obtained across five data assimilation runs for 20 different synthetic truths and are therefore more reliable than the single realisations demonstrated in Figures 3.3, 3.4 and 3.7. We have here used $N_e = 50$ ensemble members for each run. In addition to comparing the data assimilation methods against each other, we have also included the results using pure Monte Carlo simulations without observations (top row). These serve to demonstrate the worst-case scenario for each metric, and we see how all three data assimilation methods clearly outperform this, as expected. In the experiments, we have observed that the IEWPF takes several assimilation steps until it is sufficiently calibrated, what is respected by the the choice of t here such that the comparison stays fair, see Section 4 for details.

Based on the results in Table 2 there is no method that clearly dominate on all individual criteria. For RMSE, it seems that SparseObsETKF is much better than ETKF, but this is not as clear when considering FCD, where ETKF scores best. Maybe more surprising, SparseObsETKF is significantly better than ETKF when measuring the error in the ECDF at $\boldsymbol{s}_2$ far from the observation, but not at $\boldsymbol{s}_1$ at an observation site. A plausible explanation is that when updating the state far from an observation, all covariances are relatively weak, which means that spurious correlations more easily dominate data assimilation. With localisation, we ensure that only the most relevant small correlations are considered, thus improving the result. This effect will then be less at an observation site as the most important correlations are stronger. IEWPF gets all metrics between ETKF and SparseObsETKF. We observe that worse FCD has no influence on the d_{IQ} at the considered positions.

Effects of ensemble size In Figure 3.10, we study how different ensemble sizes influence RMSE, d_{IQ}, and correlations for the three ensemble-based methods. We use ensemble sizes $N_e \in \{25, 50, 100, 250, 1000, 5000\}$,

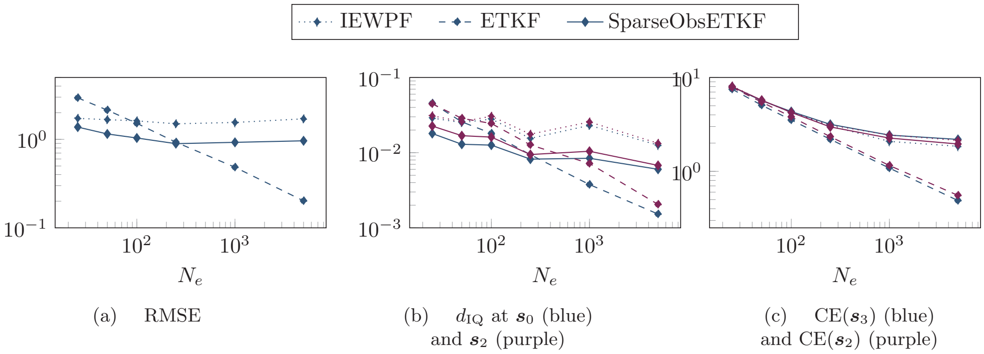

(a) RMSE

(b) d_{IQ} at $\boldsymbol{s}_0$ (blue) and $\boldsymbol{s}_2$ (purple)

(c) $\mathrm{CE}(\boldsymbol{s}_3)$ (blue) and $\mathrm{CE}(\boldsymbol{s}_2)$ (purple)

Figure 3.10: Evolution of the comparison measures in depends of the ensemble size N_e.

and the results are averaged across multiple experiments for each of these sizes. In general, we expect that increased ensemble size leads to more accurate statistical estimates and thereby better results. This is clearly the case for ETKF for all metrics, and SparseObsETKF shows the same trend, but not as strongly. We see that SparseObsETKF outperforms ETKF with respect to RMSE and d_{IQ} for small ensemble sizes, but ETKF is better with large ensembles as the performance of SparseObsETKF stagnates for $N_e > 250$. SparseObsETKF improves less than ETKF with larger ensembles because it ignores correlations, and this gives bias in the analysis. The IEWPF yields results between ETKF and SparseObsETKF for small sample sizes, but there is slower convergence as the ensemble size increases. Unlike ETKF, which converges to the true Gaussian distribution in this case, there is no such guarantee for the IEWPF. Since the second stage perturbation step of the IEWPF is designed to reduce a systematic bias and help performance, fine-tuning the choice of β scaling parameter could improve convergence for some properties, but maybe not similarly so for all the desired scores. The correlations mismatch compared with the KF in Figure 3.7 are slightly different depending on the fixed reference point, but they converge with increasing sample, especially so for the ETKF which has curves going faster to 0. For both SparseObsETKF and IEWPF there seem to be a remaining mismatch in this CE score even for thousands of ensemble members.

Effects of sparsity of observational data In a regime dominated by the sparsity of observations, we also want to stress-test all methods with respect to the amount of observational data. For this purpose, we repeat the case study using $N_Y \in \{8, 15, 60, 104, 170\}$ regularly placed observation sites. These numbers are chosen such that the observation locations have distance of 15, 10, 5, 4, and 3 grid cells apart from each others, respectively. We use $N_e = 50$ ensemble members. Of course, the localisation scheme for the SparseObsETKF is not designed for dense data and will get computationally very inefficient due to a high number of batches that are processed serially. The localisation radius is not modified.

Figure 3.11 shows the same averaged metrics as before, with respect to a growing number of observations. Note that it no longer makes sense to distinguish between locations near and far from observations, since the observation sites get denser over the domain. The increase in observation data leads to a sharpening in the reference distribution calculated from the KF. For the ETKF, we observe that RMSE does not improve and its ECDF approximation gets worse, compared with the KF. This is because of the underestimation in variance and a slight bias which strongly penalises the d_{IQ}. Both SparseObsETKF and IEWPF improve their quality for increasing observation data size. This is surprising and noteworthy for IEWPF, as PFs tends to collapse for high dimensional observations. In contrast to RMSE and d_{IQ}, the CE does not depend on the observation sparsity and is practically constant on the level that we saw in Figure 3.10c.

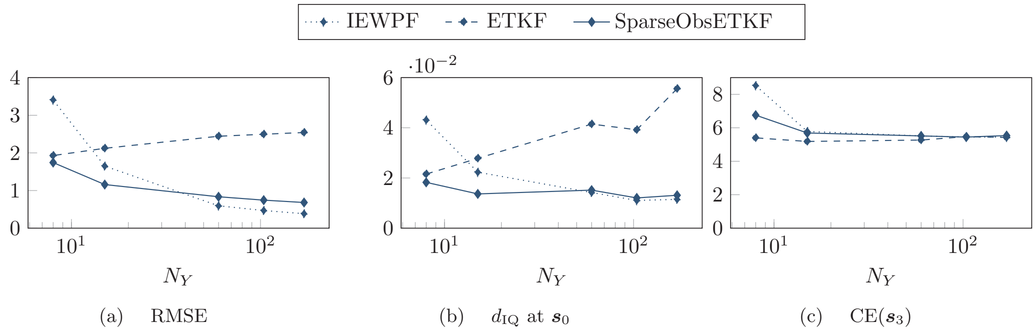

(a) RMSE (b) d_{IQ} at $\boldsymbol{s}_0$ (c) CE($\boldsymbol{s}_3$)

Figure 3.11: Evolution of the comparison measures as we change the sparsity/density of observation data through the number observations N_Y. The ensemble size is fixed at $N_e = 50$.

Summary In this case study, we verify the ensemble-based methods from Section 2 for a linear Gaussian data assimilation problem with the analytical KF reference. The SparseObsETKF and IEWPF include localisation, either explicitly or implicitly, which is connected to the correlation radius of the model error. Beyond the verification, we can in particular record that SparseObsETKF outperforms ETKF and IEWPF for smaller ensemble sizes (about $N_e \leq 250$). While the ETKF reduces the spectral radius in every data assimilation step more than the other methods, it requires a large ensemble size to obtain a reasonable approximation of the full covariance matrix. The localised version that ignores large-distance correlations is performing well for small ensemble sizes, but it does not improve much more for larger sizes. Similar tendencies are seen with the IEWPF. The approximation of the correlations between different time steps depend mostly on the ensemble size - the model error plays a major role in the evaluation and this criterion requires a higher ensemble size for a sufficient representation. For reasonable ensemble sizes, say 100, both IEWPF and SparseObsETKF operate well for any density of observation data. For most criteria we tested in this example with sparse point data, the SparseObsETKF tends to give slightly better performance than the IEWPF. Based on this extensive statistical evaluation, we hence recommend considering the SparseObsETKF for similar kinds of applications with sparse data and limited ensemble sizes.

4 Comparison for Drift Trajectory Forecasting in a Simplified Ocean Model

We now increase both dimensionality and complexity as we turn to a non-linear simplified ocean model. This gives insight into the behaviour of the ensemble-based data assimilation methods on a challenging case with applied relevance. The practical purpose of this configuration is to use ensembles of computationally efficient simplified ocean models instead of or complementary to single realisations of complex operational ocean models in time critical situations. The simplified models allow for larger ensembles and hence facilitate uncertainty quantification. Such an approach can be useful in search-and-rescue operations, where drifters released by the vessel or relevant anchored buoys (also called moorings) can give sparse in-situ observations during the operation. These point observations can then be assimilated into the ensemble-based representation to improve the drift trajectory forecasts that specify a search area.

Due to the non-linearity of such an model, there is no analytical reference solution for the ensemble distributions available. We can nevertheless compare SparseObsETKF and IEWPF by studying their predictive properties with the ground truth in a simulation study. We base our numerical experiments on those presented in Holm et al. (2020), where the IEWPF was successfully tailored for efficient GPU-accelerated assimilation of point observations of a chaotic shallow-water model. We expand on the numerical result from that work by evaluating more skill scores, and by providing an in-depth comparison between IEWPF and SparseObsETKF for state estimation and drift trajectory forecasts. In particular, this will also serve as more thorough evaluation of the applicability of IEWPF in this context.

4.1 Simplified ocean model

The simplified ocean model is represented by the rotational shallow-water equations given by

$$\begin{aligned} \eta_t + (hu)_x + (hv)_y &= 0 \\ (hu)_t + \left(hu^2 + \frac{1}{2}gh^2\right)_x + (huv)_y &= fhv \\ (hu)_t + (huv)_x + \left(hv^2 + \frac{1}{2}gh^2\right)_y &= -fhv. \end{aligned} \tag{4.1}$$

This is a non-linear two-dimensional hyperbolic conservation law, which models conservation of mass through the deviation η from equilibrium sea level, and conservation of momentum through hu and hv, which are vertically integrated ocean currents in x- and y-direction, respectively. By denoting the equilibrium depth of the ocean by H, we get the total depth as $h = H + \eta$. Furthermore, g is the gravitational constant and f is the Coriolis parameter that accounts for the rotating frame of reference.

We solve eq. (4.1) using the high-resolution central-upwind finite-volume scheme proposed by Chertock et al. (2018). In our notation from the model equation eq. (2.1), the state vector $\boldsymbol{x}^n$ consists of the cell averaged values $(\eta_i^n, (hu)_i^n, (hv)_i^n)$ at time t^n for all cells i in the discretised domain. The $\mathcal{M}^n$ operator then applies the finite-volume scheme to evolve the state from $\boldsymbol{x}^{n-1}$ to $\boldsymbol{x}^n$. Note that the time step used by the numerical method can be chosen independently from the model time step, meaning that $\mathcal{M}$ might consist of multiple iterations of the numerical scheme.

We apply a small-scale Gaussian model error $\boldsymbol{\nu} \sim \mathcal{N}(0, \boldsymbol{Q})$. It is constructed from a coarse-scale perturbation of η, which is smoothed by a second-order autoregressive function and projected onto the numerical grid. The model error for hu and hv is then inferred according to geostrophic balance to ensure physical feasibility. Further details about this model are available in Brodtkorb and Holm (2021) and Holm et al. (2020).

4.2 Experiment design

In the following, we use the same experimental design as in Holm et al. (2020). We consider a rectangular domain covering 1100 km × 666 km that is discretised as a uniform Cartesian 500 × 300 grid. The domain has periodic boundary conditions and constant equilibrium depth $H = 230.0\,\text{m}$. The initial conditions, for the ground truth as well as for all ensemble members, consist of a westward jet in the north part of the domain and an eastward jet in the south, with $hv = 0$. Both jets are balanced according to geostrophy by η so that the initial conditions are in steady state. This steady state is however unstable, and slight perturbations, such as those from the model error $\boldsymbol{\nu}$, cause chaotic behaviour.

As an example of the turbulent behaviour, Figure 4.1 shows the water velocities for one realisation that is labeled as the synthetic truth $\boldsymbol{x}_{\text{true}}$. Here, the model error is added every 60 s, and the model error correlation radius is approximately 40 km. From Figure 4.1, we see that the jets in $\boldsymbol{x}_{\text{true}}$ are still quite regular after 3 days, but grow more irregular after 6 and 10 days. It should be noted that the mean state from a pure Monte Carlo experiment without data assimilation will results in $hv \approx 0$ even after 10 days. This indicates that it is challenging to correctly capture where and how the turbulent behaviour will develop.

From $\boldsymbol{x}_{\text{true}}$, we extract direct observations of only (hu, hv) at 60 locations in the domain every 5 minutes between day 3 and day 10, with observational noise sampled from $N(0, \boldsymbol{I})$. The turquoise dots in Figure 4.1 show the observation sites. In total, the experiment is characterised by 450.000 state variables versus only 120 very sparse noisy observations. After day 10, three drifters are released in the domain, and advected according to the simulated currents at every time step of the numerical scheme using a simple Euler scheme. Part of the challenge for the data assimilation methods is to forecast the trajectories of these drifters.

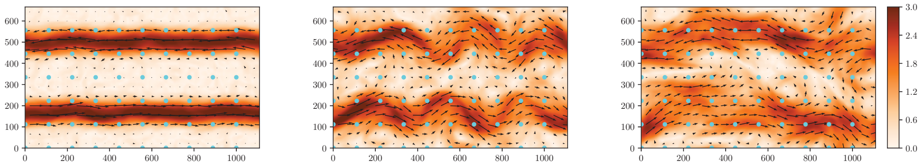

(a) Day 3 (b) Day 6 (c) Day 10

Figure 4.1: State of the synthetic truth after 3, 6, and 10 simulation days. The arrows indicate the direction as well as strength of the ocean currents derived from u and v, respectively. The background visualises the magnitude of velocity in $\frac{\mathrm{m}}{\mathrm{s}}$. The turquoise dots mark the fixed-point buoy positions.

The data assimilation start at simulation day 3 after each ensemble member has been spun up from the steady state through independently sampled model errors. Even though all ensemble members are visually very similar at this stage, they have started to develop internal instabilities that will grow over time unless the observations are successfully assimilated.

This case is much more challenging than the advection diffusion model in Section 3: The shallow-water model is non-linear, there are unobserved variables, and it has significantly higher dimensionality. Critically, the non-linear dynamics of the shallow-water model is challenging to capture. In the advection diffusion model, the state converges towards an equilibrium due to the diffusion, whereas our shallow-water equation case gets chaotic dynamics that makes the ensemble naturally diverge in time.

4.3 Numerical results

Classical EnKF approaches like the ETKF lead to useless results for this difficult case, and only results of the IEWPF and SparseObsETKF are shown in the comparison. We use $N_e = 100$ as a compromise between computational effort and statistical quality. Based on our experiments on this high-dimensional non-linear model, the IEWPF performance is not very sensitive to the explicit choice of β and we use the maximal allowed value. The localisation radius for the SparseObsETKF is chosen slightly larger than the model error correlation radius. In contrast to Section 3, we now also investigate the influence of relaxation in the SparseObsETKF. We present results for the SparseObsETKF without relaxation ($\phi = 1.0$) and for the SparseObsETKF whose weights in the localisation are scaled by $\phi = 0.5$. We compare data assimilation methods with the simulated truth using a number of skill scores that refer to this ground truth.

State estimation We first look at deviations of the ensemble mean from the truth by

$$\mathbf{err}_{\text{mean}}^{\text{day10, true}} = \overline{\boldsymbol{x}}^{\text{day10}} - \boldsymbol{x}_{\text{true}}^{\text{day10}}, \tag{4.2}$$

which represents the error in the correct physical unit. We also investigate the standard deviation in the ensemble

$$\text{STD}^{\text{day10}} = \frac{1}{N_e - 1}\sqrt{\sum_{e=1}^{N_e}\left(\boldsymbol{x}_e^{\text{day10}} - \overline{\boldsymbol{x}}^{\text{day10}}\right)^2}, \tag{4.3}$$

which gives insight about the ensemble spread around its mean.

Figure 4.2a shows the mismatch between the truth and the ensemble means of the conserved variables after assimilating the final observations on day 10. Significant differences become clear in the error of the sea-surface elevation η (left): While the IEWPF has some moderate, relatively smooth error over the entire domain, the mean of the SparseObsETKF is far off in half of the domain. In particular, the rims in the error field are very sharp, also recognisable in the error spots of the currents at the edges of the jets. This

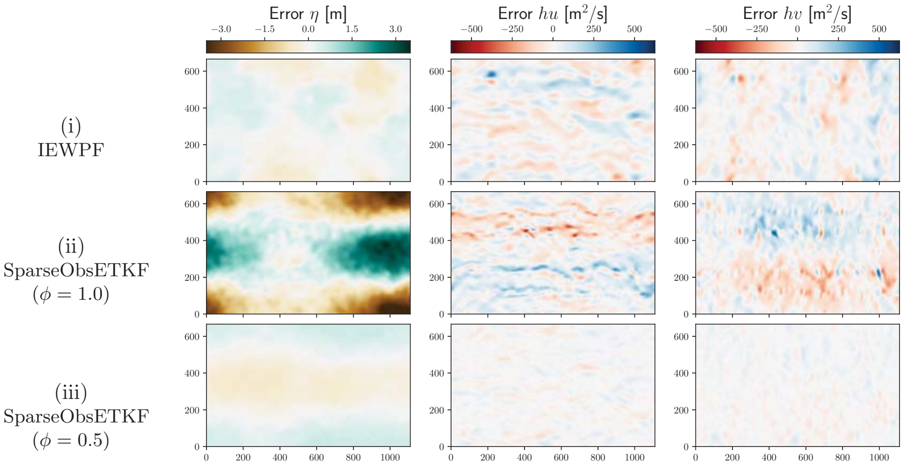

(a) Error $\mathbf{err}_{\text{mean}}^{\text{day10, true}}$

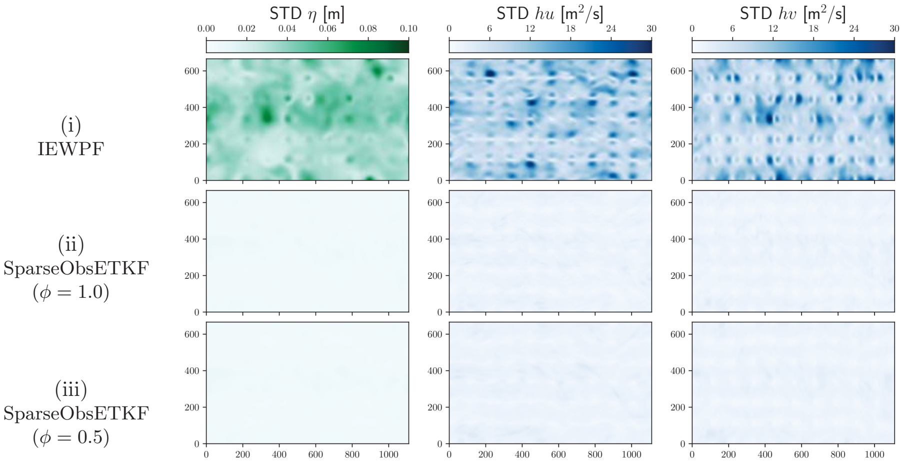

(b) Standard deviation $\text{STD}^{\text{day10}}$

Figure 4.2: Properties of the state estimation for the different physical variables in this simplified ocean model (sea-surface elevation η as well as momenta hu and hv) after day 10 measured in the error of the mean versus the truth and the standard deviation presented for the IEWPF as well as SparseObsETKF without and with inflation.

indicates that the ensemble produces very fast changing ocean fields with the tendency to non-physical members. However, relaxation with $\phi = 0.5$ (bottom) impressively fixes some of those issues and the error fields become much smoother and closely calibrated, even though there is still a recognisable, but weak inherited pattern in the error for elevation.

There are structured artefacts identifiable around the observation sites for IEWPF in Figure 4.2b. Even though Figure 4.2a shows that the ensemble mean gives a very precise description of the ground truth, the ensemble variance is large. As discussed in Holm et al. (2020), the IEWPF updates the momentum locally by inducing a corrective current formed by the structure in the model error covariance matrix $\boldsymbol{Q}$. In this case, $\boldsymbol{Q}$ induces geostrophically balanced dipole structures, which means that while improving the state at the observation site, we risk deteriorating the solution in its vicinity. This illustrates a weakness of IEWPF, showing that its quality is only as good as the structure of $\boldsymbol{Q}$.

In the standard deviations for the SparseObsETKF in Figure 4.2b (middle row), there is an expected pattern of low values around observation sites. Since the localisation only corrects around the buoys and leaves the forecast otherwise unchanged, the variance in one data assimilation step is mainly reduced in local areas. With the dynamical model over time, the variance reduction is disseminated over the entire domain. Furthermore, the standard deviation in the SparseObsETKF is on a very low level. Having areas of low error together with the sudden changes towards big errors suspects overfitting. Also the relaxed SparseObsETKF (lower row) achieves a similarly low standard deviation after day 10.

Drift trajectory forecasting To further compare the practical applicability of IEWPF and SparseObsETKF, we look at forecasts of drift trajectories starting at day 10.

Figure 4.3 demonstrates the forecasted trajectories of drifters that are realised after ten simulation days in the simplified ocean model. The three drop locations are selected to capture different characteristics in the currents: Drifter 1 (display (a)) starts in the middle of a rather weak and big east stream. Drifter 2 (display (b)) starts in a rather strong west stream and drifter 3 (display (c)) starts in a turbulent area in between the dominating streams. For the first two days of forecast, we show the true trajectory along with the trajectories for all ensemble members and the ensemble mean, whereas for the third day (right) we show the estimated kernel density (Scott, 1992) of the final drifter locations along with the true trajectory.

For drifter 1, all trajectories have an east-wards drift, but the IEWPF members fan out from the beginning while the SparseObsETKF trajectories stay close together. Without relaxation, the truth becomes an outlier in the SparseObsETKF forecast. With relaxation, the truth stays within the forecast. The trajectories from the IEWPF catch the truth in a high-probability area, but their spread covers almost the entire extent of the domain in the y-direction.

Even though drifter 2 starts within a jet, it drifts only shortly west-wards before it takes a sudden turn towards the north. Here, we can again see the turbulent behaviour of this non-linear model. The trajectories of the IEWPF again spread out widely, and therefore does not reveal any consistent dynamical pattern in the underlying currents. SparseObsETKF not only misses the true trajectory completely, it also shows some wriggling trajectories which indicates that there are unbalanced gravitational waves in the ensemble. Relaxation increases the spread in the trajectories up to day 2, and most of the ensemble members capture the sudden turn in the truth, even though this happens a day after assimilating the final observations.

Drifter 3, which is released in an unstable area, follows what is almost a rotation-like pattern. Here, the IEWPF is unable to estimate a clear direction even for the first 24 hours, and after day 10 the drifter distribution stretches out across almost half the simulation domain. In contrast, SparseObsETKF with and without relaxation the ensemble gives a precise forecast for the first day, only showing a spread for the two last days. The truth is well represented by the ensemble for both experiments, but we see that the spread is remarkably reduced when using relaxation.

In general, we see that even though IEWPF is able to give a good state estimation through the mean, the spread in the underlying ocean state is too large to facilitate precise drift trajectory forecasts. Furthermore, LETKF without relaxation shows clear signs of overfitting, as the forecasts have low spread and do not match the ground truth. Introducing relaxation into the SparseObsETKF reduces this overfitting such that the true trajectories are correctly forecasted and uncertainty is better represented. Even more important, giving

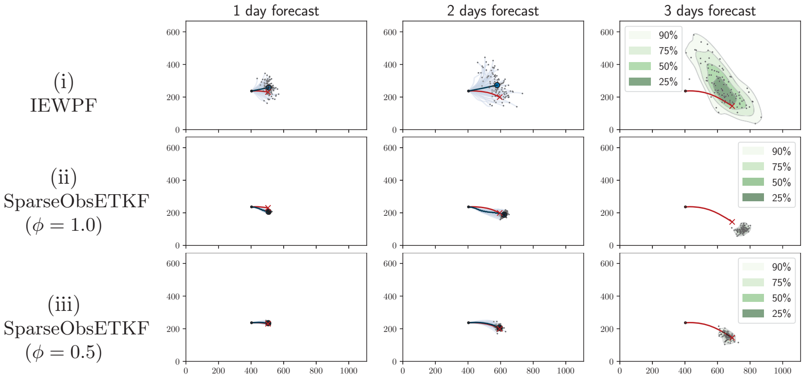

(a) Drifter 1

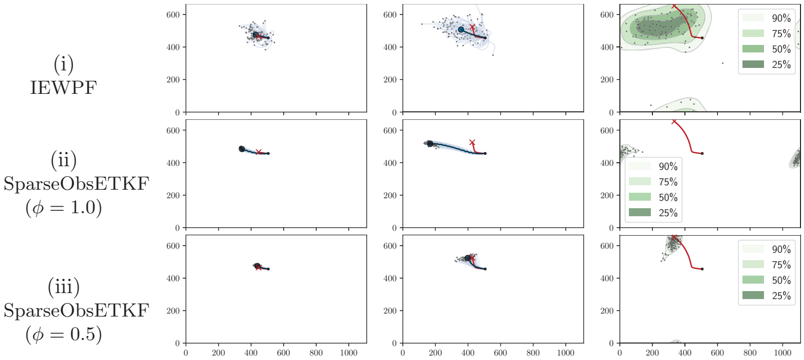

(b) Drifter 2

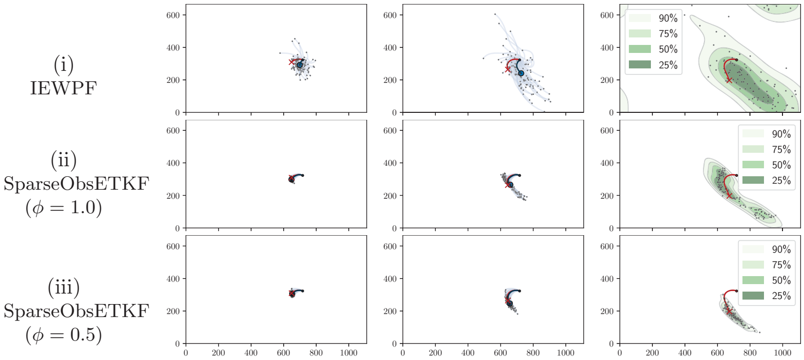

(c) Drifter 3

Figure 4.3: Drift trajectory forecasts for three different starting positions. True trajectories represented in red, and for the first two days trajectories of ensemble members are light blue and the ensemble mean in dark blue. For the third day, the forecasted drifter positions of all ensemble members are shown with black dots and selected levels of the estimated kernel density are visualised.

more weight to the forecast that comes from the physical model prevents the ensemble from unintended anomalies. The drift trajectories estimation draws attention away from the ocean states towards dynamic visual characteristics in the ensemble.

4.4 Discussion of skill scores

Complementary to drift trajectory forecasts, we look into characteristics of both methods during the data assimilation phase between day 3 and day 10. We compare statistical properties of the ensemble against the observation data. In this setting, the key idea of skill scores is to evaluate how reliably the ensemble can forecast the next observation. An illustrative introduction with a lot of examples from atmospheric weather forecasting can be found in Wilks (2005, Chapter 7). Mathematically speaking, in this setting with data comparison, a score is

$$s\left(\widehat{F}^{n,f}, \boldsymbol{y}^n\right) \in \mathbb{R}, \tag{4.4}$$

which in our case quantifies some property of the empirical distribution from an ensemble forecast $\left(\boldsymbol{H}\boldsymbol{x}_e^{n,f}\right)_{e=1}^{N_e}$ against the true observation $\boldsymbol{y}^n$, meaning hu_j and hv_j for all $j = 1, \dots, N_Y$. We consider three different skill scores to judge the performance.

Bias After asserting the calibration of the full analysis mean in Figure 4.2a, we investigate this further by evaluating the bias of the forecast as

$$s_1^n = \frac{1}{N_Y}\sum_{j=1}^{N_Y}\left[\overline{hu}_j^{n,f} - \boldsymbol{y}_{j,1}^n + \overline{hv}_j^{n,f} - \boldsymbol{y}_{j,2}^n\right]. \tag{4.5}$$

Here, $\overline{hu}$ and $\overline{hv}$ are the ensemble means. The bias discovers systematic trends off in the estimator.

Mean square error We further investigate the distance of each ensemble member individually from the data by measuring the MSE as

$$s_2^n = \frac{1}{N_e}\sum_{e=1}^{N_e}\left[\frac{1}{N_Y}\sum_{j=1}^{N_Y}|hu_{e,j}^{n,f} - \boldsymbol{y}_{j,1}^n|^2 + |hv_{e,j}^{n,f} - \boldsymbol{y}_{j,2}^n|^2\right]. \tag{4.6}$$

The MSE equals zero only when all ensemble members predict the observation exactly. However, this is of course not desired from a probabilistic forecast representing associated uncertainty. Nevertheless, a small MSE is desired and yields accurate fit to the data respecting the standard deviation in the observation error.

Continuous ranked probability score Similar to the integrated quadratic differences which compared distribution forecasts, we use a scoring rule that analyses the distribution of the ensemble members with the observation, see Gneiting and Raftery (2007). The CRPS is here defined by

$$s_3^n = \frac{1}{N_Y}\sum_{j=1}^{N_Y}\left[\frac{1}{N_e}\sum_{e=1}^{N_e}|hu_{e,j}^{n,f} - \boldsymbol{y}_{j,1}^n| + |hv_{e,j}^{n,f} - \boldsymbol{y}_{j,2}^n| - \frac{1}{2{N_e}^2}\sum_{e=1}^{N_e}\sum_{k=1}^{N_e}|hu_{e,j}^{n,f} - hu_{k,j}^{n,f}| + |hv_{e,j}^{n,f} - hv_{k,j}^{n,f}|\right]. \tag{4.7}$$

Large CRPS values can originate from bias (first terms) or the spread in the ensemble (last terms). Together with the scores for the bias and MSE, this allows one to identify the source of ensemble errors and to infer the properties of the ensemble.

Figure 4.4 presents the evolution of these skill scores for each data assimilation time step. These results are obtained from the same run as in Section 4.3. Note that when we assimilate the first observation after spin-up on day 3, the spread in the ensemble is relatively large by construction for all methods. It should be noted that hu and hv take values up to $500\,\mathrm{m}^2/\mathrm{s}$, which means that all methods have a relatively small

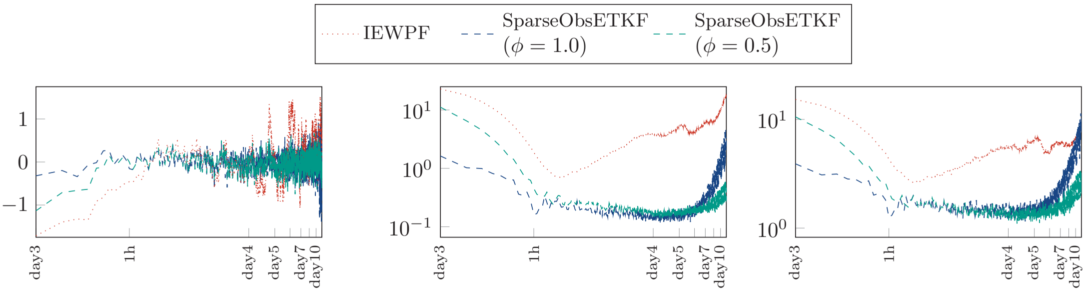

(a) Bias (b) MSE (c) CRPS

Figure 4.4: Evolution of skill scores for the IEWPF (red), SparseObsETKF without relaxation (blue), and SparseObsETKF with relaxation (turquoise) for the data assimilation phase in the experiment.

bias. In the starting phase, the SparseObsETKF immediately calibrates to the observations, whereas the IEWPF and relaxed SparseObsETKF require several data assimilation steps to correct the bias. We see however, that the bias for all methods grow over time, but with the relaxed SparseObsETKF keeping the smallest values. The systematic bias from the relaxation becomes negligible as it is sufficiently often reduced by repeated weighting with the unbiased analysis.

Looking at the MSE and CRPS, we see that both SparseObsETKF versions improve during the first few assimilation steps and stabilise at a certain level. As expected, the initial improvement with relaxation is slower than without relaxation, but this gap is closed already after 1 simulation hour, which corresponds to 12 data assimilation cycles. The quality of both SparseObsETKF versions are then stable until approximately simulation day 5, when the model dynamics gets more turbulent. At this point, the solution without relaxation starts to deteriorate due to the overfitting. Note that we see a similar trend for the relaxed SparseObsETKF later in the experiment. By relaxing even more ($\phi = 0.25$, not shown), we confirm the trend with even slower convergence in the beginning and later divergence at the end.

Similarly to the relaxed SparseObsETKF, IEWPF also converges during the initial data assimilation cycles, but the skill scores do not stabilise and instead diverge slowly. The slow initial convergence was also pointed out in Section 3, where we had to run the data assimilation sufficiently long to reach a stable level before being able to provide a fair comparison.

Note that the ensemble variance can be derived from MSE and bias. Then we see that the forecast variance behaves qualitatively similar as the MSE (not shown here). For a full assessment of the skills of a data assimilation method a single skill score gives only limited information. But for instance, the combinations of bias and CRPS broadens the insights, since the bias helps to explain the contributions in the CRPS. However, the differences especially between SparseObsETKF without relaxation and IEWPF in the skill score results do not seem substantial, whereas we have seen contrary properties in the drift trajectories that stay concealed in the monitoring of the skill scores. In general, this discussion tells us that the SparseObsETKF assimilates the ensemble much stronger towards data than the IEWPF and exemplifies the effects of relaxation.

Rank histograms We next look at rank histograms to analyse the adequacy of the ensemble spread. A short time-span in the simulation is repeated multiple times and the rank of the simulation truth in the ensemble ordering is monitored at six dynamically independent locations. Rank histograms then present the frequency of which a certain rank is reported among the N_e realisations of the ensemble and the shape of the histograms is used as a diagnostic tool to identify shortcomings of methods (Saetra et al., 2004). Flat rank histograms are commonly understood as indication for ensemble consistency or reliability of the ensemble, as it means that every ensemble member is sampled from the same distribution as the truth.

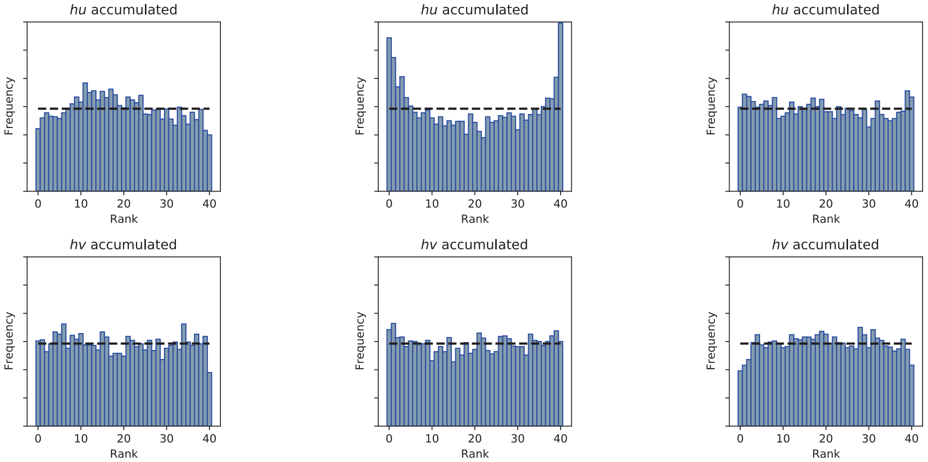

(a) IEWPF (b) SparseObsETKF ($\phi = 1.0$) (c) SparseObsETKF ($\phi = 0.5$)

Figure 4.5: Rank histograms recording the rank of the true observation within the ensemble for the observed variables. The dashed line indicates the hypothetical uniform distribution.

In Figure 4.5, we show rank histograms from repeating our experiment 1000 times, using $N_e = 40$ and simulating the first hour of data assimilation after the spin-up only. The most striking result is the clear U-shape in hu for SparseObsETKF without relaxation, which indicates that the truth often is an outlier in the ensemble and that the ensemble is underdispersive. Furthermore, we observe that IEWPF produces a slight hill-shaped rank histogram for hu, corresponding to an overdispersive ensemble. Both these observations match well with what we saw in Section 4.3. In comparison, the hu rank histogram for the relaxed SparseObsETKF closely resembles a uniform distribution. Note also that the rank histograms for hv are flatter for all three methods, but with a slight tendency towards overdispersion for the relaxed SparseObsETKF. This might be from the nature of the problem, as almost all dynamics in the case is along the x-axis.

While the rank histograms give insights how able the ensemble is to respect the uncertainty and we are able to draw similar assertions from them as we suspected already before, Hamill (2001) and Wilks (2011) advice to be careful with their interpretation, since, e.g. spatial effects between the different locations become hidden.

Summary Based on these results for the nonlinear model, we see that the CRPS together with the bias are a good start for an analysis of the ensembles during the data assimilation phase. These scalar scores are simple to include into any data assimilation sequence. By also analysing statistics over all state variables, we are able to identify additional spatial artefacts and a fundamentally different variance in the ensemble. Even though the rank histogram for the IEWPF looks reasonably flat and we get a well-calibrated mean for the state estimation, we see through the standard deviation that there are artefacts in the ensemble, leading to a higher spread than what we see for SparseObsETKF. This also made us realise how sensitive IEWPF is to the covariance structure in the model error.

Stress-testing the SparseObsETKF in this high-dimensional non-linear experiments with very sparse data discloses that the SparseObsETKF has a tendency of overfitting to the observations, resulting in an underestimated variance in the ensemble. SparseObsETKF is also not able to correctly estimate the unobserved variable η. In practice, we see that relaxing the ensemble to prior perturbations is a good remedy for these flaws. It significantly weakens the defects, but still inherits the structures from the full SparseObsETKF. We experienced that it is not necessary to fine-tune the relaxation parameter as results were similar for $\phi = 0.25$ and $\phi = 0.75$. We further point out that we tested classical covariance inflation, but this led to nonphysical states for η, while the variance of hu and hv was barely effected. Hence, it is fair to use the SparseObsETKF and the in-built relaxation with caution.

5 Conclusion

We have compared two conceptually different state-of-the-art ensemble-based data assimilation methods, namely IEWPF and ETKF with localisation, with emphasis on the handling of sparse observation data and studied how their performances compare to each other. We have shown how localised updates are implemented by design in the IEWPF, provided that the model error covariance matrix has a local pattern, and that observations are only spread in a certain radius around the observation locations and that this is especially enhanced for sparse observations. For the ETKF, we employ a explicit localisation scheme that gives good control of computations in reduced dimensions and of the correlations between observations. We have considered two distinct cases, both motivated by simplified models applicable to oceanography. The first case studied state estimation of a linear Gaussian advection diffusion model, for which we also computed the analytical filtering distribution. This facilitated for an in-depth statistical verification of the two methods in terms of estimation of the mean, covariances, distribution coverage, spectral radius and spatial-temporal connectivity. In the assessment, which also included the standard ETKF, we recorded the performance of the ensemble-based methods in relation to the number of ensemble members and observation size. The second case was a non-linear shallow water model used for forecasting of drift trajectories. Here, we compared the performance of SparseObsETKF and IEWPF in terms of skill scores and forecast abilities. We also discussed relaxation for the SparseObsETKF localisation scheme for this case. The extensive collections of comparison metrics allowed us to analyse several properties in the ensemble representations.

Our results for the first case verified that both the IEWPF and the SparseObsETKF give very good estimates of the analytical reference solution. Additionally, we exhibit effects of different localisation parametrisations for the SparseObsETKF and IEWPF. For moderate ensemble sizes, both methods delivered on par with the KF and clearly outperformed the ETKF in terms of RMSE and coverage probabilities. ETKF was best at estimating the covariance matrices, but it suffers from spurious correlations in the updates. The SparseObsETKF yields small divergences independent of the ensemble size. In the estimation of spatio-temporal model correlations, our results revealed that all three methods performed quite evenly. ETKF converges fastest with respect to the ensemble size. Interestingly, we found that SparseObsETKF and IEWPF only showed minor improvements when increasing the ensemble size, meaning that it is most beneficial to choose one of these methods when computational resources are limited. IEWPF was the scheme benefiting the most from increased number of observations.

In the non-linear case, we learned that both IEWPF and SparseObsETKF gave estimations of the observed momentum variables with bounded errors, but SparseObsETKF without relaxation did so at the expense of nonphysical fields and small spread, causing the drift trajectory forecast in some cases to diverge from the truth. These issues were also seen in the skill scores. IEWPF, on the other hand, showed artefacts around observation sites, indicating that the model error correlation matrix might not always represent the optimal mapping for assimilating the observations. This also caused a large spread in the forecasted drift trajectories. In the case of SparseObsETKF, we showed that applying relaxation clearly improved calibration, resulting in very good general performance. These results were backed up with high-quality results in the skill scores throughout the data assimilation period and precise predictions of the drift trajectories.

To summarise, the most important findings in this paper where we consider spatially very sparse observations can be listed as follows:

- Evaluating a broad range of statistical metrics and skill scores proves to be a huge advantage as it gives a deep insight into the data assimilation methods that are not obtainable through only looking at single metrics. We recommend to start with testing bias and CRPS as one-dimensional quantities, but urge to continue with qualitative analysis for the entire spatial field.

- We strengthen the argument that IEWPF, in contrast to most other PFs, is applicable to high-dimensional applications, but that its results are highly dependent on the structure of model error covariance matrix.
- We have seen that the SparseObsETKF works well even for relatively small ensemble sizes, but good calibration of the relaxation is required to retain good results also for complex models. Upon proper relaxation, the results from the SparseObsETKF outperformed the ones of the IEWPF.

These results moreover open up new directions for future research. For instance, it would be interesting to investigate in more detail how sensitive IEWPF is to the structure of the model error covariance matrix. In our work, we tested our implementation of the covariance localisation only with respect to the ETKF. It would be interesting to check whether other variants of the EnKF work equally well, or if they have advantages or disadvantages over ETKF. Beyond this, the sensitivity of the localisation concept to the relaxation parametrisation could be tuned adaptively. Finally, it would also be interesting to test the IEWPF and the SparseObsETKF in a real-world settingby assimilating real observations into an ensemble of simplified ocean models with the aim to predict true drift trajectories.

Code Availability

The source code and data used to produce the results presented in this paper are openly available under a GPL3 licence at `http://doi.org/10.5281/zenodo.10039791` for Section 3 and at `http://doi.org/10.5281/zenodo.10037281`,`http://doi.org/10.5281/zenodo.10039872` for Section 4.

Acknowledgement

The authors would like to thank Kjetil Olsen Lye for valuable feedback on the manuscript. Furthermore, we thank the two anonymous reviewers for their comments that improved the manuscript further.

References

Anderson, J. L. (2009). Spatially and temporally varying adaptive covariance inflation for ensemble filters. *Tellus, Series A: Dynamic Meteorology and Oceanography*, 61 A(1):72–83.

Anderson, J. L. and Anderson, S. L. (1999). A Monte Carlo implementation of the nonlinear filtering problem to produce ensemble assimilations and forecasts. *Monthly Weather Review*, 127(12):2741–2758.

Asch, M., Bocquet, M., and Nodet, M. (2016). *Data assimilation: methods, algorithms, and applications*. SIAM.

Bishop, C. H., Etherton, B. J., and Majumdar, S. J. (2001). Adaptive sampling with the ensemble transform kalman filter. part i: Theoretical aspects. *Monthly Weather Review*, 129(3):420–436.

Breivik, Ø., Allen, A. A., Maisondieu, C., and Olagnon, M. (2013). Advances in search and rescue at sea. *Ocean Dynamics*, 63(1):83–88.

Brodtkorb, A. R. and Holm, H. H. (2021). Coastal ocean forecasting on the GPU using a two-dimensional finite-volume scheme. *Tellus, Series A: Dynamic Meteorology and Oceanography*, 73(1):1–22.

Burgers, G., Van Leeuwen, P. J., and Evensen, G. (1998). Analysis scheme in the ensemble Kalman filter. *Monthly Weather Review*, 126(6):1719–1724.

Carrassi, A., Bocquet, M., Bertino, L., and Evensen, G. (2018). Data assimilation in the geosciences: An overview of methods, issues, and perspectives. *Wiley Interdisciplinary Reviews: Climate Change*, 9(5):1–50.

Chertock, A., Dudzinski, M., Kurganov, A., and Lukáčová-Medvid'ová, M. (2018). Well-balanced schemes for the shallow water equations with Coriolis forces. *Numerische Mathematik*, 138(4):939–973.

Chopin, N. and Papaspiliopoulos, O. (2020). *An Introduction to Sequential Monte Carlo Methods*. Springer.

Desroziers, G., Berre, L., Chapnik, B., and Poli, P. (2006). Diagnosis of observation, background and analysis-error statistics in observation space. *Quarterly Journal of the Royal Meteorological Society*, 131(613):3385–3396.

Doucet, A., Godsill, S., and Andrieu, C. (2000). Methods for Bayesian filtering. *Statistics and Computing*, pages 197–208.

Evensen, G. (1994). Sequential data assimilation with a nonlinear quasi-geostrophic model using Monte Carlo methods to forecast error statistics. *Journal of Geophysical Research*, 99(C5):10143–10162.

Evensen, G. (2003). The Ensemble Kalman Filter: Theoretical formulation and practical implementation. *Ocean Dynamics*, 53(4):343–367.

Evensen, G. (2009). *Data Assimilation. The Ensemble Kalman Filter*. Springer.

Foss, K. H., Berget, G. E., and Eidsvik, J. (2021). Using an autonomous underwater vehicle with onboard stochastic advection-diffusion models to map excursion sets of environmental variables. *Environmetrics*, 33(November 2020):1–18.

Gaspari, G. and Cohn, S. E. (1999). Construction of correlation functions in two and three dimensions. *Quarterly Journal of the Royal Meteorological Society*, 125(554):723–757.

Gneiting, T. and Raftery, A. E. (2007). Strictly proper scoring rules, prediction, and estimation. *Journal of the American Statistical Association*, 102(477):359–378.

Greybush, S. J., Kalnay, E., Miyoshi, T., Ide, K., and Hunt, B. R. (2011). Balance and ensemble Kalman filter localization techniques. *Monthly Weather Review*, 139(2):511–522.

Hamill, T. M. (2001). Interpretation of rank histograms for verifying ensemble forecasts. *Monthly Weather Review*, 129(3):550–560.

Holm, H. H. (2020). *Efficient Forecasting of Drift Trajectories using Simplified Ocean Models and Nonlinear Data Assimilation on GPUs*. PhD thesis, Norwegian University of Science and Technology.

Holm, H. H., Sætra, M. L., and van Leeuwen, P. J. (2020). Massively parallel implicit equal-weights particle filter for ocean drift trajectory forecasting. *Journal of Computational Physics: X*, 6(0314):100053.

Houtekamer, P. L. and Mitchell, H. L. (1998). Data assimilation using an ensemble kalman filter technique. *Monthly Weather Review*, 126(3):796–811.

Houtekamer, P. L. and Mitchell, H. L. (2001). A sequential ensemble Kalman filter for atmospheric data assimilation. *Monthly Weather Review*, 129(1):123–137.

Houtekamer, P. L. and Zhang, F. (2016). Review of the ensemble Kalman filter for atmospheric data assimilation. *Monthly Weather Review*, 144(12):4489–4532.

Hunt, B. R., Kostelich, E. J., and Szunyogh, I. (2007). Efficient data assimilation for spatiotemporal chaos: A local ensemble transform Kalman filter. *Physica D: Nonlinear Phenomena*, 230(1-2):112–126.

Kirchgessner, P., Nerger, L., and Bunse-Gerstner, A. (2014). On the choice of an optimal localization radius in ensemble Kalman filter methods. *Monthly Weather Review*, 142(6):2165–2175.

Li, H. (2007). *Local Ensemble Transform Kalman Filter*. PhD thesis, University of Maryland.

Li, H., Kalnay, E., and Miyoshi, T. (2009). Simultaneous estimation of covariance inflation and observation errors within an ensemble Kalman filter. *Quarterly Journal of the Royal Meteorological Society*, 135(639):523–533.

Morzfeld, M., Hodyss, D., and Snyder, C. (2017). What the collapse of the ensemble Kalman filter tells us about particle filters. *Tellus, Series A: Dynamic Meteorology and Oceanography*, 69(1):1–15.

Nerger, L. (2015). On serial observation processing in localized ensemble Kalman filters. *Monthly Weather Review*, 143(5):1554–1567.

Nussbaumer, R., Mariethoz, G., Gloaguen, E., and Holliger, K. (2018). Which Path to Choose in Sequential Gaussian Simulation. *Mathematical Geosciences*, 50(1):97–120.

Ott, E., Hunt, B. R., Szunyogh, I., Zimin, A. V., Kostelich, E. J., Corazza, M., Kalnay, E., Patil, D., and Yorke, J. A. (2004). A local ensemble Kalman filter for atmospheric data assimilation. *Tellus A: Dynamic Meteorology and Oceanography*, 56(5):415–428.

Raanes, P. N., Bocquet, M., and Carrassi, A. (2019). Adaptive covariance inflation in the ensemble Kalman filter by Gaussian scale mixtures. *Quarterly Journal of the Royal Meteorological Society*, 145(718):53–75.

Röhrs, J., Dagestad, K. F., Asbjørnsen, H., Nordam, T., Skancke, J., Jones, C. E., and Brekke, C. (2018). The effect of vertical mixing on the horizontal drift of oil spills. *Ocean Science*, 14(6):1581–1601.

Saetra, O., Hersbach, H., Bidlot, J. R., and Richardson, D. S. (2004). Effects of observation errors on the statistics for ensemble spread and reliability. *Monthly Weather Review*, 132(6):1487–1501.

Sætrom, J. and Omre, H. (2013). Uncertainty quantification in the Ensemble Kalman filter. *Scandinavian Journal of Statistics*, 40(4):868–885.

Sakov, P. and Bertino, L. (2011). Relation between two common localisation methods for the EnKF. *Computational Geosciences*, 15(2):225–237.

Scott, D. W. (1992). *Multivariate density estimation: Theory, practice, and visualization: Second edition*. Wiley.

Sigrist, F., Künsch, H. R., and Stahel, W. A. (2015). Stochastic partial differential equation based modelling of large space-time data sets. *Journal of the Royal Statistical Society. Series B: Statistical Methodology*, 77(1):3–33.

Skauvold, J., Eidsvik, J., van Leeuwen, P. J., and Amezcua, J. (2019). A revised implicit equal-weights particle filter. *Quarterly Journal of the Royal Meteorological Society*, 145(721):1490–1502.

Snyder, C., Bengtsson, T., Bickel, P., and Anderson, J. (2008). Obstacles to high-dimensional particle filtering. *Monthly Weather Review*, 136(12):4629–4640.

Soares, R. V., Luo, X., Evensen, G., and Bhakta, T. (2021). Handling big models and big data sets in history-matching problems through an adaptive local analysis scheme. *SPE Journal*, 26(2):973–992.

Szunyogh, I., Satterfield, E. A., Elana, J., Gyarmati, G., Kalnay, E., Hunt, B. R., Eric, J., Kuhl, D. D., Ott, E., and Yorke, J. A. (2007). The Local Ensemble Transform Kalman Filter and its implementation on the NCEP global model at the University of Maryland The LETKF and its implementation on the NCEP GFS model. *Proc. ECMWF Workshop on flow-dependent aspects of data assimilation*, pages 1–18.

Thorarinsdottir, T. L., Gneiting, T., and Gissibl, N. (2013). Using proper divergence functions to evaluate climate models. *SIAM-ASA Journal on Uncertainty Quantification*, 1(1):522–534.

Van Leeuwen, P. J. (2009). Particle filtering in geophysical systems. *Monthly Weather Review*, 137(12):4089–4114.

van Leeuwen, P. J. (2020). A Consistent Interpretation of the Stochastic Version of the Ensemble Kalman Filter. *Quarterly Journal of the Royal Meteorological Society*, 146(731):2815–2825.

van Leeuwen, P. J., Künsch, H. R., Nerger, L., Potthast, R., and Reich, S. (2019). Particle filters for high-dimensional geoscience applications: A review. *Quarterly Journal of the Royal Meteorological Society*, 145(723):2335–2365.

Vetra-Carvalho, S., van Leeuwen, P. J., Nerger, L., Barth, A., Altaf, M. U., Brasseur, P., Kirchgessner, P., and Beckers, J. M. (2018). State-of-the-art stochastic data assimilation methods for high-dimensional non-Gaussian problems. *Tellus, Series A: Dynamic Meteorology and Oceanography*, 70(1):1–38.

Whitaker, J. S. and Hamill, T. M. (2002). Ensemble data assimilation without perturbed observations. *Monthly Weather Review*, 130(7):1913–1924.

Wilks, D. S. (2005). *Statistical methods in the atmospheric sciences*. Elsevier Inc.

Wilks, D. S. (2011). On the reliability of the rank histogram. *Monthly Weather Review*, 139(1):311–316.

Zhang, F., Snyder, C., and Sun, J. (2004). Impacts of initial estimate and observation availability on convective-scale data assimilation with an ensemble kalman filter. *Monthly Weather Review*, 132(5):1238–1253.

Zhu, M., van Leeuwen, P. J., and Amezcua, J. (2016). Implicit equal-weights particle filter. *Quarterly Journal of the Royal Meteorological Society*, 142(698):1904–1919.

Paper IV

Multi-Level Data Assimilation for Simplified Ocean Models

Florian Beiser, Håvard Heitlo Holm, Kjetil Olsen Lye, Jo Eidsvik

In review

This paper is under review for publication and is therefore not included.

ISBN 978-82-326-8074-0 (printed ver.)
ISBN 978-82-326-8073-3 (electronic ver.)
ISSN 1503-8181 (printed ver.)
ISSN 2703-8084 (online ver.)

NTNU
Norwegian University of
Science and Technology